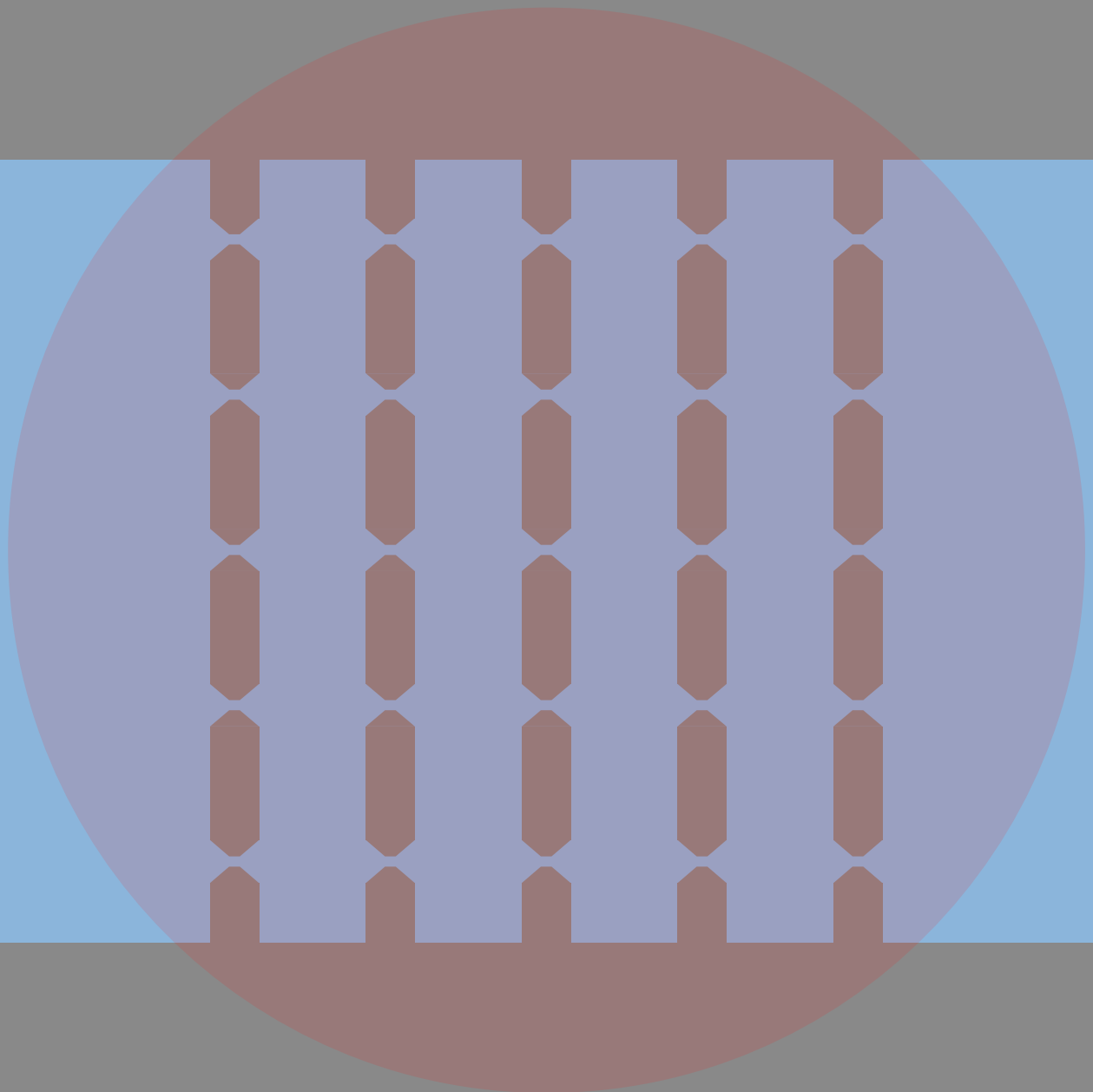


# Photoconductive antennas

Towards the design of an imaging setup using photoconductive antennas

Martijn Huiskes



# Photoconductive antennas

Towards the design of an imaging setup using  
photoconductive antennas

by

Martijn Huiskes

to obtain the degree of Master of Science  
at the Delft University of Technology,  
to be defended publicly on Thursday October 20, 2022 at 10:15 AM.

Student number: 4701291  
Project duration: November 9, 2021 – October 20, 2022  
Thesis committee: Prof. dr. N. Llombart-Juan, TU Delft, supervisor  
Prof. dr. A. Neto, TU Delft, supervisor  
dr. F. Fioranelli, TU Delft

An electronic version of this thesis is available at <http://repository.tudelft.nl/>.

# Acknowledgements

This thesis summarizes the work done over the past year carried out within the Terahertz Sensing Group at the Delft University of Technology.

First and foremost, I would like to thank my supervisors dr. Nuria Llombart and dr. Andrea Neto, your guidance throughout the project has been truly exceptional. Nuria, even though you were guiding many students and were extremely busy with the organization of the IRMMW 2022 conference, you always made time to check in with me and to guide me whenever I had questions. Your critical thinking and patience allowed me to learn a lot. Andrea, your enthusiasm for electromagnetics during my bachelor's is what led me to pursue the WiCoS master's program and follow the EM courses in the first place. I'm glad I did. The many discussions about the project over the past year have been incredibly helpful.

To Huasheng Zhang, thank you for the discussions and for helping me understand many of the concepts I applied in this thesis.

Also, a big thanks to the whole Terahertz Sensing group for creating a great atmosphere at the university.

To my family and friends, thank you for supporting me throughout the years. I could not have done it without you.

*Martijn Huiskes  
Delft, October 2022*

# Contents

<b>Acknowledgements</b>	<b>i</b>
<b>Nomenclature</b>	<b>iv</b>
<b>1 Introduction</b>	<b>1</b>
1.1 State-of-the-art photoconductive antennas . . . . .	2
1.2 THz time-domain spectroscopy systems . . . . .	2
1.3 THz imaging systems . . . . .	3
1.4 Scope of the thesis . . . . .	4
<b>I Characterization of PCCAs</b>	<b>5</b>
<b>2 Photoconductive Connected Arrays</b>	<b>6</b>
2.1 Connected array analysis . . . . .	8
2.1.1 Array impedance . . . . .	8
2.1.2 Far-fields inside the lens medium (primary fields) . . . . .	9
2.1.3 Phase center . . . . .	11
2.1.4 Front-to-back efficiency . . . . .	11
2.2 Energy spectrum and radiated power . . . . .	12
2.2.1 Optical efficiency . . . . .	14
2.2.2 Application of the TD Norton circuit to a PCCA . . . . .	15
2.3 Conclusions . . . . .	17
<b>3 Physical Optics simulations for dielectric lenses</b>	<b>18</b>
3.1 PO analysis for a hemispherical lens . . . . .	18
3.1.1 PO procedure . . . . .	19
3.1.2 Full PCCA lens geometry . . . . .	20
3.1.3 Validity of the PO method using primary far-fields . . . . .	20
3.2 PO method using embedded element patterns . . . . .	21
3.3 Verification of the revised PO method . . . . .	22
3.4 Application of the revised PO method to fabricated geometries . . . . .	24
3.4.1 Lens efficiency . . . . .	26
3.4.2 Spectra and radiated power . . . . .	26
3.5 Conclusions . . . . .	27
<b>4 Array model comparison to experimental results</b>	<b>28</b>
4.1 Modeling and simulation of the QO channel . . . . .	29
4.2 Predicted and measured detected power . . . . .	30
4.3 Measured spectra . . . . .	32
4.4 Conclusions . . . . .	33
<b>II Imaging setup design</b>	<b>34</b>
<b>5 PCCA lens optimization</b>	<b>35</b>
5.1 Hemispherical lens extensions . . . . .	35
5.2 PCCA coupled to a parabolic reflector . . . . .	36
5.2.1 Aperture efficiency on a parabolic reflector . . . . .	36
5.2.2 Optimizing the aperture efficiency on a parabolic reflector . . . . .	37
5.2.3 Reducing the f-number . . . . .	39
5.3 Conclusions . . . . .	40

<b>6</b>	<b>Design of an imaging setup for PCA benchmarking</b>	<b>41</b>
6.1	QO focusing component	41
6.1.1	Lens dimensions and losses	42
6.2	Focal fields	44
6.2.1	Depth of Field	46
6.3	Link benchmarking analysis	46
6.3.1	QO losses	47
6.3.2	Field matching	47
6.3.3	Receiver energy spectra and power	49
6.4	Conclusions	50
<b>7</b>	<b>Conclusions and future work</b>	<b>51</b>
7.1	Summary and conclusions	51
7.2	Future work	52
	<b>References</b>	<b>53</b>
<b>A</b>	<b>Time-domain Norton circuit</b>	<b>56</b>
<b>B</b>	<b>Primary far-fields of the array inside silicon.</b>	<b>57</b>
B.1	Primary far-field patterns	57
B.1.1	Amplitude patterns $h_{gap} = 0\mu m$	57
B.1.2	Amplitude patterns $h_{gap} = 10\mu m$	59
B.1.3	Amplitude patterns $h_{gap} = 25\mu m$	61
B.2	Phase error losses	63
<b>C</b>	<b>Center Embedded Element Pattern</b>	<b>64</b>
C.1	Far-field embedded pattern of the center element	64
C.1.1	$h_{gap} = 0\mu m$	64
C.1.2	$h_{gap} = 10\mu m$	68
C.1.3	$h_{gap} = 25\mu m$	72
C.2	Phase error losses	75
<b>D</b>	<b>Secondary fields fabricated PCCAs</b>	<b>76</b>
D.1	Secondary far-field patterns	76
D.1.1	Amplitude patterns $h_{gap} = 0\mu m$	76
D.1.2	Amplitude patterns $h_{gap} = 25\mu m$	78
D.2	Phase error losses	79
<b>E</b>	<b>Secondary fields redesigned PCCAs</b>	<b>80</b>
E.1	Secondary far-field patterns	80
E.1.1	Amplitude patterns $h_{gap} = 0\mu m$	80
E.1.2	Amplitude patterns $h_{gap} = 10\mu m$	82
E.2	Phase error losses	83
<b>F</b>	<b>Secondary fields leaky wave bow-tie PCA</b>	<b>84</b>
F.1	Secondary far-field patterns	84
F.2	Phase error losses	86
<b>G</b>	<b>Focal field amplitude patterns</b>	<b>87</b>
G.1	PCCA $h_{gap} = 0\mu m$	87
G.2	PCCA $h_{gap} = 10\mu m$	89
G.3	Leaky wave bow-tie PCA $h_{gap} = 10\mu m$	91
<b>H</b>	<b>PEL parabolic reflector fields</b>	<b>93</b>

# Nomenclature

## Abbreviations

Abbreviation	Definition
FoV	Field of View
GO	Geometrical Optics
SNR	Signal to Noise Ratio
THz-TDS	Terahertz Time Domain Spectroscopy
DoF	Depth of Field
EEP	Embedded Element Pattern
FWHM	Full Width at Half Maximum
HPBW	Half Power Beam Width
LW	Leaky wave
LW BT	Leaky Wave Bow-tie
PC	Photoconductive
PCA	Photoconductive antenna
PCCA	Photoconductive Connected Array
PEL	Phase Error Loss
PO	Physical Optics
QO	Quasi-Optical

# Introduction

Over the past 30 years, Terahertz (THz) technology has sparked the interest of both researchers and industry, due to its applicability in many fields. THz technology has been applied as a non-destructive testing technique in, for example, the medical and pharmaceutical sectors, and in the food industry; it is used in communications due to the large bandwidths available at these frequencies, and has found applications in security screening. [1, 2, 3, 4, 5]. Many of these applications were made possible by the introduction of Photoconductive Antennas (PCAs) at Bell Laboratories in 1984 [6]. PCAs use biased photoconductive semiconductor materials combined with optical sources to generate fast-changing feeding currents.

The basic working principle of PCAs is shown in Figure 1.1. A metalization that acts as an antenna is printed on top of a photoconductor (e.g. LT-GaAs). Over the photoconductive (PC) gap, a DC bias voltage is applied, and the PC gap is periodically illuminated with a laser pulse with a frequency larger than the band-gap frequency of the photoconductor. The illumination of the PC gap by the laser pulse causes electrons in the material to be promoted from the valence band to the conduction band. Due to the applied bias voltage, the free electrons in the conduction band will constitute a current in the feeding gap of the antenna placed on the photoconductor. The carriers in the photoconductor eventually recombine which puts the system into a steady state again where it is not radiating. Using a material with a recombination time in the order of a picosecond results in transient currents on the PC gap that last for a time in the order of picoseconds, meaning the concept of photoconductivity can be exploited to create broad band feeding currents for antennas [7]. An example of the shape of the laser power profile and the change in conductivity during a single laser pulse is shown in Figure 1.2.

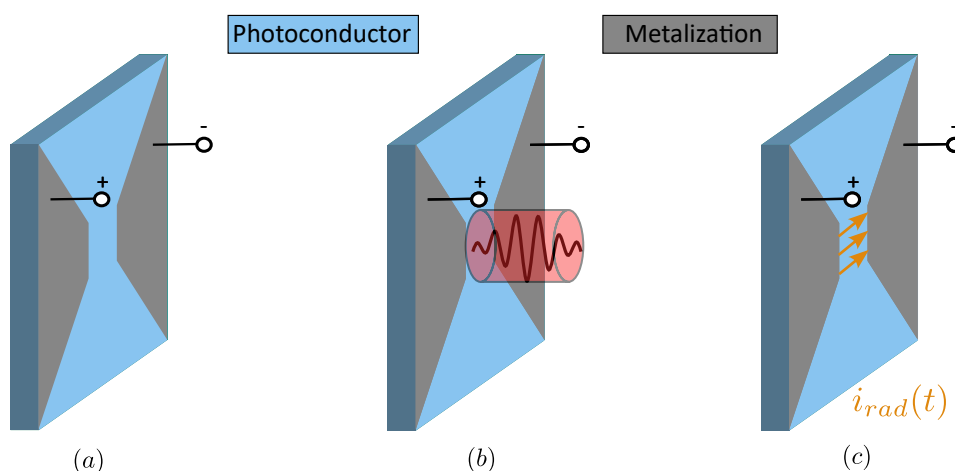


**Figure 1.1:** (a) Schematic of a PCA, where a bias voltage is applied between the two terminals. (b) A laser pulse is incident on the gap of the PCA, making the feeding gap of the antenna conductive. (c) The finite conductivity in the feeding gap and applied bias voltage allow for a time-varying current to flow, which is present until all the free charge carriers recombined.

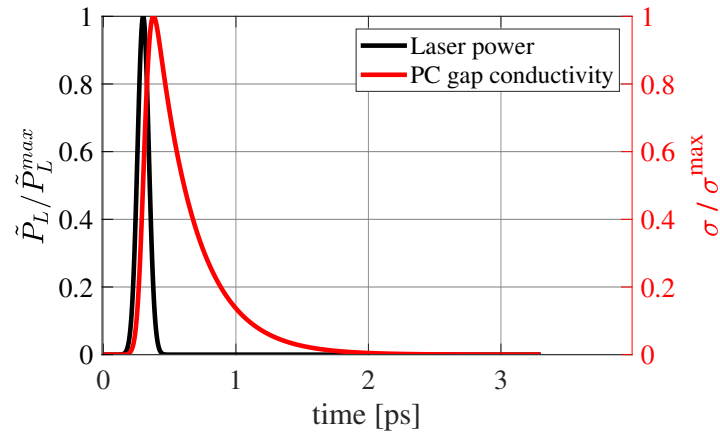


Figure 1.2: Example of the shape of the conductivity and laser power incident on the photoconductive gap over time.

## 1.1. State-of-the-art photoconductive antennas

The most widely used antenna geometries used in PCAs are the Auston-switch, bow-tie, and logarithmic spiral antenna. These geometries are often coupled to a silicon dielectric lens to enhance the front-to-back ratio and directivity [7, 8]. The aforementioned antennas coupled with dielectric lenses generally have a poor radiation efficiency due to high reflection losses inside the lens [9, 10]. Recently, a bow-tie PCA based on an LT-GaAs membrane has been introduced, allowing for the addition of a leaky-wave cavity to the lens feed [11]. The leaky wave bow-tie PCA geometry is shown in Figure 1.3. The addition of the leaky wave cavity increases the directivity of the field inside the lens, causing mostly the top part of the lens to be illuminated, which in turn gives the lowest amount of reflections [10].

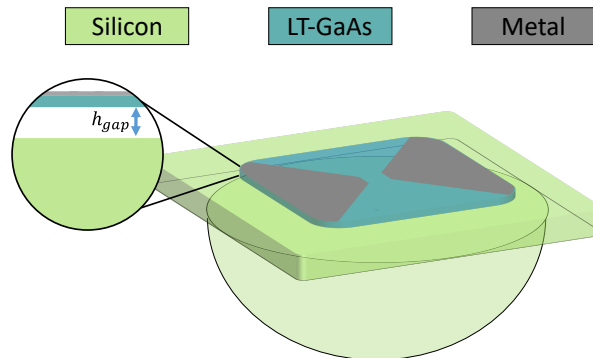


Figure 1.3: Schematic overview of the leaky wave bow-tie PCA antenna introduced in [11], where  $h_{gap} = 10 \mu\text{m}$ .

Single-element PCAs like the leaky wave bow-tie are however intrinsically limited in the amount of power they can radiate. Generally, PCAs radiate more power when either the laser power or bias voltage is increased. However, the photocurrent on the PC gap saturates when sufficiently increasing the bias voltage and/or the laser power. Furthermore, the maximum laser power is limited by thermal failure, and the maximum bias voltage is limited by the dielectric breakdown effects. To increase the radiated power, array-based PCAs have been introduced which are able to handle larger amounts of laser power before saturating. In [12], Garufo et al. introduced the Photoconductive Connected Array (PCCA) based on the concept of the connected array [13, 14] to efficiently radiate over a broad frequency band. The PCCA concept is discussed in detail in Chapter 2.

## 1.2. THz time-domain spectroscopy systems

PCAs are typically used within a Terahertz Time-Domain Spectroscopy (THz-TDS) system. A typical THz-TDS system is shown in Figure 1.4. The setup has a PCA in transmission and in reception. The transmitting PCA is biased by a voltage generator, while the receiving PCA is connected to an amplifier

to read out the received signal. The laser pulse is split by a beam splitter, where half of the power goes to the transmitter, and the other half goes to the receiver. Here the receiver works in a similar way as the transmitter: the incoming laser pulse promotes carriers to the conduction band, which are then accelerated by the incident electric field originating from the transmitter. The current measured at the receiver is then proportional to the strength of the electric field impinging on the receiver. The laser pulse going to the receiver travels via an optical path with variable delay. This makes it possible to sample different time instants of the incoming THz pulse and thus reconstruct the full pulse by varying the optical delay.

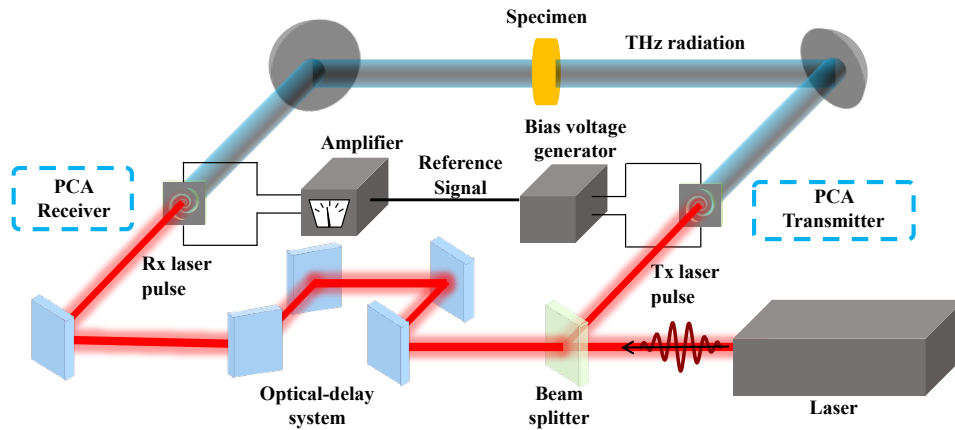


Figure 1.4: Schematic overview of a typical THz-TDS system setup [15].

The spectral information about the incoming field is found via the Fourier Transform of the reconstructed THz pulse. One can place a specimen in the QO path of the terahertz radiation, and by comparing the spectrum obtained when the specimen is present to the spectrum obtained without the specimen, spectral information of the specimen is obtained. In this work, several measurements that are obtained using a THz-TDS setup are discussed.

### 1.3. THz imaging systems

The THz frequency range is interesting for imaging, due to the high lateral resolution that can be obtained for limited aperture size at THz frequencies. Also, the large bandwidths available at THz frequencies allow for systems with a depth resolution in the order of a millimeter.

An interesting application for THz imaging systems is security screening. The high depth resolution allows for the distinction of different clothing layers, and the wide-band spectral information obtained from the sample gives information about the material. In [5], a real-time imaging radar at 675 GHz with a bandwidth of 29 GHz is presented for standoff personnel screening, which makes use of frequency multipliers based on Schottky diodes. The depth resolution of this system is in the order of a 1 cm, due to the 29 GHz bandwidth.

Photoconductive antennas are an interesting candidate for imaging systems in this frequency range due to their relatively low cost and their ability to provide a bandwidth in the order of hundreds of GHz. The large bandwidth of PCAs allows for sub-millimeter depth resolution. An imaging setup using photoconductive antennas would look similar to a THz-TDS system, where focusing components can be added to illuminate a small portion of the specimen. One can then scan the specimen to form a 3D image of the object. Typically PCA imaging setups suffer from long acquisition times due to low power arriving at the receiver, causing the need for long integration times to obtain an acceptable Signal to Noise Ratio (SNR) in wide Field-of-View (FoV) applications. However, for the state-of-the-art leaky wave bow-tie PCA and the PCCA, the power levels radiated reach the order of hundreds of microwatts, making them interesting for imaging applications where an acquisition time in the order of seconds is needed [11, 12, 16].

## 1.4. Scope of the thesis

This work is split up into two parts. The first part of the thesis is concerned with the characterization of PCCA antennas. In part two of this work, an imaging setup is designed and modeled for different PCAs, including the PCCA. An imaging setup is considered here to compare the performance of different state-of-the-art PCAs in an imaging scenario, and to lay the basis to build and use such an imaging setup in practice. More specifically:

- In Chapter 2 an analysis is done on the existing PCCA introduced by Garufo et al. To further increase the bandwidth of the PCCA, a leaky wave enhanced PCCA is introduced, characterized, and compared to the original PCCA design.
- In Chapter 3, a physical optics method is introduced to find the fields outside the dielectric lens of the PCCAs in a convenient way when the lens is in the near field region of the array. Furthermore, the effect of the losses associated with the lens on the spectra of the radiated fields and on the corresponding radiated power is quantified.
- In Chapter 4, a power measurement setup is modeled, and the measurements of two fabricated PCCA geometries are compared with the simulated results. This comparison provides useful information about the limitations of the current modeling procedure.
- In Chapter 5, the dielectric lenses of the PCCAs are redesigned such that the PCCAs couple well to a quasi-optical focusing component, which is necessary for the design of an imaging setup.
- Lastly, In Chapter 6 an imaging setup is designed to benchmark the different PCAs considered in this work. The coupling between transmitting and receiving PCAs in the imaging setup is studied via a field-matching formalism.

**Part I**

**Characterization of PCCAs**

# 2

## Photoconductive Connected Arrays

Single-element PCAs can only radiate a limited amount of power due to saturation effects that occur when increasing the optical power or biasing voltage. This restriction on the radiated power limits the applications of single-element PCAs in an imaging scenario, where low power causes long integration times [16]. To increase the power emitted, one can use an array of PCAs. Here, the increase in elements compared to a single-element PCA gives the potential to radiate more power, making them interesting candidates for imaging applications. Several array structures have been introduced, but typically the antenna configurations presented have limited radiation bandwidth due to the use of resonant elements [15]. Garufo et al. introduced the concept of a lens-coupled Photoconductive Connected Array (PCCA) of dipoles [12]. A connected array is beneficial compared to an array of more commonly used resonant elements due to the large bandwidths that connected arrays can obtain [13].

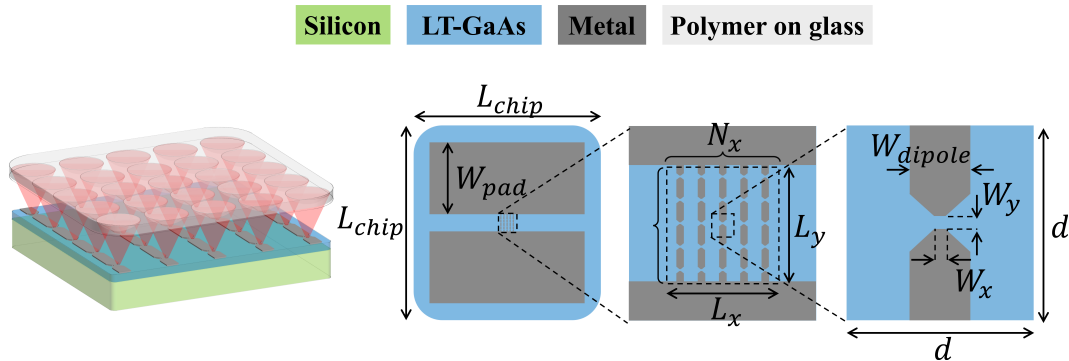


**Figure 2.1:** Schematic representation of the connected dipole array as presented in [12]. The values corresponding to the dimensions depicted in this figure can be found in Table 2.1.

**Table 2.1:** Table containing dimensions of the connected array structure presented in [12].

Parameter	Definition	Value
$L_{chip}$	Length of the chip including bias pads	6 mm
$L_x$	Length of connected array in x	500 $\mu\text{m}$
$L_y$	Length of connected array in y	500 $\mu\text{m}$
$W_{pad}$	Width of the biasing pads	2.25 mm
$N_x$	Number of dipole elements along x	5
$N_y$	Number of dipole elements along y	5
$W_{dipole}$	Width of the dipole elements	21.5 $\mu\text{m}$
$W_x$	Width of the feeding gap in x	7.5 $\mu\text{m}$
$W_y$	Width of the feeding gap in y	7.5 $\mu\text{m}$
$d$	Array period in x and y	100 $\mu\text{m}$

A schematic of the connected array can be seen in Figure 2.1. The array consists of 25 connected dipole elements, where the elements on the top and bottom are connected to a biasing source via metal pads with a width of  $W_{pad}$ . The metalization rests on top of a photoconductive layer of LT-GaAs with a thickness of  $h_{LT-GaAs} = 2 \mu\text{m}$ . During operation, laser pulses are periodically incident on an array of microlenses made out of polymer-on-glass. The microlens array focuses the laser pulses onto the photoconductive gaps of the dipole array. On top of the LT-GaAs layer, an extended hemispherical silicon lens with a radius of  $R_{lens} = 5 \text{ mm}$  is placed. A schematic view of the entire PCCA structure can be seen in Figure 2.2.

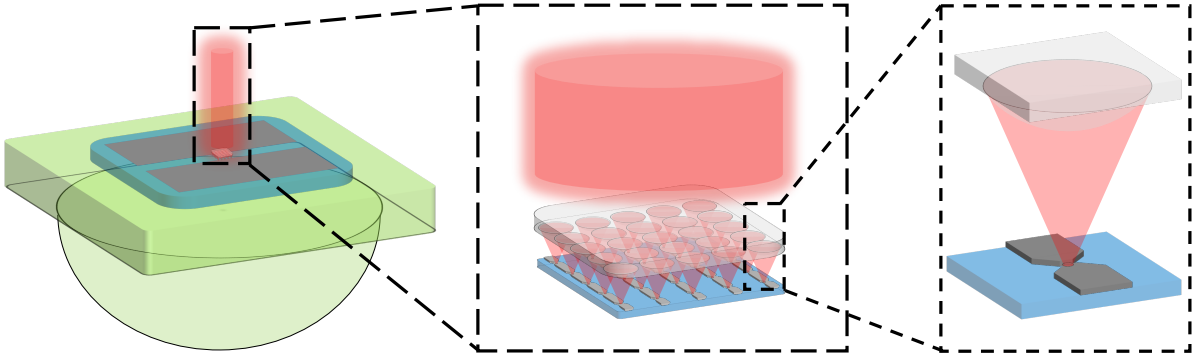


**Figure 2.2:** Schematic view of the PCCA structure introduced in [12], including extended hemispherical silicon lens. Note that this figure is not to scale.

Even though the PCCA introduced in [15] already has the potential to radiate significantly more power over a broader bandwidth compared to single-element PCAs, still the bandwidth of this connected array implementation is limited. The array period is set to  $d = 100 \mu\text{m}$  as this was the microlens array with the smallest period commercially available at the time of fabrication. This array period introduces a high-frequency cut-off due to grating lobes and destructive mutual coupling, which are both explained in Section 2.1. To diminish these negative effects and thus increase the bandwidth and radiated power, the possibility of adding a leaky-wave cavity to the structure is studied.

### Leaky-wave enhanced PCCA

In general, the performance of antennas coupled to dielectric lenses can often be enhanced by adding a leaky-wave cavity between the feeding antenna and the dielectric lens [17]. The added leaky-wave cavity allows for the shaping of the field radiated into the dielectric lens. In array structures, the leaky wave also can significantly impact the mutual coupling between elements [18].

This chapter examines the effect of adding an air cavity between the LT-GaAs layer and the silicon lens. More specifically, the effect of the LW cavity on the fields radiating into the silicon lens- and on the impedance of the array elements is quantified. The results are then used to clarify whether the leaky-wave enhanced PCCA is a better candidate to use in an imaging setup compared to the original PCCA without leaky wave cavity introduced in [12].

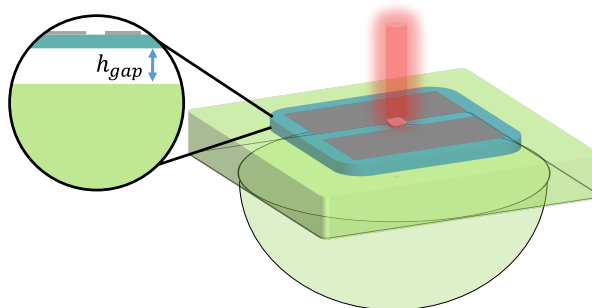


**Figure 2.3:** Schematic view of the leaky-wave PCCA structure. Note that this figure is not to scale.

## 2.1. Connected array analysis

In this section, the array is characterized by doing a full-wave simulation of the entire structure using CST [19] where the lens is simplified by a semi-infinite silicon medium. The effect of the silicon-air interface of the lens is discussed in Chapter 3. The stratification used is shown in Figure 2.4. All the dielectrics are considered lossless, and the metal is regarded as an infinitely thin Perfect Electric Conductor (PEC). Furthermore, the elements in the array are simultaneously excited.

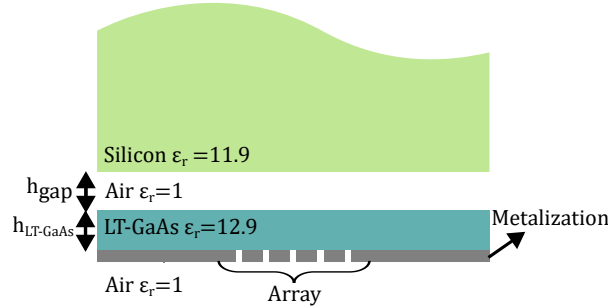


**Figure 2.4:** Simplified stratification that is used for the simulation of the connected array. The metalization represents in this case the metal that makes up the connected dipole elements and the biasing pads. The silicon layer on top and the air layer on the bottom are considered semi-infinite media.

Three different air gap heights  $h_{gap} = [0, 10, 25] \mu\text{m}$  will be considered in the results that follow. Here an air cavity of  $h_{gap} = 10 \mu\text{m}$  is chosen as it is the minimum air gap height that can be fabricated. The  $h_{gap} = 25 \mu\text{m}$  case is considered because it is the current dimension of a PCA fabricated by the TU Delft based on a leaky wave bow-tie [9]. Furthermore, a frequency range from 100 GHz to 1000 GHz is considered where the lower limit on the frequency range is because elements in the connected array are electrically small below 100 GHz and therefore the antenna will not work well. Furthermore, below 100 GHz, the lens cannot be simplified by an infinite dielectric for the considered lens geometries. This is further explained in Section 3.1.3.

### 2.1.1. Array impedance

The average active impedance of the above-mentioned  $5 \times 5$  finite array is shown in Figure 2.5 (active resistance) and Figure 2.6 (active reactance). Here, the impedance of an infinite array of connected dipoles is also included to verify the results.

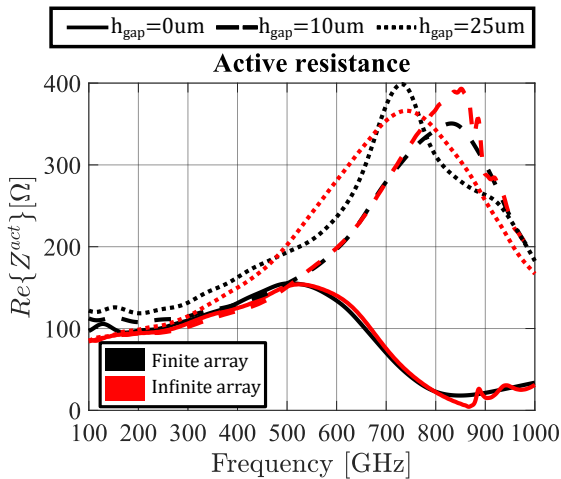


**Figure 2.5:** Average active resistance of the dipole elements in the connected array for different gap heights.

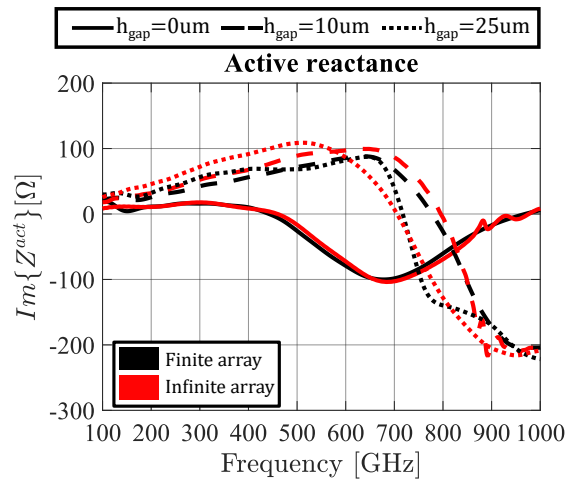


**Figure 2.6:** Average active reactance of the dipole elements in the connected array for different gap heights.

#### Impedance of the array without air cavity

Let us first consider the array without air gap ( $h_{gap} = 0 \mu\text{m}$ ). The presence of grating lobes is expected when the periodicity of the array becomes larger than a wavelength inside silicon. This happens for

frequencies larger than the grating lobe frequency  $f_{GL}$ , which is defined as:

$$f_{GL} = \frac{c_0}{d\sqrt{\epsilon_r^{Si}}} \approx 870 \text{ GHz} \quad (2.1)$$

When the grating lobes appear, one expects a drop in the active resistance [14]. Indeed, in Figure 2.5, the active resistance becomes almost zero around  $f_{GL}$ . The active resistance, in general, is associated with the radiated power of the antenna. Thus the near-zero active resistance due to the grating lobes will limit the operational bandwidth.

However, the active resistance already starts to drop before the grating lobes appear. This effect can be attributed to the intrinsic behavior of connected arrays [13][20]. A high-frequency cut-off is present because of destructive mutual coupling between the dipole elements in the array. This effect starts to be visible when the array period  $d$  approximately becomes larger than  $\frac{\lambda_{eff}}{2}$ . Here,  $\lambda_{eff}$  is defined as the effective wavelength and is calculated using an effective relative permittivity  $\epsilon_r^{eff} = (\epsilon_r^{air} + \epsilon_r^{Si})/2$ . The resulting cut-off frequency is then calculated as follows:

$$f_{cut} = \frac{c_0}{2d\sqrt{\epsilon_r^{eff}}} \approx 590 \text{ GHz} \quad (2.2)$$

Intuitively, this destructive mutual coupling effect can be explained as follows: for a small array period in terms of the wavelength ( $d < \frac{\lambda_{eff}}{2}$ ), the field contributions due to each of the individual elements add coherently, and the structure essentially behaves as a single radiator. When the array period becomes in the order of  $\frac{\lambda_{eff}}{2}$ , the elements start to behave like individual radiators, resulting in non-coherent field summation, which causes a drop in the impedance.

### Effect of an air-cavity on the array impedance

The addition of an air cavity between the radiating structure and the lens decreases the effective permittivity, which in turn increases the effective wavelength. The increase in effective wavelength pushes the high-frequency cut-off in the active resistance due to the destructive mutual coupling to higher frequencies, as shown by the peaks in Figure 2.5. Also, the zero in the real part of the impedance associated with the grating lobes is pushed to higher frequencies as is evident from Figure 2.5. The reason for this effect is given in Section 2.1.2.

### 2.1.2. Far-fields inside the lens medium (primary fields)

Besides the active impedance, one can also analyze the far fields radiated by the array inside the lens medium (silicon). These fields are referred to as the primary fields and are shown from Figure 2.7 to Figure 2.12 for 400 GHz, 700 GHz and 1000 GHz. The amplitude patterns for all simulated frequencies can be found in Appendix B. Note that only the co-polar components are shown, as the cross-polar components are not visible on this scale.

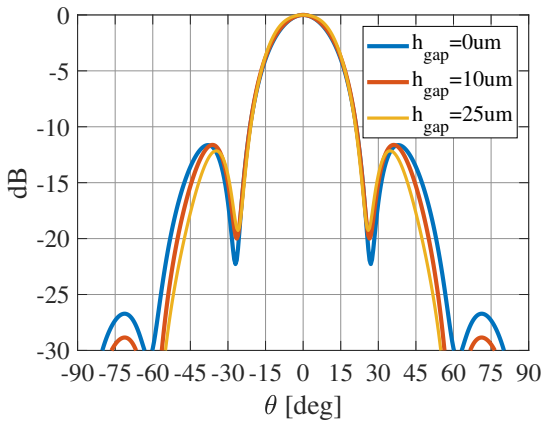


**Figure 2.7:** Far-field magnitude of the electric field inside silicon for  $f = 400 \text{ GHz}$ , for  $\phi = 0^\circ/180^\circ$ .

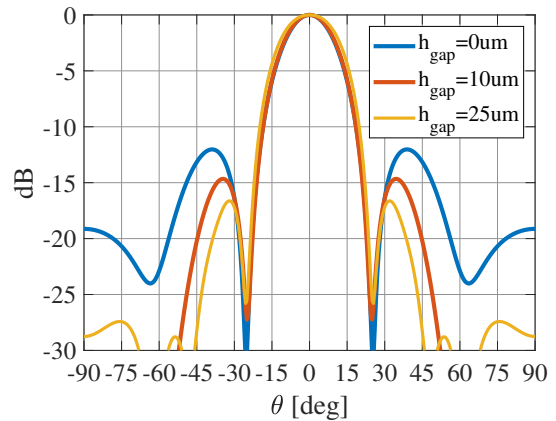


**Figure 2.8:** Far-field magnitude of the electric field inside silicon for  $f = 400 \text{ GHz}$ , for  $\phi = 90^\circ/270^\circ$ .

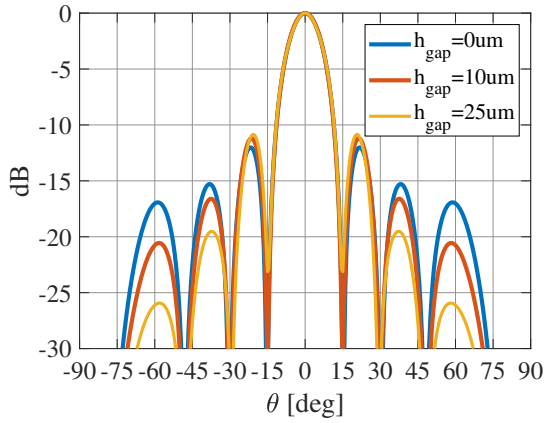


**Figure 2.9:** Far-field magnitude of the electric field inside silicon for  $f = 700GHz$ , for  $\phi = 0^\circ/180^\circ$ .

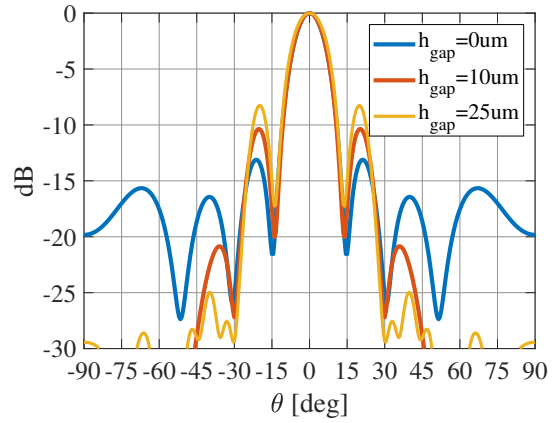


**Figure 2.10:** Far-field magnitude of the electric field inside silicon for  $f = 700GHz$ , for  $\phi = 90^\circ/270^\circ$ .

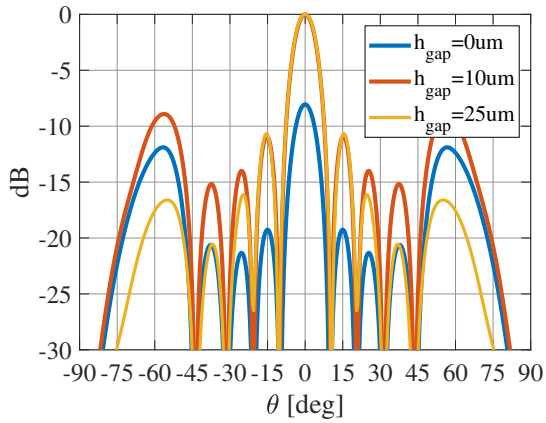


**Figure 2.11:** Far-field magnitude of the electric field inside silicon for  $f = 1000GHz$ , for  $\phi = 0^\circ/180^\circ$ .

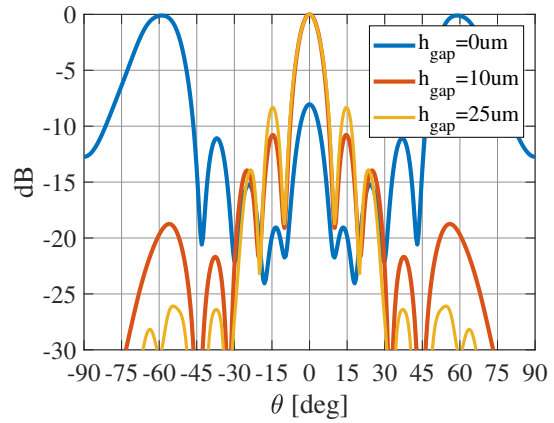


**Figure 2.12:** Far-field magnitude of the electric field inside silicon for  $f = 1000GHz$ , for  $\phi = 90^\circ/270^\circ$ .

For  $f < f_{GL}$ , the field amplitude patterns are very similar for the considered values of  $h_{gap}$ . However, for  $f > f_{GL}$  it is evident from Figure 2.12 that the addition of an air-gap has the positive side-effect that it strongly suppresses the grating lobes in the  $\phi = 90^\circ/270^\circ$  plane. This grating lobe suppression can be explained by the excited leaky waves which enlarge the effective area along this direction. This in turn causes the array element patterns to become more directive, resulting in less radiation in the direction of the grating lobes. In Figure 2.13a the embedded pattern of the centre element is shown for different  $h_{gap}$  to illustrate this effect.

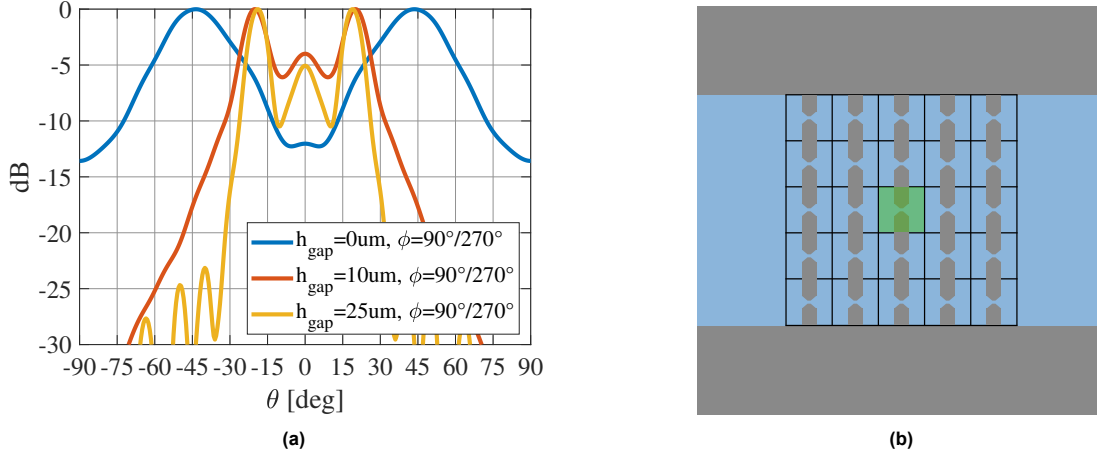


**Figure 2.13:** (a) Magnitude of the radiation pattern of the center element, radiating in the presence of the other elements for  $\phi = 90^\circ/270^\circ$ . The embedded center patterns at all considered frequencies can be found in Appendix C (b) Connected array with the center element highlighted in green.

### 2.1.3. Phase center

When one feeds a quasi-optical (QO) component, the phase center of the feed should be placed at the focus of the QO component, which in this case is a dielectric lens. In reality, antennas usually do not have a true phase center, in the sense that the phase front is not truly flat over a sphere in the far field, and the phase center position changes with frequency. Thus in practice, a frequency-dependent phase-loss is present due to the non-uniform phase distribution of the field arriving at the QO component. This Phase-Error-Loss (PEL) is defined as follows:

$$\text{PEL}(\Delta_z) = \frac{\left| \int_0^{2\pi} \int_0^{\theta_{MB}} E_{co}(\theta, \phi) e^{jk_z \Delta_z} \sin(\theta) d\theta d\phi \right|^2}{\left( \int_0^{2\pi} \int_0^{\theta_{MB}} |E_{co}(\theta, \phi)| \sin(\theta) d\theta d\phi \right)^2} \quad (2.3)$$

From Equation 2.3 one can find an approximate phase center position that minimizes the phase losses over a certain solid angle and frequency band. Here  $\Delta_z$  indicates the shift of the reference system in the negative  $-\hat{z}$  direction. The approximate phase center position is expected to lie along the  $\hat{z}$  direction (normal to the array), as the far fields are symmetric in  $\phi$ . The co-polarized field is denoted by  $E_{co}(\theta, \phi)$ . The main beam angle  $\theta_{MB}$  is defined as the angle from broadside to where the field is  $-15$  dB.

The PEL vs. frequency is shown for different air-gap sizes in Appendix B.2. For the approximate phase center of the feed  $\Delta_{PC}^{feed}$ , a value of  $\Delta_z$  that gives a low PEL over a large frequency band is chosen by inspection. The approximate phase centers of the fields radiating into silicon are given in Table 2.2.

**Table 2.2:** Phase centers of the far-fields of the PCCA array radiating into silicon.

$h_{gap} [\mu\text{m}]$	$\Delta_{PC}^{feed} [\mu\text{m}]$
0	132
10	282
25	443

Note here that a positive value of  $\Delta_{PC}^{feed}$  means that the structure should be shifted upwards to align the focus with the phase center, which implies a phase center located under the origin of the structure.

### 2.1.4. Front-to-back efficiency

So far, the radiation into the lens medium has been considered. However, part of the radiation goes to the backside of the array, and we consider this portion of the power as a loss. To quantify this loss, we can define a front-to-back efficiency  $\eta_{f2b}$  of the antenna as follows:

$$\eta_{f2b}(f) = \frac{P_{prim}^{up}(f)}{P_{prim}^{tot}(f)} \quad (2.4)$$

Where  $P_{prim}^{tot} = P_{prim}^{down} + P_{prim}^{up}$ ,  $P_{prim}^{down}$  is the power radiated to the back side of the array, and  $P_{prim}^{up}$  is the power radiated into the lens medium. Figure 2.14 shows a schematic overview of the stratification, where the field radiated by the feed has its origin in the phase center.

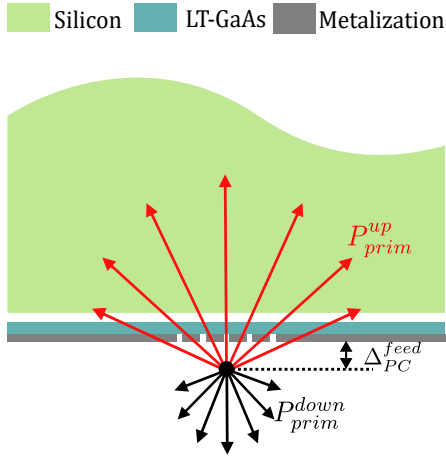


**Figure 2.14:** Schematic overview of the stratification where the red arrows indicate the power radiated upwards into the semi-infinite silicon layer. The black arrows represent the power radiated downward into the air.

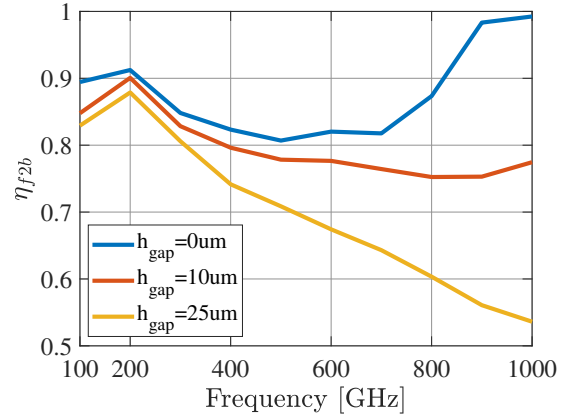


**Figure 2.15:** Front-to-back efficiency of the array for the stratification considered in Figure 2.4.

In Figure 2.15, the front-to-back efficiency is shown for the values of  $h_{gap}$  considered. It is evident that adding an air gap decreases the front-to-back efficiency, and the front-to-back efficiency goes down as  $h_{gap}$  increases.

## 2.2. Energy spectrum and radiated power

In previous sections, the arrays are quantified in terms of front-to-back, impedance, and radiation patterns. A significant quantity of interest that still should be considered is the spectrum of the energy generated in the PC gap and the associated power. The energy spectrum and power depend on several physical parameters, including the amount of incident laser power and biasing voltage. In [9], an equivalent Norton circuit is introduced that characterizes the voltage and current distributions in the load of a single photoconductive source. The characterization is done starting from the Drude-Lorentz model, which describes the movement of charge carriers in the PC gap over time. In this chapter, only results of the derivation from [9] are used.

Using the voltage and current distributions on the photoconductive load, the energy spectra of the voltage and current on the antenna load and the associated power generated by the PC source can be found. Figure 2.16 shows a schematic representation of the Norton circuit.

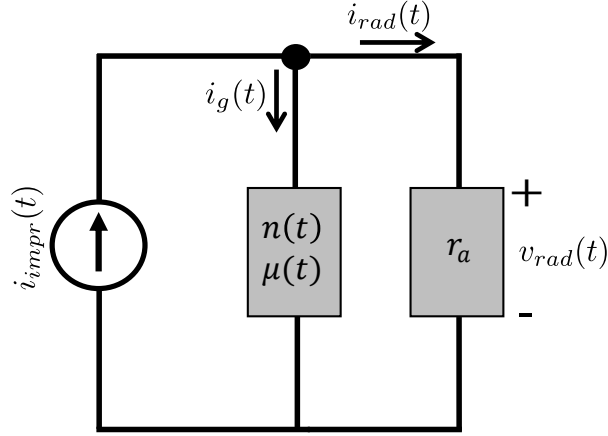


**Figure 2.16:** Circuit diagram of the equivalent PCA Norton circuit. Here the  $n(t), \mu(t)$  component represents the photoconductive gap, and  $r_a$  represents the antenna radiation resistance.

Note here that in the circuit model in Figure 2.16, the antenna is represented by a real radiation resistance  $r_a$ . Approximating the impedance of the antenna by a real radiation resistance is valid for electrically long broadband antennas. The photoconductive gap is represented by the “ $n(t)\mu(t)$ ” component. Here  $n(t)$  and  $\mu(t)$  refer to the charge carrier density inside the PC gap and the mobility of the charge carriers, respectively.

The equations for the impressed current  $i_{impr}(t)$  and the generator current  $i_g(t)$  can be found in Appendix A. For the evaluation of the spectrum of the energy on the PC gap,  $E_s(f)$ , the radiation current going to the antenna load  $i_{rad}(t)$  is necessary. From the steps listed in [9], one can arrive at the set of equations used to evaluate  $i_{rad}(t)$ :

$$i_{rad}(t) = \frac{q_e^2}{m_e} \frac{W_y W_z}{W_x} A \int_{-t_{min}}^t e^{-4 \ln 2 \frac{t''^2}{\tau_p^2}} \int_{t''}^t e^{-\frac{t-t'}{\tau_s}} (V_b - v_{rad}(t')) dt' e^{-\frac{t-t''}{\tau_c}} dt'' \quad (2.5a)$$

$$v_{rad}(t) = i_{rad}(t) r_a \quad (2.5b)$$

Equation 2.5 can be solved numerically using a “march-in-time” technique, where the scheme is initialized with  $v_{rad}(t = t_{min}) = 0$  and  $i_{rad}(t = t_{min}) = 0$ . The parameter  $A$  is defined as:

$$A = \eta_{opt} \frac{\tilde{P}_L}{N_x N_y h f_c} \frac{T_L}{\tau_p} \sqrt{\frac{4 \ln 2}{\pi}} \frac{1}{Vol} \quad (2.6)$$

The definitions and values of the parameters that are considered fixed when evaluating the Norton circuit in this thesis are listed in Table 2.3. The definition of the variable parameters are listed in Table 2.4.

**Table 2.3:** Fixed parameters used in the time-domain Norton equivalent circuit.

Variable	Definition	Value
$q_e$	Electron charge	$\approx 1.602 \times 10^{-19} \text{ C}$
$m_e$	Electron mass	$\approx 9.109 \times 10^{-31} \text{ Kg}$
$W_x, W_y$	Dimension of the photoconductor gap in x and y respectively	$7.5 \mu\text{m}$
$W_z$	Dimension of the photoconductor gap in z	$2 \mu\text{m}$
$\tau_p$	Pulsed laser time constant	$0.1 \text{ ps}$
$\tau_s$	Electron scattering time	$8 \text{ fs}$
$\tau_c$	Electron recombination time	$300 \text{ fs}$
$\Gamma$	Reflection coefficient at the photoconductor-air interface	$0.5657$
$\alpha$	Laser absorption coefficient	$1 \times 10^6 \text{ m}^{-1}$
$T_L$	Laser repetition period	$12.5 \times 10^{-9} \text{ s}$
$f_c$	Laser carrier frequency	$385 \text{ THz}$
$Vol$	Volume of the photoconductor gap	$W_x \cdot W_y \cdot W_z$

**Table 2.4:** Variable parameters used in the time-domain Norton equivalent circuit.

Variable	Definition
$V_b$	Applied bias voltage on a single gap
$\eta_{opt}$	Optical efficiency
$\tilde{P}_L$	Average power of the laser

The spectrum of the energy  $E_s(f)$  generated in a single PC gap can then be found as:

$$E_s(f) = \Re\{Z_a(f)\}|I_{rad}(f)|^2 \quad (2.7)$$

Here the antenna impedance is denoted as  $Z_a$ .

### 2.2.1. Optical efficiency

Several laser power losses occur along the laser path from the Menlo Tera K15 system to being absorbed in the PC gap. Here a loss means that this part of the power does not contribute to changing the conductivity in the PC gap. The optical efficiency which quantifies the laser power losses is then defined as:

$$\eta_{opt} = \eta_{SO,Laser}^{ML} \eta_{SO,Laser}^{Gap} (1 - e^{-\alpha W_z})(1 - \Gamma^2) \quad (2.8)$$

Here, the factor  $(1 - e^{-\alpha W_z})$  takes into account the absorption losses in the PC gap, and the factor  $(1 - \Gamma^2)$  takes into account the reflection losses that occur at the interface between air and the photoconductor (LT-GaAs). The parameters  $\alpha$ ,  $W_z$  and  $\Gamma$  are defined as in Table 2.3.

The remaining losses in the optical path can be attributed to spillover losses. The first spillover loss is on the microlens array, which is quantified by the microlens spillover efficiency  $\eta_{SO,Laser}^{ML}$ . The spatial power profile of the laser incident on the microlens array  $S_{laser}^{ML}(x, y)$  is approximately Gaussian and can be expressed as:

$$S_{laser}^{ML}(x, y) = A_{Gauss} \cdot e^{-\frac{(x^2+y^2)(4 \ln 2)}{D_{laser}^2}} \quad (2.9)$$

Here,  $A_{Gauss}$  is an arbitrary amplitude of the incident laser, and  $D_{laser}$  represents the  $-3$  dB beamwidth of the laser. The laser spillover efficiency on the microlens array  $\eta_{SO,laser}^{ML}$  is then found as:

$$\begin{aligned} \eta_{SO,laser}^{ML} &= \frac{\int_{-\frac{L_y}{2}}^{\frac{L_y}{2}} \int_{-\frac{L_x}{2}}^{\frac{L_x}{2}} S_{laser}^{ML}(x, y) dx dy}{\int_{-\infty}^{\infty} \int_{-\infty}^{\infty} S_{laser}^{ML}(x, y) dx dy} \\ &= \frac{4 \ln 2}{\pi D_{laser}^2} \int_{-\frac{L_y}{2}}^{\frac{L_y}{2}} \int_{-\frac{L_x}{2}}^{\frac{L_x}{2}} e^{-\frac{(x^2+y^2)(4 \ln 2)}{D_{laser}^2}} dx dy \end{aligned} \quad (2.10)$$

Generally, the laser beam diameter at  $-3$  dB is set to be the same as the array size,  $D_{laser}^{ideal} = L_x = L_y$ , such that the array is approximately uniformly excited. Evaluating Equation 2.10 for this case yields the "Ideal" spillover efficiency on the microlens array of  $\eta_{SO,laser}^{ML,ideal} = 0.580$ .

Spill-over also occurs on the photoconductive feeding gap of the dipoles and is quantified by the gap spillover efficiency  $\eta_{SO,Laser}^{Gap}$ . The field in the focused spot of the photoconductive gap can be approximated by an Airy pattern, assuming the field distribution on the receiving side of each microlens is approximately uniform. The spatial power profile of the focused spot is then given by:

$$S_{laser}^{Spot}(\theta) = A_{Airy} \cdot \left[ \frac{J_1(k \cdot R_{ML} \cdot \sin(\theta))}{k \cdot R_{ML} \cdot \sin(\theta)} \right]^2 \quad (2.11)$$

In Equation 2.11 again an arbitrary amplitude  $A_{Airy}$  is used. Here  $k$  is the wavenumber corresponding to the laser illumination, and  $R_{ML}$  is the radius of a single microlens. The spillover efficiency on the PC gaps,  $\eta_{SO,laser}^{Gap}$ , can then be evaluated as follows:

$$\eta_{SO,laser}^{Gap} = \frac{\int_{-\frac{W_y}{2}}^{\frac{W_y}{2}} \int_{-\frac{W_x}{2}}^{\frac{W_x}{2}} S_{laser}^{Spot}(x, y) dx dy}{\int_{-\infty}^{\infty} \int_{-\infty}^{\infty} S_{laser}^{Spot}(x, y) dx dy} \quad (2.12)$$

On the PC gaps, the gap size is approximately matched to the  $-3$  dB diameter of the focussed spot  $D_{spot} = 1.02 f_{\#}^{ML} \lambda_0 = 7.55 \text{ um}$ . Here  $f_{\#}^{ML}$  is the f-number of the microlenses in the microlens array. The spillover efficiency on the PC gaps assuming each individual lens is uniformly illuminated, is found to be  $\eta_{SO,laser}^{Gap,Ideal} = 0.537$

### 2.2.2. Application of the TD Norton circuit to a PCCA

In this section, the TD Norton circuit is used to evaluate the energy spectrum of a PCCA. The radiation resistance  $r_a$  used to evaluate Equation 2.5 for the different PCCAs can be found in Table 2.5. These values are chosen to approximately match the radiation resistance, as seen in Figure 2.5, over a large band. If one wants to take into account the time-domain behavior of the PCCA fully, the antenna impulse response should be used. However, this is not possible with the current formulation because it requires the knowledge of  $i_{rad}$  before starting the march-in-time procedure. Thus throughout this thesis, the evaluation of the Norton equivalent circuit for all PCCAs will be done using the values considered in Table 2.5, while keeping it in mind as a possible source of error.

**Table 2.5:** Approximated real radiation resistance of the PCCAs considered, used for the evaluation of the Norton TD circuit.

$h_{gap} [\mu m]$	Approximated $r_a [\Omega]$
0	100
10	150
25	200

The spectrum of the total energy radiated by a PCCA can be approximated by summing the spectra of the individual PC gaps in the array, as is done below [12]:

$$E_{s,array}(f) = \sum_{n_x} \sum_{n_y} E_{s,(n_x,n_y)}(f) = \sum_{n_x} \sum_{n_y} \Re\{Z_{a,(n_x,n_y)}(f)\} |I_{rad}(f)|^2, \quad (2.13)$$

for  $n_x = -2, \dots, 2$  &  $n_y = -2, \dots, 2$

Here  $n_x$  and  $n_y$  represent the indices of the array elements in x and y respectively and are defined as shown in Figure 2.18. Furthermore  $I_{rad}(f) = \mathcal{F}\{i_{rad}(t)\}$ . The laser power across the array is assumed to be uniformly distributed, and the laser power that is incident on the individual PC gaps is given by:

$$\tilde{P}_{gap} = \frac{\tilde{P}_L \cdot \eta_{SO,laser}^{ML} \cdot \eta_{SO,laser}^{Gap}}{N_x N_y} \quad (2.14)$$

Furthermore the bias voltage  $V_b$  is assumed to be the same across all elements. Due to the assumptions on the bias voltage and laser power distributions, all the elements have the same  $i_{rad}(t)$ . An example of  $i_{rad}$  computed using the Norton circuit for the values of  $h_{gap}$  considered is shown in Figure 2.17. The active impedance of an individual element in the array is denoted by  $Z_{a,(n_x,n_y)}$ .

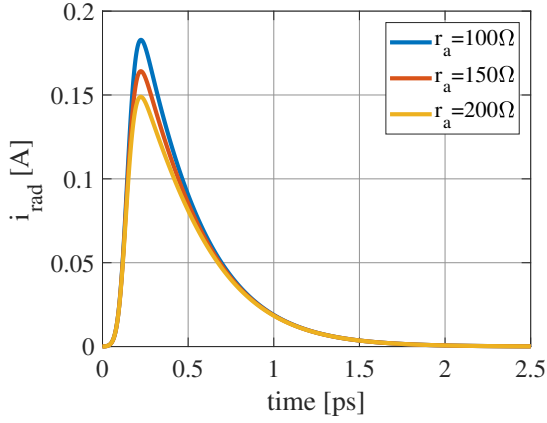


**Figure 2.17:** Radiation currents going to the load for different  $r_a$  corresponding to the values of  $h_{gap}$  considered. For the evaluation of the Norton circuit, the following variable parameters are used  $\eta_{SO,laser}^{ML} = \eta_{SO,laser}^{ML, Ideal} = 0.580$  and  $\eta_{SO,laser}^{Gap} = \eta_{SO,laser}^{Gap, Ideal} = 0.537$ ,  $V_b = 80$  V,  $\tilde{P}_L = 178$  mW.

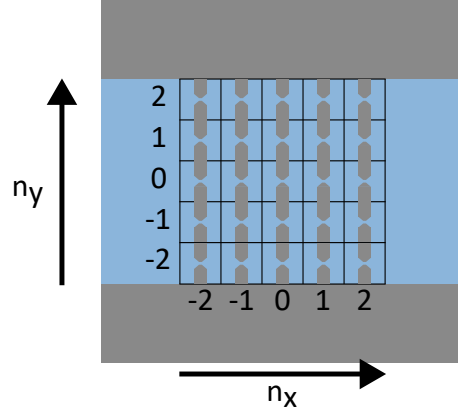


**Figure 2.18:** Connected array including element indices.

The energy spectral density of the upward radiation  $E_{s,array}^{up}(f)$  into the silicon medium can be found by multiplying the spectrum by the front-to-back efficiency:

$$E_{s,array}^{up}(f) = \eta_{f2b}(f) \cdot E_{s,array}(f) \quad (2.15)$$

An example of the resulting spectra is shown in Figure 2.19.

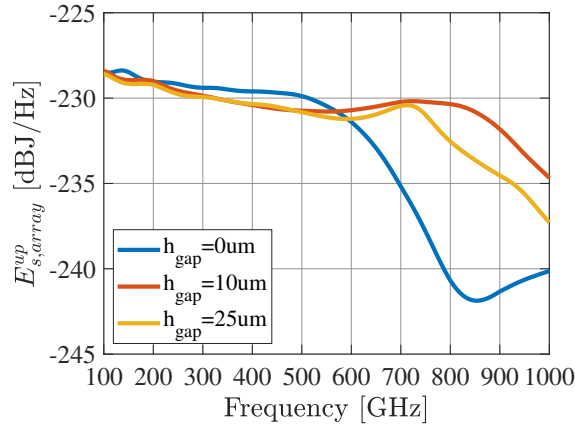


**Figure 2.19:** Energy spectral densities of the primary fields radiating into a semi-infinite silicon medium. For the evaluation of the Norton circuit, the following variable parameters are used  $\eta_{SO,laser}^{ML} = \eta_{SO,laser}^{ML, Ideal} = 0.580$  and  $\eta_{SO,laser}^{Gap} = \eta_{SO,laser}^{Gap, Ideal} = 0.537$ ,  $V_b = 80$  V,  $\tilde{P}_L = 178$  mW.

The average power radiated into the silicon for a periodically excited PCCA with a laser repetition period of  $T_L$  is expressed as:

$$P_{rad}^{Si} = \frac{2}{T_L} \int_0^{\infty} E_{s,array}^{up}(f) df \quad (2.16)$$

Here a frequency range from 100 GHz to 1000 GHz is used to evaluate Equation 2.16. For the energy spectra in Figure 2.19 the associated radiated powers are given below:

**Table 2.6:** Power radiated into the silicon medium associated with the spectra in the example case of Figure 2.19

$h_{gap}[\mu m]$	$P_{rad}[mW]$
0	1.04
10	1.32
25	1.16

## 2.3. Conclusions

To increase the radiated power of single-element PCAs, the PCCA was introduced by [12]. However, the connected array used in the PCCA design by Garufo is still limited in bandwidth due to the presence of grating lobes and destructive mutual coupling effects. Adding a leaky-wave cavity to the structure improved the bandwidth of the connected array. This improvement is due to the enlargement of the effective area that comes with the leaky wave, which pushes the grating lobes and destructive mutual coupling effects to higher frequencies. Here an air gap of  $h_{gap} = 10\mu m$  is found to have a larger bandwidth and radiated power compared to the  $h_{gap} = 25\mu m$  case. From both the increase in bandwidth, radiated power, and the suppressed grating lobes one can conclude that the use of the  $h_{gap} = 10\mu m$  PCCA is generally expected to have superior performance when feeding a dielectric lens.

# 3

## Physical Optics simulations for dielectric lenses

In Chapter 2, the primary fields inside the silicon lens are simulated and analyzed for the investigated PCCAs. In this chapter, the effect of the dielectric lens is considered. More specifically, a Physical Optics (PO) method is used to evaluate the fields radiated by the silicon lens, using the primary fields evaluated in the previous chapter. A quantitative review is first given explaining the PO method as used in previous works concerning PCA coupled dielectric lenses [15] [9] [21]. Then, a modification to the previous method is discussed specifically for large array-based feeds in combination with small dielectric lenses, where the lens surface is in the near-field with respect to the array. Subsequently, several efficiency terms are defined to quantify the effect of the dielectric lens on the radiated power. Using these efficiency terms, the spectra of the fields radiated by several fabricated PCCA structures and the associated radiated powers are evaluated.

### 3.1. PO analysis for a hemispherical lens

To get the fields radiated by the silicon lens into air, an in-house PO tool is employed [22], of which the general concept is discussed in this section. The PCCA geometries considered have an extended hemispherical silicon lens of which a schematic drawing is shown in Figure 3.1.

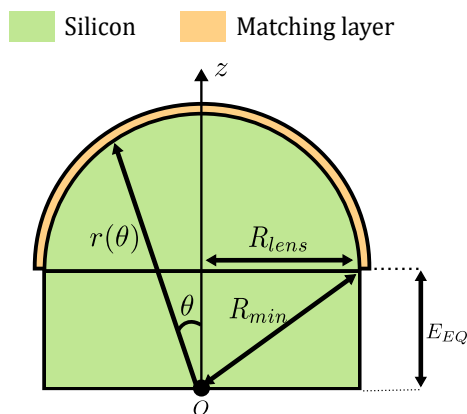


**Figure 3.1:** Schematic of the geometry of a hemispherical lens including a matching layer.

The extended hemispherical lens shown in Figure 3.1 has a radius denoted by  $R_{lens}$  and an equivalent extension length of  $E_{EQ}$ . The lower focus of the lens is denoted by  $O$ , where the focus of the lens is aligned with the phase center of the feed. The radial distance from the lower focus to the lens surface is denoted by  $r(\theta)$ , and is expressed analytically as follows [22]:

$$r(\theta) = E_{EQ} \cos \theta + \sqrt{R_{lens}^2 - E_{EQ}^2 \sin^2 \theta} \quad (3.1)$$

The distance from the focus of the lens to the edge of the hemisphere is denoted by  $R_{min}$ , and is expressed as follows:

$$R_{min} = \sqrt{E_{EQ}^2 + R_{lens}^2} \quad (3.2)$$

### 3.1.1. PO procedure

To obtain the radiated fields of the lens antenna, the equivalent currents ( $\vec{J}_s, \vec{M}_s$ ) on the lens surface should be evaluated. These equivalent currents are calculated in several steps. First, the incident field on the inner lens surface is evaluated using the primary far-field of the feed. Note here that the phase center of the primary field is aligned with the focus of the lens, and that the lens should be in the far field of the feed. The incident field on the inner lens surface is then transmitted outside the lens surface following Snell's law, where the lens surface is assumed to be locally flat. Here, a quarter-wavelength matching layer is implemented to improve the transmission at the dielectric-air interface. For the evaluation of the equivalent current on the lens surface, two approximations are used which are referred to as the PO approximations. The first approximation is that the equivalent currents are calculated using only the transmitted fields on the lens surface ( $\vec{E}_T, \vec{H}_T$ ). The second approximation is that the equivalent currents are zero outside the lens surface. The transmitted fields are then used to calculate the equivalent currents as follows:

$$\vec{J}_{EQ} \approx \hat{n}_Q \times \vec{H}_T \quad (3.3a)$$

$$\vec{M}_{EQ} \approx -\hat{n}_Q \times \vec{E}_T \quad (3.3b)$$

The fields radiated by the equivalent currents, referred to as the secondary fields ( $\vec{E}_{sec}, \vec{H}_{sec}$ ), are subsequently found using the Green's function equations:

$$\vec{E}_{sec}(\vec{r}) = \int_Q j\vec{k} \times \vec{M}_{EQ} \frac{e^{-jk|\vec{r}-\vec{r}'|}}{4\pi|\vec{r}-\vec{r}'|} d\vec{r}' - j\omega\mu \int_Q [\vec{J}_{EQ} - (\hat{k} \cdot \vec{J}_{EQ})\hat{k}] \frac{e^{-jk|\vec{r}-\vec{r}'|}}{4\pi|\vec{r}-\vec{r}'|} d\vec{r}' \quad (3.4a)$$

$$\vec{H}_{sec}(\vec{r}) = -\frac{jk}{\zeta} \int_Q [\vec{M}_{EQ} - (\hat{k} \cdot \vec{M}_{EQ})\hat{k}] \frac{e^{-jk|\vec{r}-\vec{r}'|}}{4\pi|\vec{r}-\vec{r}'|} d\vec{r}' - \int_Q j\vec{k} \times \vec{J}_{EQ} \frac{e^{-jk|\vec{r}-\vec{r}'|}}{4\pi|\vec{r}-\vec{r}'|} d\vec{r}' \quad (3.4b)$$

Here,  $\vec{r}$  is the observation point and  $\vec{r}'$  is a point on the lens surface. Furthermore, the propagation unit vector is defined as  $\hat{k} = \frac{\vec{r}-\vec{r}'}{|\vec{r}-\vec{r}'|}$  and the propagation vector as  $\vec{k} = k\hat{k}$  with  $k$  being the wave number of the medium. A schematic drawing of a hemispherical lens including an illustrative ray-tracing of the primary and secondary field is shown in Figure 3.2.

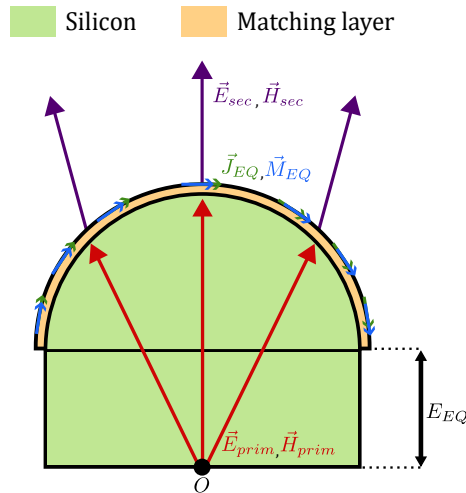
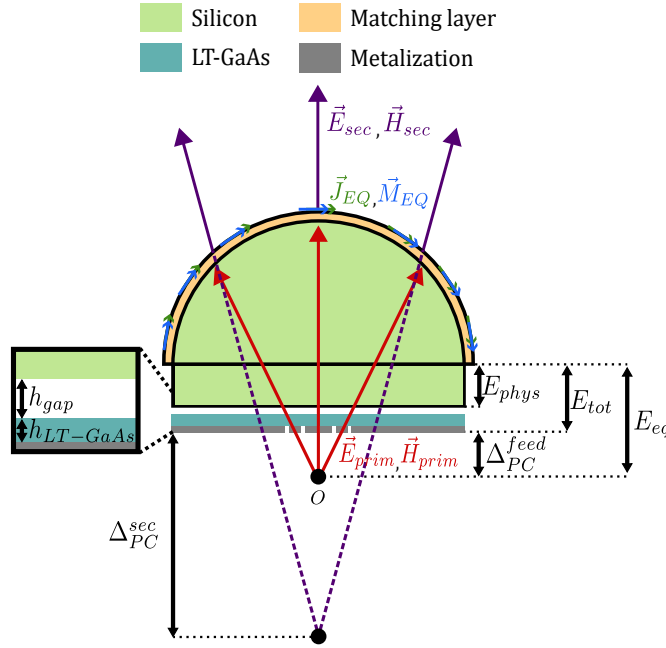


Figure 3.2: Illustrative ray-tracing of the primary field

### 3.1.2. Full PCCA lens geometry

When fabricating the PCCA, one has to make sure the phase center of the feed is aligned with the focus of the hemispherical lens. The connected array feeds investigated in this work have a phase center that is below the radiating structure, which means the array is located above the focus. A schematic overview of the full PCCA structure is shown in Figure 3.3.



**Figure 3.3:** Schematic drawing of the full PCCA geometry including an illustrative ray-tracing of the primary and secondary fields.

Here,  $\Delta_{PC}^{sec}$  is the phase center of the secondary fields and  $E_{phys}$  is the physical extension of the lens which can be expressed as follows:

$$E_{phys} = E_{eq} - E_{tot} - \Delta_{PC}^{feed} \quad (3.5)$$

where  $E_{tot}$  is the physical extension including the height of the gap and the LT-GaAs:

$$E_{tot} = E_{phys} + h_{gap} + h_{LT-GaAs} \quad (3.6)$$

### 3.1.3. Validity of the PO method using primary far-fields

The PO method's validity depends on the geometry of both the array and the lens. For lenses that are small in terms of the wavelength ( $D_{lens} \lesssim 3\lambda_0$ ), the lens surface can not be assumed locally flat, leading to an inaccurate secondary field. Furthermore, because the far fields are used to represent the feed, the lens surface should be in the far field of the connected array at the base of the lens. To be in the far-field,  $R_{min}$  should satisfy the far field conditions given in Equation 3.7. Here  $D$  is the effective diameter of the feed, which is assumed to be  $D \approx D_{array}$  when considering the full array as the feed. The far-field distance is denoted by  $R_{FF}$ , which indicates the minimum distance from the structure where the radiated field satisfies the far-field conditions:

$$R_{min} > R_{FF} = 10D \quad (3.7a)$$

$$R_{min} > R_{FF} = \frac{2D^2}{\lambda_d} \quad (3.7b)$$

In Figure 3.4, the validity criteria for the PO method are plotted in the case far-fields are used to represent the feed. In the work by Garufo et al, a lens radius of  $R_{lens} = 5$  mm and an equivalent extension length of  $E_{EQ} = 0.3164R_{lens}$  are considered, giving  $R_{min} \approx 5.21$  mm. It is evident from Figure 3.4

that the use of the far-fields in the PO method using the full array primary patterns as described is not valid for frequencies larger than approximately 900 GHz. To address this limitation and to provide the possibility of simulating smaller lens radii, instead of using the far-field of the full array, the use of the embedded element patterns (EEP) in the PO method[23] is introduced in the next section.

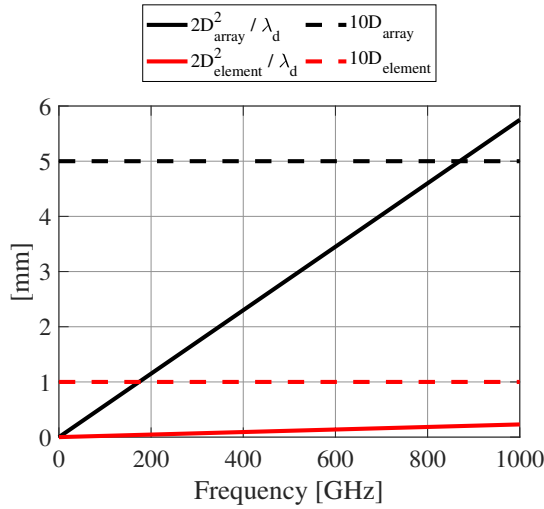


Figure 3.4: Validity criteria for the PO method using primary far-fields. The curves indicate the minimum value that  $R_{min}$  should have in order for the far-field conditions to be satisfied.

### 3.2. PO method using embedded element patterns

The use of the full array primary far-fields in the PO method is limited by the far-field conditions in Equation 3.7. This puts a limit on the lens size and maximum frequency that can be simulated when using the primary far-fields. One can in principle evaluate primary near fields at the inner lens surface using a full-wave solver, and use the PO method as described in Section 3.1.1. However, the evaluation of near fields is more computationally intensive and would require one to recalculate the near fields if another lens extension length is selected. Another option is the use of the embedded element patterns (EEPs) of the individual dipole elements in the array instead of the full array patterns. The use of EEPs is beneficial because the area of a single element is smaller compared to the array, making the far-field distance smaller. This means the lens is in the far-field of a single element for a larger frequency range compared to the full array. The use of the EEP also provides the possibility to simulate the connected array in combination with smaller lenses, which is useful when the dielectric PCCA lenses are optimized for an imaging scenario in Chapter 5.

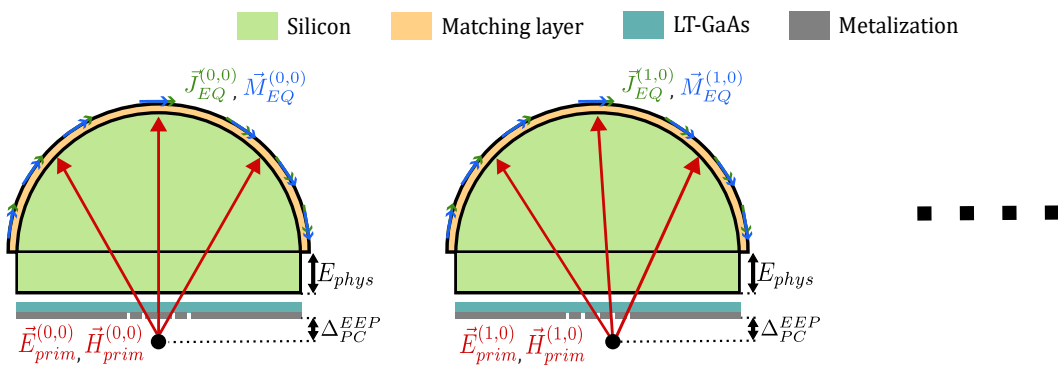


Figure 3.5: Figure illustrating the concept of using the embedded element patterns instead of the full array patterns in the PO method.

The embedded element patterns are obtained using a full-wave solver [19]. More specifically, each

dipole element is excited sequentially assuming all the other elements are closed in a load impedance. Here the load impedances are set to the same impedance as used in Table 2.5 to best approximate a matched load over the considered band. This sequential excitation results in the EEPs for all dipole elements. The magnitude of the center embedded element patterns can be found in Appendix C. In order to obtain the secondary fields, the equivalent current contribution due to each of the individual dipole elements is first found in a similar way as done when using the full array patterns. An important thing to note here is that each EEP is propagated from the phase center of each individual dipole element as shown in Figure 3.5, where the EEPs are denoted by  $(E_{prim}^{(n_x, n_y)}, H_{prim}^{(n_x, n_y)})$ . Here it is assumed that for all elements the phase center displacement is that of the center element  $\Delta_{PC}^{EEP}$ . The phase center of the EEP of the center element for the different air-gap sizes is given in Table 3.1, which is found by minimizing the PEL as defined in Equation 2.3. The figures containing the PEL for the different air-gap sizes can be found in Appendix C.2.

**Table 3.1:** The phase center of the center embedded element pattern in silicon.

$h_{gap}[\mu m]$	$\Delta_{PC}^{EEP}[\mu m]$
0	37
10	60
25	100

The individual current contributions due to each of the EEPs,  $(J_{EQ}^{(n_x, n_y)}, M_{EQ}^{(n_x, n_y)})$ , are summed in order to obtain the total equivalent currents on the lens surface  $(J_{EQ}^{tot}, M_{EQ}^{tot})$  as follows:

$$J_{EQ}^{tot} = \sum_{n_x=-2}^2 \sum_{n_y=-2}^2 J_{EQ}^{(n_x, n_y)} \quad (3.8a)$$

$$M_{EQ}^{tot} = \sum_{n_x=-2}^2 \sum_{n_y=-2}^2 M_{EQ}^{(n_x, n_y)} \quad (3.8b)$$

From the total currents, the secondary fields can be calculated using the Green's function equations listed in Equation 3.4.

### 3.3. Verification of the revised PO method

To verify the results of the revised PO method, a case is studied in which both the PO with primary patterns and the PO with embedded patterns are within their region of validity. This means that for both cases the validity conditions shown in Figure 3.4 are satisfied, and the methods are expected to give the same secondary fields. The geometry used for the verification is defined by the parameters in Table 3.2.

**Table 3.2:** Dimensions of the geometry used to verify the revised PO method

	$R_{lens}[mm]$	$h_{gap}[\mu m]$	$E_{tot}$	$E_{eq}$	$\Delta_{PC}^{sec}[mm]$
Verification geometry	10	0	$0.29R_{lens}$	$0.3032R_{lens}$	29.8

Here, the radius of the lens is taken to be  $R_{lens} = 10$  mm such that the lens is in the far-field with respect to the active patterns and the embedded patterns. The secondary fields evaluated using both the active and embedded patterns at 400 GHz and 700 GHz are shown below:

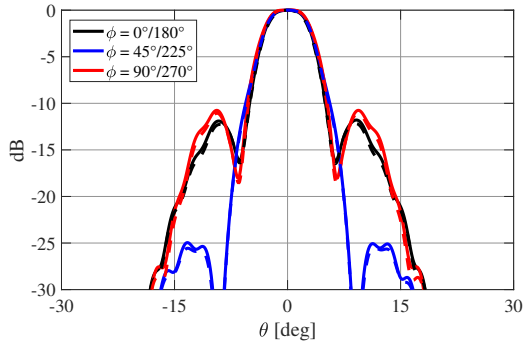


**Figure 3.6:** Secondary field evaluated using the primary patterns (solid) and embedded patterns (dashed) of the verification geometry at  $f = 400$  GHz. Note that only the co-polar components of the field are shown.

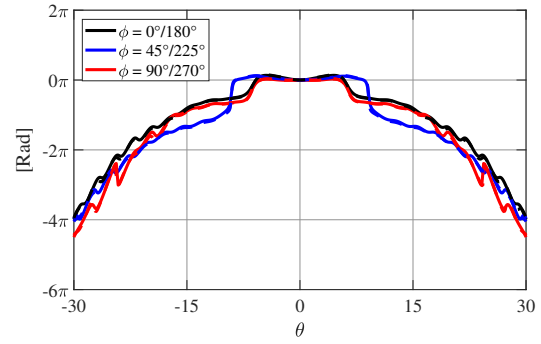


**Figure 3.7:** Phase of the secondary field evaluated using the primary patterns (solid) and embedded patterns (dashed) of the verification geometry at  $f = 400$  GHz. Note that the phase is plotted from the phase center, and only the phase of the co-polar component is shown.

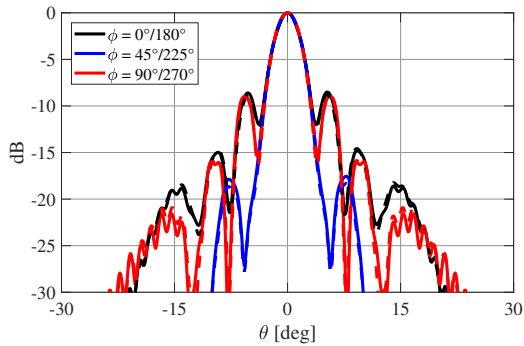


**Figure 3.8:** Secondary field evaluated using the primary patterns (solid) and embedded patterns (dashed) of the verification geometry at  $f = 700$  GHz. Note that only the co-polar components of the field are shown.

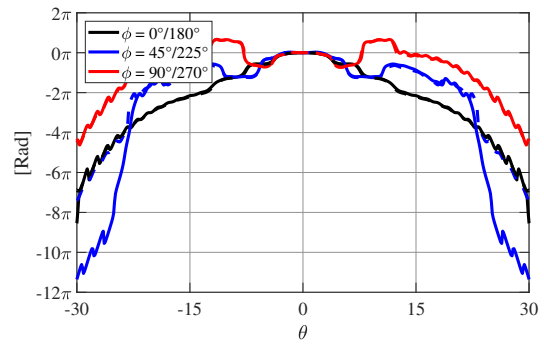


**Figure 3.9:** Phase of the secondary field evaluated using the primary patterns (solid) and embedded patterns (dashed) of the verification geometry at  $f = 700$  GHz. Note that the field has its phase center as its origin, and only the phase of the co-polar component is shown.

As expected, there is an excellent agreement between the two cases. Here small deviations can be attributed to numerical errors. The phase centers of the secondary fields  $\Delta_{PC}^{sec}$  are found by calculating the PEL of the secondary fields and minimizing it over the considered frequency range. Note here that  $\Delta_{PC}^{sec}$  is defined as the distance from the bottom of the physical extension of the lens to the phase center. For illustrative purposes, the magnitude of the magnetic currents  $M_{EQ}^{tot}$  obtained using the revised PO method are shown in Figure 3.10.

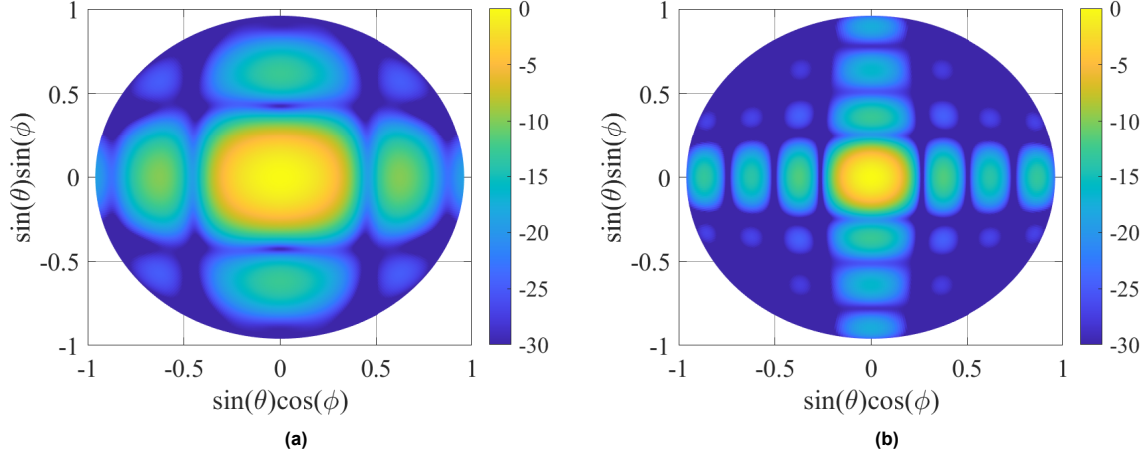


**Figure 3.10:** Magnitude of the magnetic currents  $M_{EQ}^{tot}$  on the lens surface of the verification structure listed in Table 3.2 at (a) 400 GHz and at (b) 700 GHz

### 3.4. Application of the revised PO method to fabricated geometries

Currently two PCCA geometries have been fabricated, one without an air-gap ( $h_{gap} = 0 \mu\text{m}$ ) and one with an air-gap ( $h_{gap} = 25 \mu\text{m}$ ). The dimensions of both geometries are given in Table 3.3.

**Table 3.3:** Dimensions of the fabricated PCCA geometries and phase centers of the secondary fields

Fabricated geometries	$R_{lens}[mm]$	$h_{gap}[\mu m]$	$E_{tot}$	$E_{eq}$	$\Delta_{PC}^{sec}[mm]$
PCCA	5	0	$0.29R_{lens}$	$0.3164R_{lens}$	-3.1
LW PCCA	5	25	$0.3074R_{lens}$	$0.3960R_{lens}$	-11.5

For these two geometries, the secondary fields are evaluated using the PO method in combination with the EEPs, meaning the equivalent currents on the lens surface are evaluated as in Equation 3.8. The magnitude of the secondary fields at 400 GHz, 700 GHz, and 1000 GHz are shown below for the two structures. The amplitude patterns of all considered frequencies are shown in Appendix D. From Figure 3.15 the effect of the grating lobes in the  $h_{gap} = 0 \mu\text{m}$  case is strongly visible.

The phase centers of the secondary fields  $\Delta_{PC}^{sec}$  are found by calculating the PEL of the secondary fields and minimizing it over the considered frequency range. The PEL for the different stratifications is shown in Appendix D.2. The secondary field phase centers associated with the fabricated geometries are listed in Table 3.3. Note here that the negative sign of the phase center means the phase center is located above the plane in which the connected array lies.

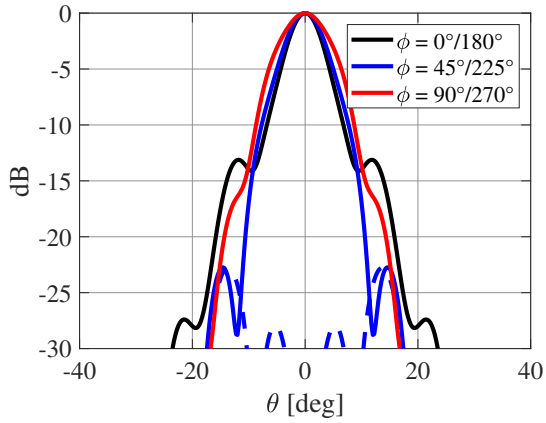


**Figure 3.11:** Secondary field at  $f = 400$  GHz for the fabricated PCCA geometry with  $h_{gap} = 0 \mu\text{m}$

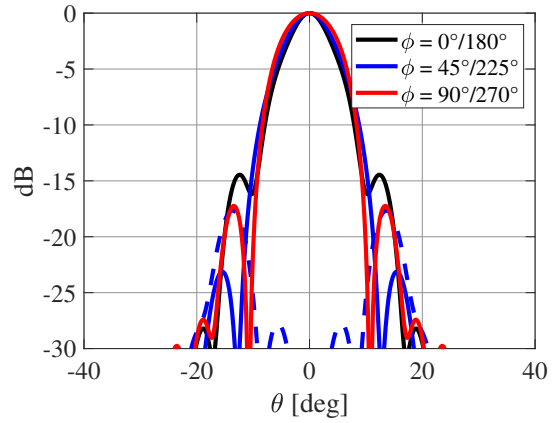


**Figure 3.12:** Secondary field at  $f = 400$  GHz for the fabricated LW PCCA geometry with  $h_{gap} = 25 \mu\text{m}$

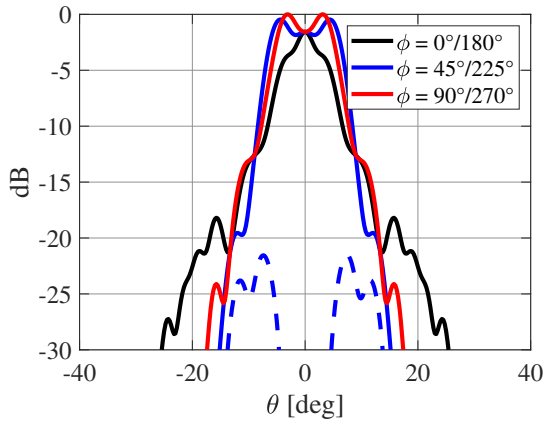


**Figure 3.13:** Secondary field at  $f = 700$  GHz for the fabricated PCCA geometry with  $h_{gap} = 0 \mu\text{m}$

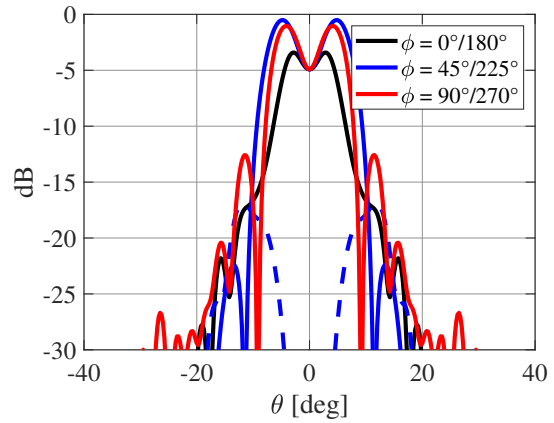


**Figure 3.14:** Secondary field at  $f = 700$  GHz for the fabricated LW PCCA geometry with  $h_{gap} = 25 \mu\text{m}$

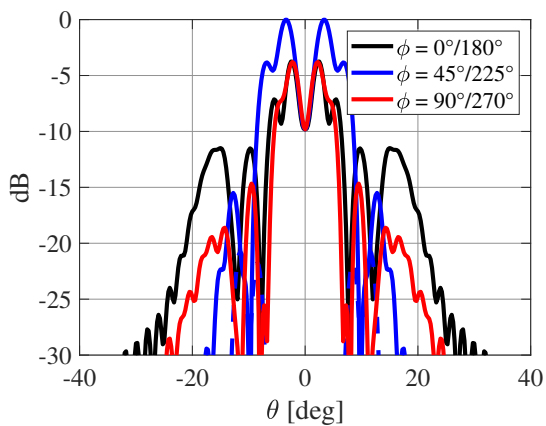


**Figure 3.15:** Secondary field at  $f = 1000$  GHz for the fabricated PCCA geometry with  $h_{gap} = 0 \mu\text{m}$

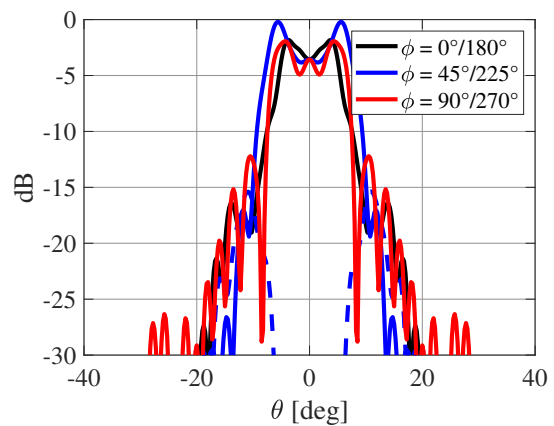


**Figure 3.16:** Secondary field at  $f = 1000$  GHz for the fabricated LW PCCA geometry with  $h_{gap} = 25 \mu\text{m}$

### 3.4.1. Lens efficiency

Part of the power generated in the photoconductive gap is lost due to different mechanisms. In Equation 2.4, the front-to-back efficiency  $\eta_{f2b}$  is introduced to quantify the losses due to the part of the radiation that goes to the backside of the array. The introduction of the dielectric lens causes two additional loss factors: reflection losses and spillover losses. The reflection losses occur due to the change in dielectric permittivity when going from the silicon medium to the matching layer, and when going from the matching layer to air. The reflection losses are quantified by the reflection efficiency  $\eta_{ref}^{PCA}$  of the PCA. The part of the field that does not hit the lens surface is considered lost and is quantified by the spillover efficiency of the PCA  $\eta_{SO}^{PCA}$ .

A single efficiency is introduced capturing the front-to-back losses, the reflection losses, and the spillover losses, called the PCA lens efficiency  $\eta_l^{PCA}$ :

$$\begin{aligned}\eta_l^{PCA}(f) &= \eta_{f2b}(f) \cdot \eta_{ref}^{PCA}(f) \cdot \eta_{SO}^{PCA}(f) \\ &= \frac{P_{sec}(f)}{P_{prim}^{tot}(f)}\end{aligned}\quad (3.9)$$

Here the power in the secondary fields is denoted as  $P_{sec}(f)$ . The PCA lens efficiency is shown for the fabricated arrays in Figure 3.17.

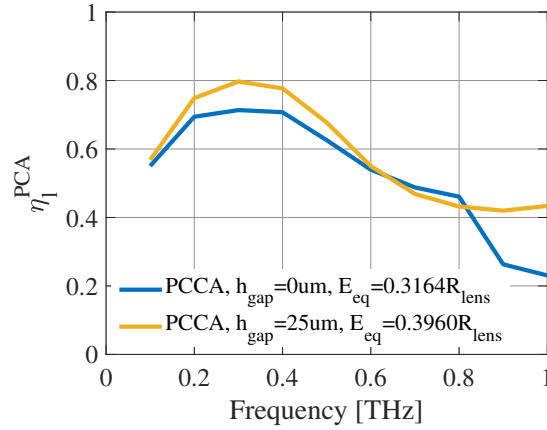


Figure 3.17: PCA lens efficiency  $\eta_l^{PCA}$  for the fabricated array geometries listed in Table 3.3.

Note that directly comparing the lens efficiencies of the fabricated geometries is not fair because the equivalent lens extensions  $E_{eq}$  in the geometries are not equal. Generally, if the equivalent extension length becomes larger, the lens efficiency decreases due to increasing spillover and reflection losses on the dielectric lens. The increase in reflection losses is because the main beam of the primary pattern illuminates an increasingly larger portion of the lens as the equivalent extension increases. A fair comparison between two cases with different  $h_{gap}$  but with the same equivalent extension is discussed in Chapter 5.

### 3.4.2. Spectra and radiated power

Using the PCA lens efficiency  $\eta_l^{PCA}$  and the spectra of the energy generated by the PC source, the spectra of the fields radiated into air by the full PCCA structure are found (secondary spectra). The secondary spectra shown in Figure 3.18 are found as:

$$E_{s,array}^{air}(f) = \eta_l^{PCA}(f) \cdot E_{s,array}(f) \quad (3.10)$$

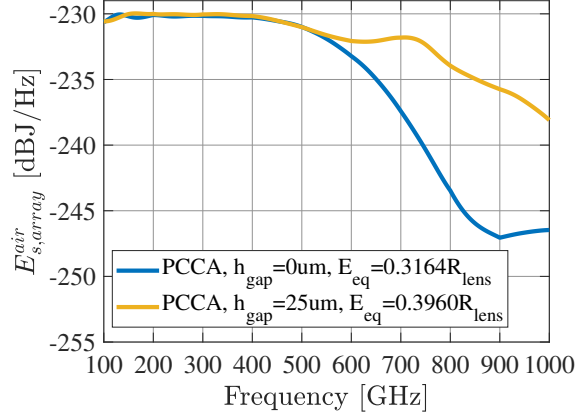


**Figure 3.18:** Energy spectral densities of the secondary field for the fabricated geometries listed in Table 3.3. For the evaluation of the Norton circuit, following variable parameters are used  $\eta_{SO,laser}^{ML} = \eta_{SO,laser}^{ML,Ideal} = 0.580$  and  $\eta_{SO,laser}^{Gap} = \eta_{SO,laser}^{Gap,Ideal} = 0.537$ ,  $V_b = 80$  V,  $\tilde{P}_L = 178$  mW.

To evaluate  $E_{s,array}$  in Equation 3.10, the same parameters in the Norton circuit are used for the evaluation of the primary spectrum in Figure 2.19. The associated radiated power  $P_{rad}^{air}$  can then be found as:

$$P_{rad}^{air} = \frac{2}{T_L} \int_0^{\infty} E_{s,array}^{air}(f) df \quad (3.11)$$

where for the evaluation of  $P_{rad}^{air}$  a frequency band is considered from 100 GHz to 1000 GHz. Using Equation 3.11, the radiated power into air by the PCCA structures is evaluated and listed in Table 3.4. Evidently, the structure with an air-gap radiates more power which can be attributed to the higher PCA lens efficiency at the lower end of the spectrum, and the fact that the cut-off phenomena are pushed to higher frequencies due to the presence of the air-gap.

**Table 3.4:** Simulated radiated power into air of the full fabricated PCCA structures, associated to the spectra in Figure 3.18

$h_{gap}[\mu m]$	$P_{rad}^{air}[mW]$
0	0.78
25	1.00

### 3.5. Conclusions

This chapter introduces a PO method that uses the embedded element patterns instead of the full primary patterns. The use of embedded element patterns is beneficial, as it is generally valid for a larger frequency band compared to the use of primary patterns in the PO method. Using the embedded element patterns gives almost identical results compared to using primary patterns in the PO method when both are in their frequency region of validity. The secondary fields of the fabricated PCCA geometries are evaluated, and from these, the PCA lens efficiencies are calculated. However, the fabricated geometries are hard to compare as their equivalent lens extension lengths  $E_{eq}$  are quite different. Also, the lens extension lengths of the fabricated geometries are currently not optimized for a particular use case such as imaging. Still, for both cases, a relatively flat spectrum is obtained, and the positive effect of the addition of the air gap on the secondary field shape, lens efficiency, and impedance properties is visible as an increase in the bandwidth.

# Array model comparison to experimental results

In Chapter 2 the spectra and associated power generated by the photoconductive gaps of a PCCA under pulsed laser excitation are simulated employing a time-domain Norton circuit. In Chapter 3 the effect of the dielectric lens on the spectrum and radiated power is quantified, and the radiation patterns of the fields after the lens are found. There are two PCCAs that have been fabricated and measured in the THz Laser Lab at Delft University of Technology. The experiment setup is shown in Figure 4.1. In this chapter, this power measurement setup is modeled and simulations are compared to measurements. The experiment is performed using the Tera K15 THz-TDS system by Menlo Systems, where the transmitting antenna is replaced by the PCCA under test, and the receiving antenna is replaced by a horn antenna which is connected to a circular waveguide. The waveguide is connected to a PM5 power meter, which measures the absorbed power.

The transmitting PCCA antenna is placed such that its phase center is aligned with the focus of the first plano-convex lens in blue. The first plano-convex lens collimates the field between the two lenses. The field arriving at the second plano-convex lens is focussed into the horn antenna and subsequently absorbed by the power meter in the waveguide connected to the horn.

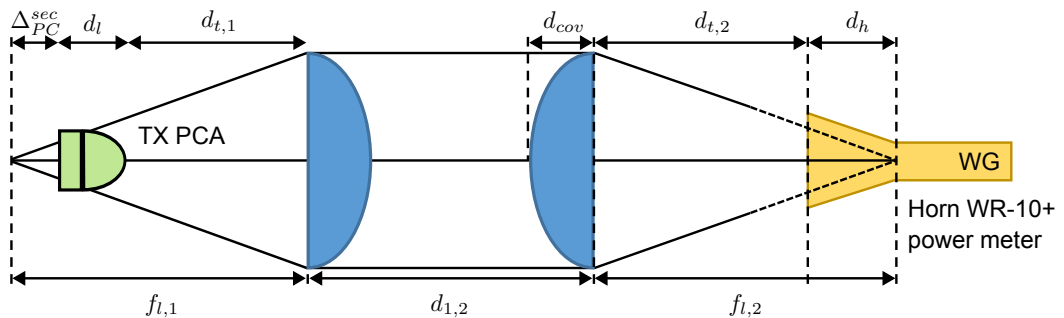


**Figure 4.1:** Schematic overview of the power measurement setup used to validate the array model.

While doing the experiment, some dimensions are tuned by hand in order to obtain the maximum possible received power in the absorber. The dimensions used during the measurement are given in Table 4.1.

**Table 4.1:** Dimensions used in the power measurement experiment done in the lab.

Fabricated geometries	$f_{l,1}[mm]$	$d_{t,1}[mm]$	$d_l$	$\Delta_{PC}^{sec}[mm]$	$d_{cov}[mm]$	$d_{1,2}[mm]$	$f_{l,2}[mm]$	$d_{t,2}[mm]$	$d_h[mm]$
PCCA ( $h_{gap} = 0 \mu m$ )	46.85	43.5	$1.29R_{lens}$	-3.1	8.5	56.5	44.6	14.5	30.1
LW PCCA ( $h_{gap} = 25 \mu m$ )	56.04	61	$1.3074R_{lens}$	-11.5	8.5	43.5	43.1	13	30.1

In this chapter, first the setup in Figure 4.1 is modeled and simulated to quantify the effect of the QO path

on the received power by the horn. Then, the comparison between simulations and measurements is shown and discussed.

### 4.1. Modeling and simulation of the QO channel

Several losses along the QO path shown in Figure 4.1 can be identified. The losses due to the front-to-back ratio and spillover and reflections on the dielectric lens are quantified by the lens efficiency  $\eta_l^{PCA}$  as defined in Equation 3.9. The losses associated with the rest of the QO path from the PCCA lens to the power meter are quantified using the commercial solver GRASP [24]. The secondary fields radiated by the lens antenna are imported as a tabulated source into GRASP. The secondary fields are then propagated to the horn using the GO/PO solver of GRASP. The setup in GRASP, including a ray-tracing, is shown in Figure 4.2.

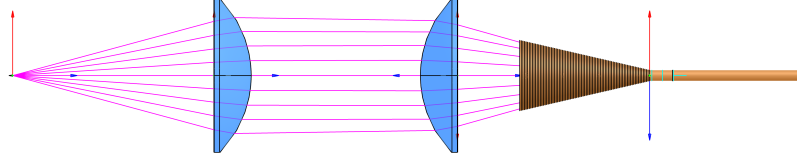


Figure 4.2: Power measurement setup modeled in GRASP.

The losses in the QO path from the PCCA lens to the horn include the reflection and spillover losses on the plano-convex lenses and the spillover on the horn antenna. The total effect of the QO path on the detected power can be quantified by defining an efficiency  $\eta_{QO}^{setup}$ , which is defined as follows:

$$\eta_{QO}^{setup} = \frac{P_{WG}(f)}{P_{sec}(f)} \quad (4.1)$$

where  $P_{WG}(f)$  is the power captured in the waveguide and  $P_{sec}(f)$  is the power in the secondary fields of the PCCA. Several simulation outputs are given by GRASP, namely the power incident on the second plano-convex lens and the EM fields on a cross-sectional circular grid in the waveguide connected to the horn antenna ( $\vec{E}_{WG}, \vec{H}_{WG}$ ). The power in the waveguide  $P_{WG}$  is then found using the waveguide fields by integrating the Poynting vector  $\vec{S}_{x,y,z}$  inside the waveguide:

$$P_{WG} = \int_0^{R_{WG}} \int_0^{2\pi} \vec{S}_{x,y,z} \cdot \hat{z} \rho d\rho d\phi \quad (4.2)$$

Here  $\hat{z}$  is the normal unit vector to the cross-section in the waveguide, and  $R_{WG}$  is the radius of the waveguide. The plano-convex lenses in GRASP are modeled as lossless lenses. However, ohmic losses occur in the lenses and are quantified by  $\eta_{menlo}^{loss}$ , which is shown in Figure 4.3. The total quasi-optical efficiency of the system  $\eta_{QO}$  is then defined as:

$$\eta_{QO}(f) = \eta_l^{PCA}(f) \cdot \eta_{QO}^{setup}(f) \cdot \eta_{menlo}^{loss}(f) \quad (4.3)$$

The total quasi-optical efficiency for both structures is shown in Figure 4.4.

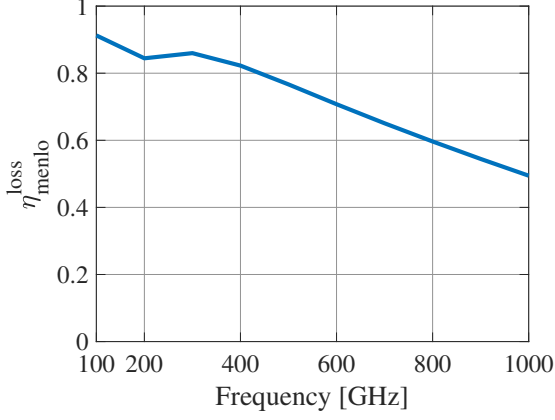


**Figure 4.3:** Ohmic losses of the plano-convex lenses included in the Tera K15 system by Menlo Systems

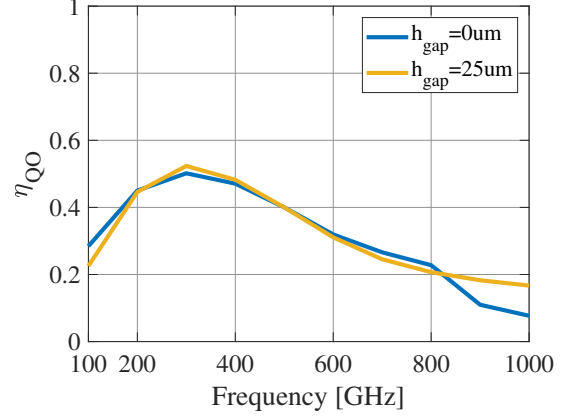


**Figure 4.4:** Quasi-optical efficiency of the full setup as defined in Equation 4.3 for the two PCCA geometries.

## 4.2. Predicted and measured detected power

In the experiment, a power measurement of the absorbed power by the PM5 is done for various conditions. The laser profile was measured in two orthogonal planes using the knife-edge technique [25]. The Full-Width Half Maximum (FWHM) is used as the laser diameter which was measured to be  $D_{laser} = 510 \mu\text{m}$ , and is thus slightly larger than that of the ideal one. This leads to a spillover efficiency on the microlens array of  $\eta_{SO,laser}^{ML} = 0.566$ . The values of the remaining (fixed) parameters are those listed in Table 2.3.

To get the detected power  $P_d$  predicted from the model, the spectrum is integrated together with the QO efficiency defined by Equation 4.3 as shown below:

$$P_d = \frac{2}{T_L} \int_0^{\infty} E_{s,array}(f) \cdot \eta_{QO}(f) df \quad (4.4)$$

The effect of varying two different parameters is studied. First,  $P_d$  is plotted against the average laser power  $\tilde{P}_L$  for several values of  $V_b$ . The simulated and measured detected power are shown in Figure 4.5.

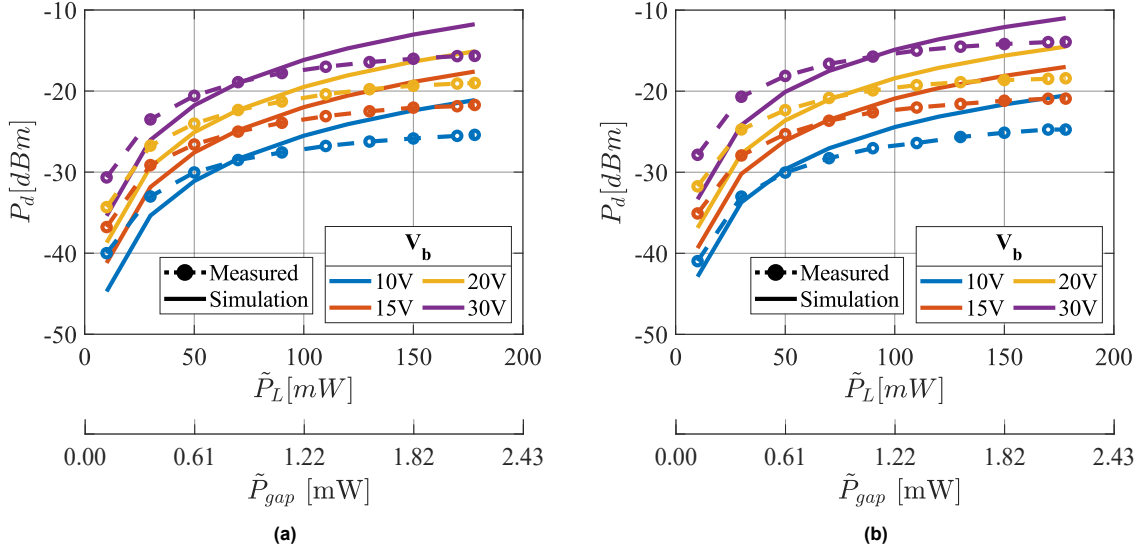


**Figure 4.5:** The simulated and measured detected power  $P_d$  plotted against the average laser power  $\tilde{P}_L$ , for the fabricated PCCA with (a)  $h_{gap} = 0 \mu\text{m}$  and (b)  $h_{gap} = 25 \mu\text{m}$ . Here  $\eta_{SO,laser}^{ML} = 0.566$ ,  $\eta_{SO,laser}^{Gap} = 0.537$  and the other parameters are as in Table 2.3.

The results in Figure 4.5 show a decent match between measurements and simulations. However, the measured curves saturate faster for increasing laser power than expected from the simulation. The deviation from the model is likely explained by the approximation made on the array impedance, as the power tends to saturate more quickly for increasing laser powers as the assumed array resistance  $r_a$  increases [9]. In the model, it is assumed that the element impedances are those of a continuously excited array, while in reality, the PC gaps are only conductive for a short time. The time duration in which the gap is conductive is in the order of the propagation time between two neighboring elements. Due to this highly time-dependent behavior of the element impedances, the mutual-coupling effects between elements are not modeled correctly with the current formulation. A schematic visualization of this effect is shown in Figure 4.6.

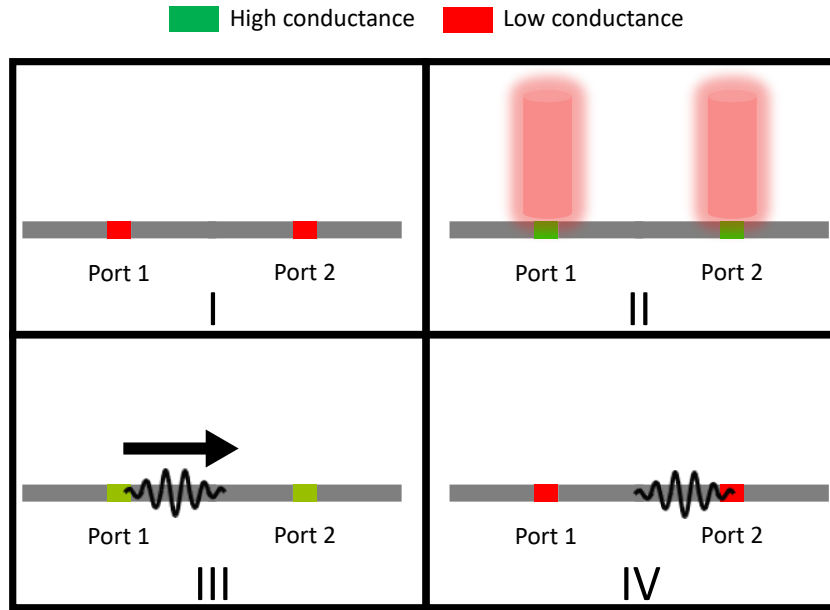


**Figure 4.6:** (I) Both ports are inactive, the PC gaps are not conductive. (II) A laser pulse is incident on both PC gaps, and the conductivity on the gaps becomes finite. (III) Due to the applied bias voltage, a current is induced in each of the PC gaps which serve as a feed to the dipoles in the array. This in turn causes the dipoles to radiate. Only the radiation from the dipole connected to Port 1 is considered in this figure for illustration. (IV) By the time the radiated pulse arrives at the second port, the conductance of the second PC gap is already near zero, meaning the element impedance of the second dipole approaches that of an open circuit.

Also, when evaluating  $i_{rad}(t)$  which necessary to find  $E_{s,array}$ , the array impedance is approximated as a frequency-independent real radiation resistance (Equation 2.5). Apart from the fact that the array impedance is not accurately known due to the effect shown in Figure 4.6, ignoring the reactive part of the array impedance and the frequency dependence of the real part of the impedance when calculating  $i_{rad}(t)$  introduces errors. To find the main source of error, first a more accurate description of the array impedance should be developed.

Another case is considered where the bias voltage on each element  $V_b$  is varied under a constant maximum laser power of  $P_L = 178$  mW. The predicted detected power is shown together with the measured powers for varying  $V_b$  in Figure 4.7.

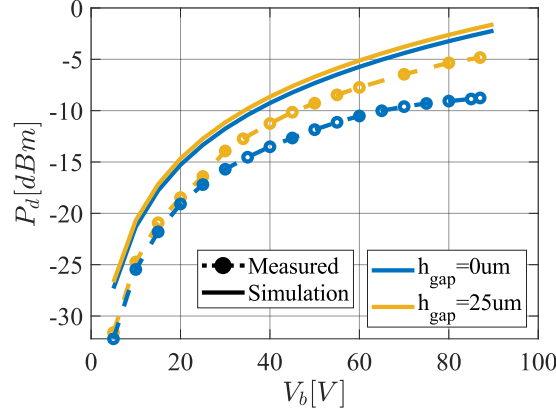


**Figure 4.7:** The simulated and measured detected power plotted against  $V_b$  for the fabricated PCCA with. Here the laser power is kept constant at  $\tilde{P}_L = 178$  mW,  $\eta_{SO,laser}^{ML} = 0.566$ ,  $\eta_{SO,laser}^{Gap} = 0.537$  and the other parameters are as in Table 2.3.

From Figure 4.7, several observations can be made. The first observation is that an offset is present between the measured and simulated curves. This offset is due to the fact that for  $P_L = 178$  mW the devices operate in the saturation region with respect to the laser power, which is not modeled well as previously explained. For the  $h_{gap} = 0$   $\mu\text{m}$  structure, another saturation effect for the measured curve can be observed for increasing bias voltage. This saturation for increasing bias voltage is not observed for the  $h_{gap} = 25$   $\mu\text{m}$  case, where the measured curve has the same shape as that of the simulated one. The exact reason why the  $h_{gap} = 0$   $\mu\text{m}$  saturates, and the  $h_{gap} = 25$   $\mu\text{m}$  does not saturate is currently still being investigated.

### 4.3. Measured spectra

Spectral measurements have been done of the fabricated PCCA antennas in the TUDelft Laser Lab [26]. The measurements are carried out with the Tera K15 receiver and a different QO setup than the one shown in Figure 4.1. The measured spectra are shown in Figure 4.8, where both PCCAs are measured under the same conditions. While neither the QO setup nor the signature of the receiving antenna was modeled in this work, comparing the measured spectra of the PCCA with  $h_{gap} = 0$   $\mu\text{m}$  and  $h_{gap} = 25$   $\mu\text{m}$  shows that the addition of an air-gap indeed has a positive effect on the spectrum. From Figure 4.8 one can see that the roll-off of the spectrum due to destructive mutual coupling and the grating lobes is not present for the  $h_{gap} = 25$   $\mu\text{m}$  PCCA, while it is visible for the  $h_{gap} = 0$   $\mu\text{m}$  PCCA.

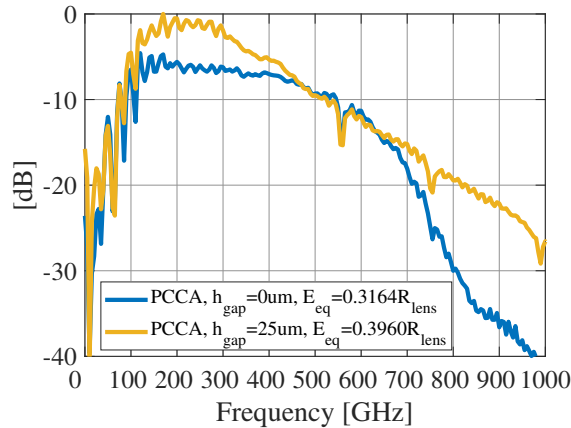


**Figure 4.8:** Spectra of the fabricated PCCA geometries measured using the Tera K15 receiver. Here,  $\eta_{SO,laser}^{ML} = \eta_{SO,laser}^{ML, Ideal} = 0.580$  and  $\eta_{SO,laser}^{Gap} = \eta_{SO,laser}^{Gap, Ideal} = 0.537$ ,  $V_b = 30$  V,  $\tilde{P}_L = 178$  mW. Note that both spectra are normalized to the maximum value of the spectrum of the PCCA with  $h_{gap} = 25$   $\mu\text{m}$ .

## 4.4. Conclusions

A power-measurement experiment is used to check whether the behavior of the PCCA structures in terms of radiated power can be successfully predicted. The effect of the QO path of the measurement setup is simulated in GRASP. A decent match is present between the predicted power at the receiver and the measured power. When the PCCAs are in saturation with respect to the applied laser power, the model starts to deviate from the measurements. This deviation can most likely be attributed to assumptions made on the impedance of the array, from which the approximated radiation resistance  $r_a$  is estimated. The accuracy of the model is expected to improve when a more accurate description of the array impedance is developed and used in the current context. Furthermore, a saturation effect with respect to the bias voltage is observed in the measurements of the  $h_{gap} = 0 \mu\text{m}$  PCCA, which is not predicted by the model. Lastly, a spectral measurement of the PCCAs confirms the positive effect of the added leaky wave cavity on the bandwidth.

## **Part II**

# **Imaging setup design**

## PCCA lens optimization

In Part I of this work, two fabricated PCCA geometries are analyzed and discussed. These fabricated geometries are by themselves not suitable for mm-resolution imaging, due to the limited resolution that is obtained with a dielectric lens of  $R_{lens} = 5$  mm. To effectively use the fabricated PCCA geometries for imaging, the PCCA can be coupled to a larger QO component, such as a reflector or a focusing lens, to focus the field onto a small spot. Because of this, the PCCA lens should be designed such that the secondary field effectively illuminates the focusing component. In this chapter, first, the two classical hemispherical lens extensions are discussed. Then, the extension of the hemispherical lens is chosen such that the aperture efficiency is maximized for a general QO component.

### 5.1. Hemispherical lens extensions

Hemispherical lenses are a widely used type of integrated lenses as they are easy to fabricate because of their simple shape. Two types of hemispherical lens extensions are commonly used: the hyper-hemispherical extension and the elliptical extension. The hyper-hemispherical extension length is  $E_{eq}/R_{lens} = 1/\sqrt{\epsilon_r} = 0.29$  [27], and the elliptical extension length is around  $E_{eq}/R_{lens} = 0.38 - 0.39$  for a silicon lens [28]. A schematic representation of both cases is shown in Figure 5.1.

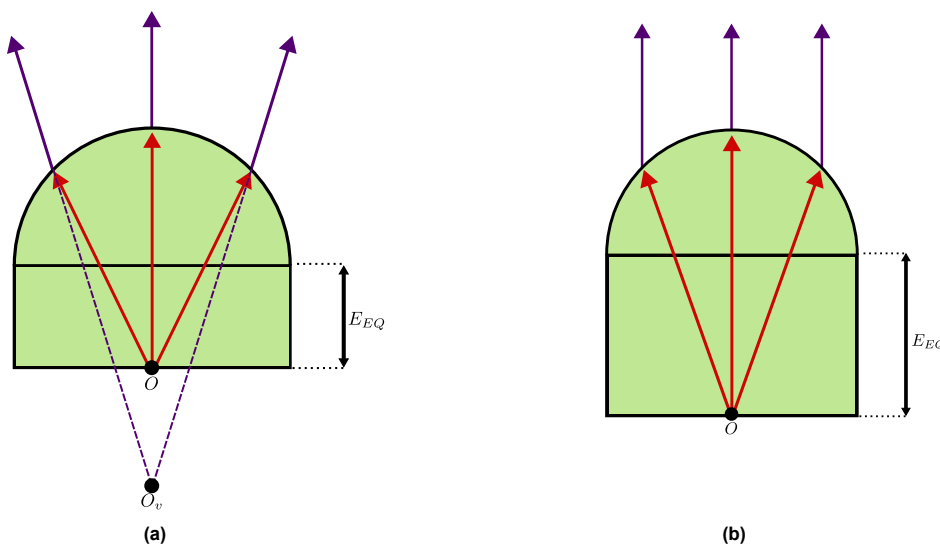


**Figure 5.1:** Schematic drawing of extended hemispherical lenses with (a) a hyper-hemispherical extension (b) an elliptical extension.

The hyper-hemispherical lens has a virtual focus  $O_v$  behind the lens which is frequency independent, gives a radiated field that is not collimated, and bends the rays of the feed towards its axis. Due to the non-collimated rays of the radiated field, the directivity of this type of lens does not scale with the

lens size but depends mainly on the radiation pattern of the feed [29]. The elliptically extended lens approximates a true elliptical lens, which produces collimated rays for the transmitted field.

## 5.2. PCCA coupled to a parabolic reflector

To get an idea of what extension to use for the hemispherical lens, we compare the coupling of a PCCA with both extensions to a canonical parabolic reflector. The performance of the feed in this work is measured by considering the aperture efficiency on the reflector, which quantifies the loss in gain of the reflected field due to a non-perfect feed. Note that here the parabolic reflector does not focus the field and will not be used in an imaging setup. The parabolic reflector geometry is considered as it is a standard canonical geometry used to quantify the performance of a feed in terms of aperture efficiency. Furthermore, the geometry does not depend on specific scenario parameters, but only on the f-number of the reflector. One can expect similar values for the aperture efficiency when the parabolic reflector is replaced with a focusing component like an elliptical reflector or focusing lens, due to their similar shape. A schematic overview of a general parabolic reflector fed by a PCCA is shown in Figure 5.2.

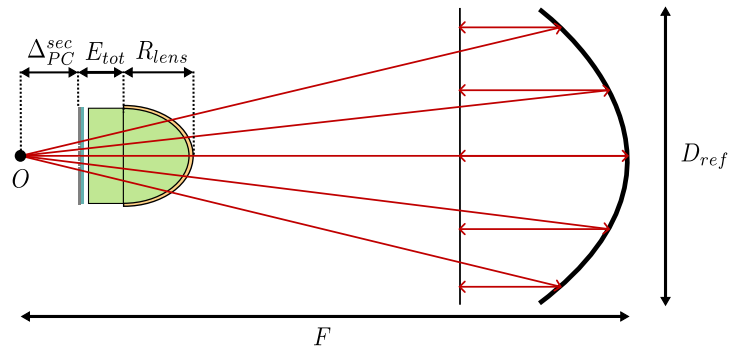


**Figure 5.2:** Schematic overview of a parabolic reflector illuminated by an extended hemispherical lens where the feed is a PCCA.

### 5.2.1. Aperture efficiency on a parabolic reflector

Close to the reflector, the reflected field can be evaluated analytically using a Geometrical Optics (GO) approach [30]. In this section, the field in a circular region centered at the focus of the reflector (equivalent aperture) is evaluated. Here it is assumed that the reflector is in the far field with respect to the PCA feed. Using the fields on the equivalent aperture, the aperture efficiency is calculated. The geometry including the coordinate systems used is shown in Figure 5.3. The focus is denoted by  $O$ , the coordinate system of the feed is  $(\theta', \phi', r')$ ,  $Q$  is a point on the reflector,  $P$  is a point on the equivalent aperture,  $\rho$  is the radial component in the coordinate system of the equivalent aperture,  $D_{ref}$  is the diameter of the reflector and  $F$  the focal distance. Note here that the phase center of the secondary fields is aligned with the focus of the reflector as shown in Figure 5.2.

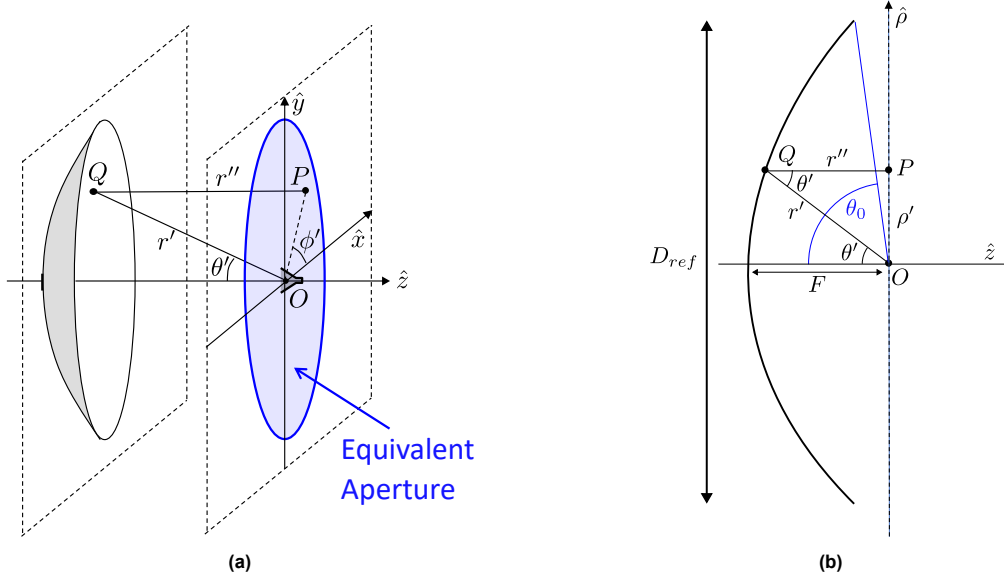


**Figure 5.3:** (a) Schematic representation of a parabolic reflector geometry including the coordinate system of the feed. (b) Cross-sectional view of the reflector including the coordinate system of the equivalent aperture. [31]

Following the derivation in [30], the components of the electric field distribution on the equivalent aperture  $\vec{E}_a$  are written as follows:

$$\vec{E}_{a,\rho}(\rho', \phi') = -\vec{f}_{pattern,\theta'} \left( \theta' = 2 \tan^{-1} \left( \frac{\rho'}{2F} \right), \phi' \right) \frac{4F}{4F^2 + (\rho')^2} e^{-2jkF} \quad (5.1a)$$

$$\vec{E}_{a,\phi}(\rho', \phi') = -\vec{f}_{pattern,\phi'} \left( \theta' = 2 \tan^{-1} \left( \frac{\rho'}{2F} \right), \phi' \right) \frac{4F}{4F^2 + (\rho')^2} e^{-2jkF} \quad (5.1b)$$

where  $\vec{f}_{pattern} = \vec{E}_{sec} \cdot R_{sec} \cdot e^{jkR_{sec}}$  is the secondary field back-propagated to its origin, with  $R_{sec}$  the radius at which the secondary fields are evaluated. Using a PO approach, one could calculate the far fields radiated by the reflector using aperture fields. However, for the evaluation of the aperture efficiency, only the field on the equivalent aperture is necessary.

The aperture efficiency is defined as the product of the taper efficiency  $\eta_{tap}$  and the spillover efficiency  $\eta_{SO}$ , as  $\eta_{ap} = \eta_{SO} \eta_{tap}$ . The taper efficiency quantifies the loss of directivity of the reflected far field due to the tapering of the field on the equivalent aperture. The taper efficiency can be expressed as follows:

$$\eta_{tap} = \frac{4}{\pi D_{ref}^2} \frac{\left| \int_0^{2\pi} \int_0^\pi E_{a,co}(\rho, \phi) \rho d\rho d\phi \right|^2}{\int_0^{2\pi} \int_0^\pi |E_{a,co}(\rho, \phi)|^2 \rho d\rho d\phi} \quad (5.2)$$

where  $E_{a,co}$  is the co-polar component of the field on the equivalent aperture. The spillover efficiency quantifies the spillover of the secondary fields on the reflector. The spillover is expressed as follows:

$$\eta_{so} = \frac{\int_0^{2\pi} \int_0^{\theta_0} |\vec{E}_{sec}(\theta, \phi)|^2 \sin(\theta) d\theta d\phi}{\int_0^{2\pi} \int_0^\pi |\vec{E}_{sec}(\theta, \phi)|^2 \sin(\theta) d\theta d\phi} \quad (5.3)$$

where  $\theta_0$  is the subtended half-angle, which is related to the f-number  $f_{\#} = \frac{F}{D_{ref}}$  of the reflector as  $\theta_0 = 2 \tan^{-1} \left( \frac{f_{\#}}{4} \right)$ .

### 5.2.2. Optimizing the aperture efficiency on a parabolic reflector

To choose a lens extension suitable for illumination of a QO focussing component, the aperture efficiency is optimized on a parabolic reflector. The dimensions of the considered PCCAs with both

hyper-hemispherical and elliptical extensions are listed in Table 5.1. First, the aperture efficiency is evaluated at the central frequency of 500 GHz while varying the f-number to get an indication of a suitable f-number. The resulting aperture efficiency at  $f = 500$  GHz for the considered structures is shown in Figure 5.4. The secondary fields used to evaluate the aperture efficiency of the PCCAs are found using the PO procedure described in Chapter 3.

**Table 5.1:** Considered geometries for the optimization of the aperture efficiency on a parabolic reflector.

Geometry	$E_{virt}$	$h_{gap}$ [μm]	$R_{lens}$ [mm]	$\Delta_{PC}^{sec}$ [mm]	$f\#$
PCCA	$0.29R_{lens}$	0	5	-3.8	3
PCCA	$0.38R_{lens}$	0	5	-8.5	3.4
LW PCCA	$0.29R_{lens}$	10	5	-5	3
LW PCCA	$0.38R_{lens}$	10	5	-10.3	3.4

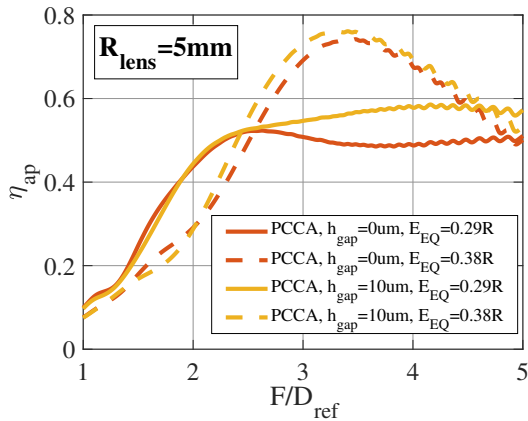


**Figure 5.4:** Aperture efficiency on a parabolic reflector for the structures considered in Table 5.1 at the central frequency of  $f = 500$  GHz for a varying f-number.

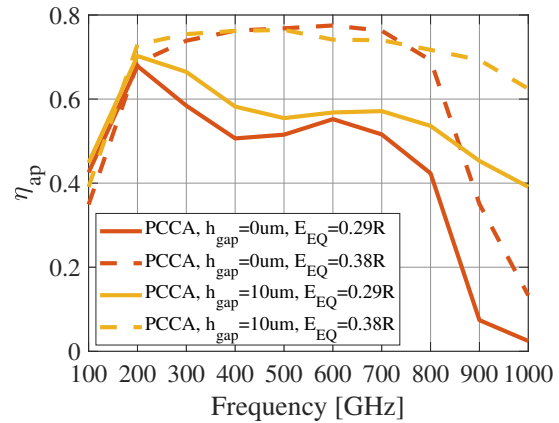


**Figure 5.5:** Aperture efficiency on a parabolic reflector vs frequency for the structures considered in Table 5.1

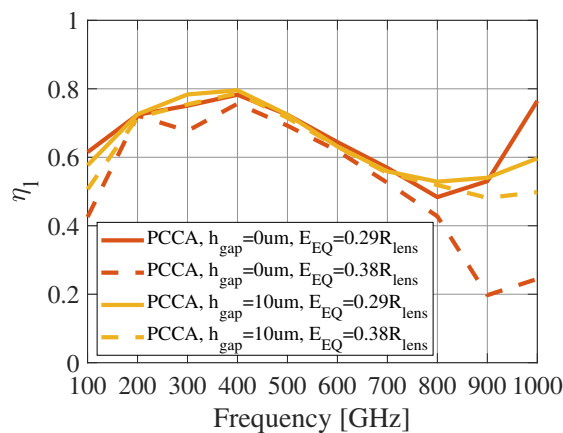


**Figure 5.6:** Lens efficiencies for the geometries listed in Table 5.1.

Using Figure 5.4 as a reference for the f-numbers to be used, the f-numbers are found by optimizing  $\eta_{ap}$  over the whole considered frequency band. The resulting optimized f-numbers for the different structures are listed in Table 5.1, and the corresponding aperture efficiencies are shown in Figure 5.5.

From Figure 5.5 it is evident that the PCCAs with the elliptically extended lenses provide a higher aperture efficiency over the considered frequency band compared to the hyper-hemispherically extended lenses.

For the hyper-hemispherical extension, the directivity of the secondary field is mostly dependent on the directivity of the feed. Because the primary fields become increasingly directive with frequency, the directivity of the secondary fields of the hyper-hemispherically extended PCCA also increases with frequency. The fact that the beamwidth strongly varies with frequency makes efficient illumination of the QO component over a broad frequency band impossible.

For the elliptically extended PCCAs, the directivity of the secondary field is dependent on both frequency and the feed pattern. As the frequency increases and the directivity of the primary field with it, a smaller portion of the PCCA lens is illuminated by the feed. The size of the illuminated area in terms of the wavelength however stays approximately the same due to the decreasing wavelength. This causes the secondary fields to have a main beamwidth that stays quite constant over the considered frequency band, which is beneficial when illuminating a QO component. This is also visible in the aperture efficiencies in Figure 5.5. Another benefit of the elliptically extended PCCAs is that the secondary fields are quite flat over the main beam and have limited side lobes, which allows for a high aperture efficiency. Therefore the elliptically extended PCCAs are superior compared to the hyper-hemispherically extended PCCAs when illuminating the focusing component.

The lens efficiencies for the geometries of Table 5.1 are shown in Figure 5.6. Generally, the reflection and spillover losses are slightly higher for the elliptically extended lenses. This is due to the larger truncation angle associated with the larger extension length of the elliptical extension compared to the hemispherical extension, and also due to the fact that the angle with the normal vector of the lens surface is larger for most rays.

### 5.2.3. Reducing the f-number

For the elliptically extended PCCAs with- and without air-gap, the f-numbers were found to be  $f_{\#} = 3.4$ . A lower f-number is beneficial, as it makes the required distance between the PCCA and the focusing component smaller which allows for a more compact imaging setup. The f-number can be reduced by changing the PCCA lens radius  $R_{lens}$ . To reduce the f-number, a smaller PCCA lens radius of  $R_{lens} = 2.5$  mm is considered, which makes the secondary field less directive. Halving the PCCA lens radius has a negligible effect on the aperture efficiency and lens efficiency, but approximately halves the f-number, giving an optimal f-number of  $f_{\#} = 1.65$ . The final geometries that are considered most suitable for imaging are listed in Table 5.2, and are further analyzed in Chapter 6. Here, as a reference, the geometry and results for a fabricated state-of-the-art leaky wave bow-tie PCA are shown as well. The result for the LW BT is given in a frequency range from 150 GHz – 1000 GHz, as beneath 150 GHz, the PO analysis was found to be inaccurate compared to full-wave simulations. The aperture efficiency evaluated using GRASP for the geometries listed in Table 5.2 is shown in Figure 5.9, and the lens efficiency is shown in Figure 5.10. The secondary field amplitudes of the PCCAs are given in Appendix E, and the field amplitudes of the LW-BT are shown in Appendix F. Note here that at  $f = 100$  GHz, the lens diameter is  $D_{lens} \approx 1.67\lambda_0$ , might not be accurately simulated by the PO as explained in Section 3.1.3. The simulations at 100 GHz obtained using the PO are included anyway as a reference.

**Table 5.2:** Final PCCA geometries that are considered most optimal for imaging and the state-of-the-art LW BT as a reference.

Geometry	$E_{virt}$	$h_{gap}$ [μm]	$R_{lens}$ [mm]	$\Delta_{PC}^{sec}$ [mm]	$f_{\#}$
PCCA	$0.38R_{lens}$	0	2.5	-4.2	1.65
LW PCCA	$0.38R_{lens}$	10	2.5	-4.2	1.65
LW BT	$0.312R_{lens}$	10	5	18.5	2.7

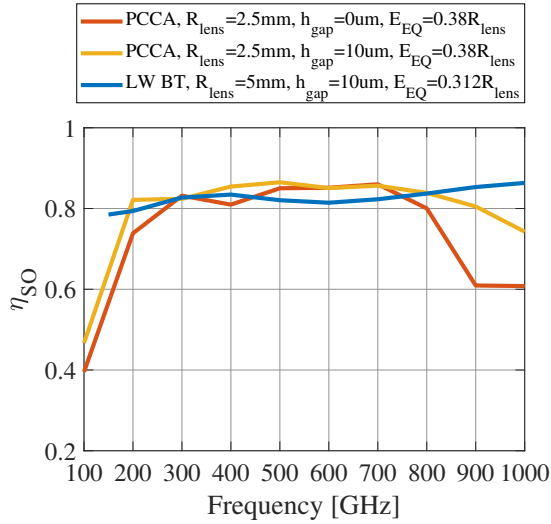


**Figure 5.7:** Spillover efficiency on a parabolic reflector vs frequency for the "final" structures considered in Table 5.2.

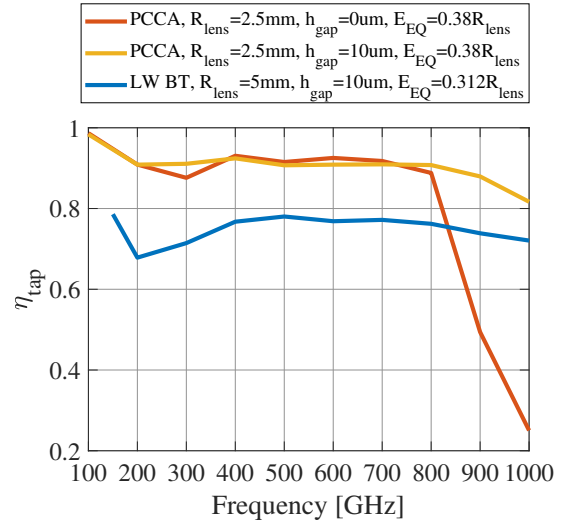


**Figure 5.8:** Taper efficiency on a parabolic reflector vs frequency for the "final" structures considered in Table 5.2.

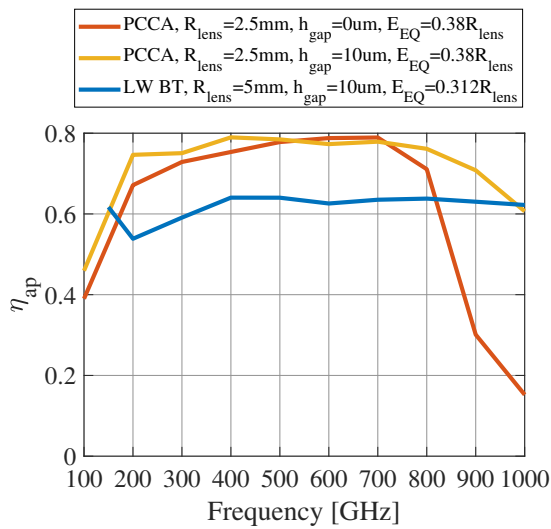


**Figure 5.9:** Aperture efficiency on a parabolic reflector vs frequency for the "final" structures considered in Table 5.2.

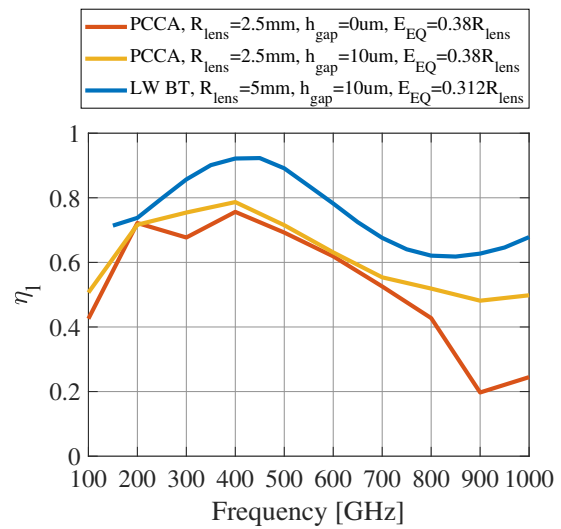


**Figure 5.10:** Lens efficiencies for the "final" structures considered in Table 5.2.

### 5.3. Conclusions

The extension length of the PCCA is optimized by considering the aperture efficiency on a canonical parabolic reflector. From this analysis, it is found that the elliptically extended PCCAs can obtain higher aperture efficiencies compared to the hyper-hemispherically extended PCCAs, while a similar lens efficiency is obtained for both cases. The f-number required for the considered PCCA geometries is reduced by reducing the PCCA lens radius in order to make it more practical in an imaging setup. For the PCCAs with the elliptical extension, high aperture efficiencies are obtained of around 70% – 80% from 200 GHz to 800 GHz.

# Design of an imaging setup for PCA benchmarking

In this chapter, an imaging setup is designed to benchmark the PCA geometries considered in Table 5.2. Simultaneously, this setup will serve as a proof of concept for a mm-resolution THz imaging system. A schematic overview of the envisioned setup is shown in Figure 6.1, where the radiation from a PCA in transmission is focused onto a spot on the object by a dielectric focusing lens. The reflected field is received by another PCA coupled to a focusing lens. First, the choice of the focusing component is explained and the dimensioning of the setup is done. After this, the focal fields are analyzed in terms of achieved resolution and main-beam efficiency. Finally, a reference case is studied, where a PCA and focusing lens in transmission are directly pointing to the receiving focusing lens and PCA, without any object in between. For this reference case, the maximum power that can be received by the receiver is evaluated via a field-matching formalism.

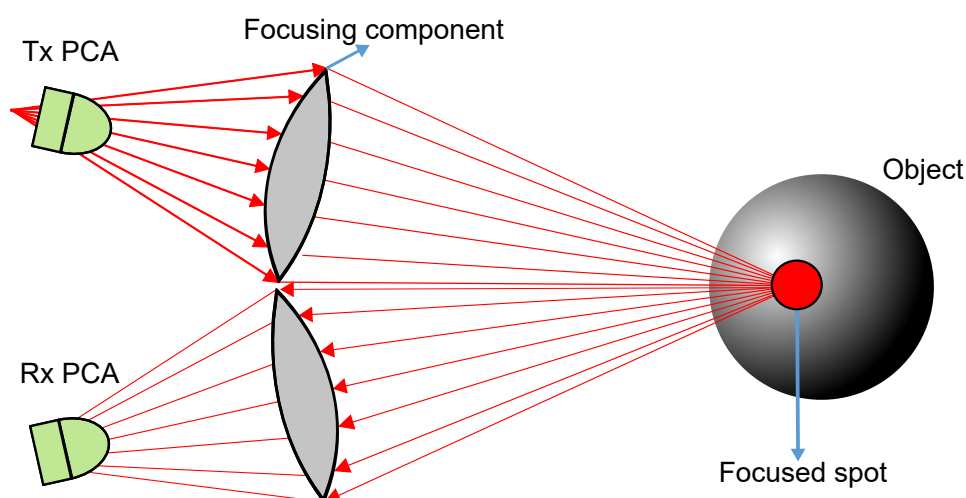


**Figure 6.1:** Schematic overview of the imaging setup, where the PCCAs are coupled to dielectric focusing lenses. The radiation from the transmitter is focused onto a spot on the object.

## 6.1. QO focusing component

For the focusing of the field transmitted by the PCA lens onto the object, either a dielectric focusing lens or a reflector geometry can be used. A reflector geometry has the benefit that it does not introduce dielectric losses or reflection losses. However, dielectric focusing lenses are easy to fabricate and relatively cheap compared to a reflector geometry. Thus the dielectric focusing lenses are more suitable for a proof of concept. The impact of the dielectric- and reflection losses on the received power are considered in Section 6.1.1 and Section 6.3 respectively.

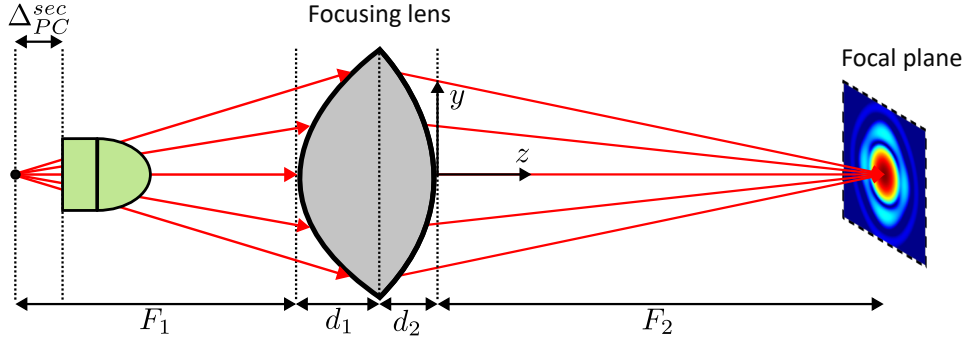


Figure 6.2: Schematic overview of a PCA lens coupled to a dielectric focusing lens.

The geometry of a simple bifocal dielectric lens with a radius of  $R_{foc}$  in combination with a PCA is shown in Figure 6.2. The focusing lens is made out of two hyperbolic surfaces, fully determined by their eccentricity and vertex distances [32]. The eccentricity is given by  $e = \sqrt{\epsilon_r^{foc}}$ , where  $\epsilon_r^{foc}$  is the relative permittivity of the lens material. The vertex distance of the side facing the PCA is  $2a_1 = 2F_1/(1+e)$  and vertex distance of the side facing the focussed spot is  $2a_2 = 2F_2/(1+e)$ . Here  $F_1$  is the focal distance from first focus to the lens, and is found using the optimal f-numbers  $f_{\#}$  for the different PCAs as listed in Table 5.2, where  $F_1 = f_{\#}D_{foc}$  and  $D_{foc}$  is the diameter of the focusing lens. The second focus  $F_2$  is equal to the desired imaging distance  $R_{image}$ . The thickness of the individual parts of the lens  $d_1$  and  $d_2$  are expressed as:

$$d_1 = \sqrt{a_1^2 + \frac{R_{foc}}{e^2 - 1}} - a_1 \quad (6.1a)$$

$$d_2 = \sqrt{a_2^2 + \frac{R_{foc}}{e^2 - 1}} - a_2 \quad (6.1b)$$

### 6.1.1. Lens dimensions and losses

To determine the diameter of the focusing lens, several factors are considered. The field amplitude close to the focal plane of the focusing lens has the same properties as that of the far-field [33]. Therefore, the Half Power Beam Width (HPBW) of the focal plane field of a lossless lens illuminated with  $\eta_{ap} = 100\%$  is approximately given by the HPBW of the Airy pattern:

$$\Delta_x^{ideal} \approx 1.02 R_{image} \cdot \frac{\lambda_0}{D_{foc}} \quad (6.2)$$

The HPBW of the focused spot will determine the resolution of the imaging system. Thus, to obtain the desired resolution for a certain  $R_{image}$ , one could in principle scale the diameter of the focusing lens accordingly. However, careful attention should be paid to the dielectric losses of the focusing lens. As a reference, a low loss dielectric material called TOPAS ( $\epsilon_r^{foc} = 2.33$ ) is used for the focusing lenses. The loss tangent  $\tau$  shown in Figure 6.3 is extrapolated from values at 250 GHz and 500 GHz as given in [32]. Using the loss tangent, the attenuation factor  $A_{dB}$  is expressed as:

$$A_{dB}(f) = 8.686 \frac{\pi \sqrt{\epsilon_r^{foc}} \tau(f)}{\lambda_0(f)} \quad [\text{dB/m}] \quad (6.3)$$

The dielectric losses of the focusing lens are estimated using  $A_{dB}$  and the thickness in the middle of the lens  $d_{tot} = d_1 + d_2$ , giving a loss in dB of  $L_{dB} = A_{dB} \cdot d_{tot}$ .

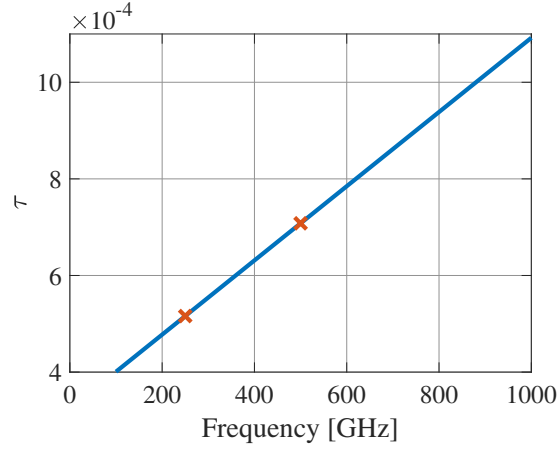


**Figure 6.3:** Estimated loss tangent of TOPAS. Note that the crosses indicate the values for the loss tangent given in [32].

Thus, the choice of  $D_{foc}$  and  $R_{image}$  influence both the lens losses and HPBW of the focal field. The lens losses  $L_{dB}$  and  $\Delta_x^{ideal}$  are shown in Figure 6.4 and Figure 6.5 respectively at the central frequency of 500 GHz for varying  $D_{foc}$  and  $R_{image}$ . Note that here the dielectric losses of the focusing lens are different for the PCCAs compared to the LW-BT, due to the different values of  $F_1$  chosen.

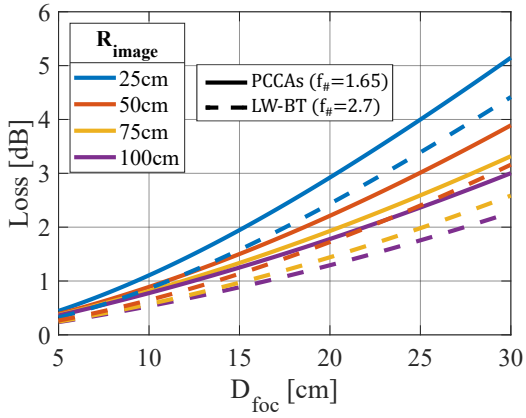


**Figure 6.4:** Losses of the focusing lenses at  $f = 500$  GHz for varying focusing lens size and imaging distance.

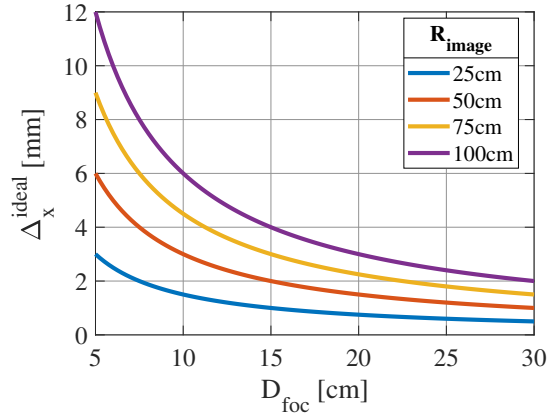


**Figure 6.5:** HPBW of the airy-pattern at  $f = 500$  GHz for varying focusing lens size and imaging distance.

For this project, an imaging distance of  $R_{image} = 0.5$  m is adequate for showing the potential of this type of system. Choosing  $R_{image} = 0.5$  m allows for a HPBW on the focal plane of  $\Delta_x^{ideal} = 2$  mm with a reflector of  $D_{foc} = 15$  cm. resulting in limited losses of about 1 dB – 1.5 dB at the central frequency for both the PCCAs and LW-BT. Note that these values are chosen specifically for a proof of concept using dielectric focusing lenses. In the final system, one can use a reflector and scale it based on set requirements without suffering the consequence of dielectric losses like in the case with the dielectric lenses. The geometrical parameters of the designed focusing lenses are listed in Table 6.1. The dielectric loss efficiency  $\eta_{loss}^{foc}$  quantifying the dielectric losses for the chosen focusing lens size is shown in Figure 6.6. Figure 6.7 shows  $\Delta_x^{ideal}$  for the chosen lens size and imaging distance.

**Table 6.1:** Geometrical parameters of the designed focusing lenses.

	$F_1$ [cm]	$F_2$ [cm]	$a_1$ [cm]	$a_2$ [cm]	$d_1$ [cm]	$d_2$ [cm]
PCCA focusing lens	24.75	50	9.80	19.79	1.96	1.04
LW-BT focusing lens	40.5	50	16.03	19.79	1.27	1.04

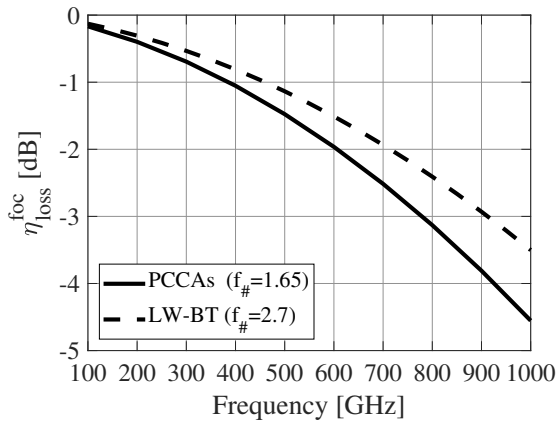


**Figure 6.6:** Dielectric loss efficiency  $\eta_{loss}^{foc}$  quantifying the losses of a single focusing lens vs frequency for the lenses considered in Table 6.1.

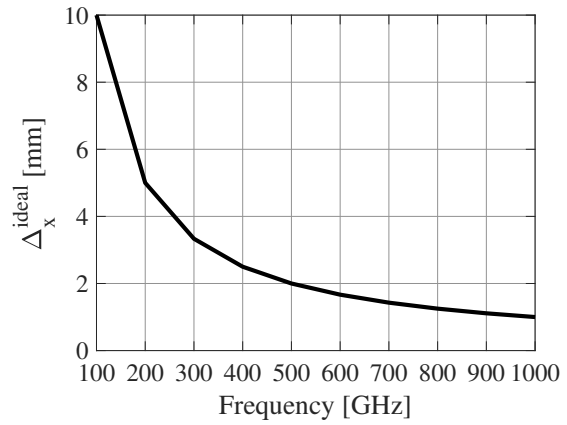


**Figure 6.7:** HPBW of the airy-pattern vs frequency for the lenses considered in Table 6.1.

## 6.2. Focal fields

The fields in the focal plane of the focusing lenses are evaluated with a PO procedure using GRASP. The amplitude of the electric fields on the focal plane  $\vec{E}_{Tx}^{Sc}$  at 400 GHz, 700 GHz and 1000 GHz are shown in Figure 6.8, while the magnitude of fields at the other considered frequencies is shown in Appendix G.

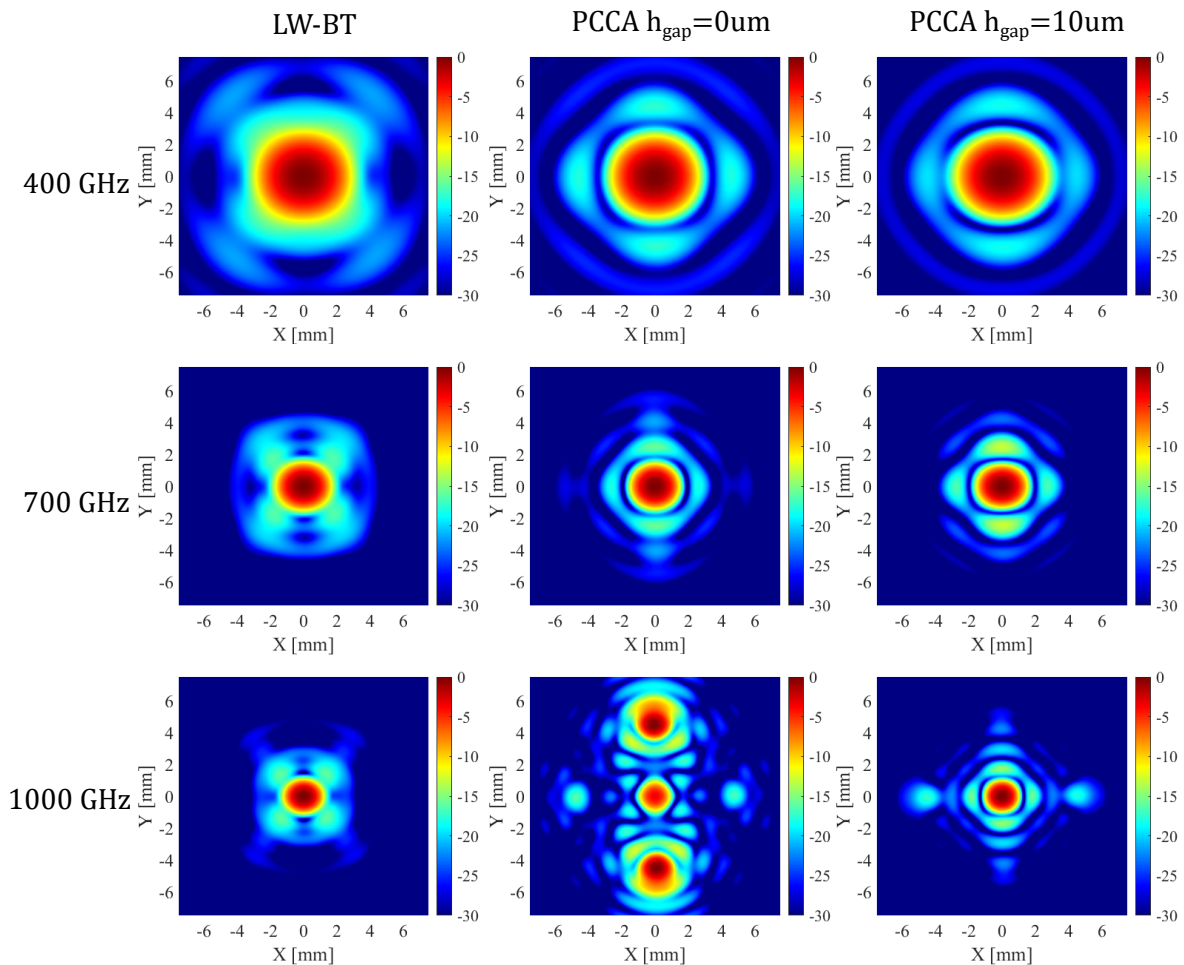


**Figure 6.8:** Focal fields of the focusing lenses for the considered structures at 400 GHz, 700 GHz and 1000 GHz.

To characterize the quality of the focal fields, the main beam efficiency and resolution are considered. The main beam efficiency  $\eta_{MB}$  quantifies how much of the total power is contained within the main beam, and is defined as follows:

$$\eta_{MB} = \frac{\int_0^{2\pi} \int_0^{R_{MB}} \left| \vec{E}_{Tx}^{Sc}(\rho, \phi) \right|^2 \rho d\rho d\phi}{\int_0^{2\pi} \int_0^{\infty} \left| \vec{E}_{Tx}^{Sc}(\rho, \phi) \right|^2 \rho d\rho d\phi} \quad (6.4)$$

where  $R_{MB}$  for the main-beam efficiency is defined as the radius on the focal plane from the center of the beam to the point where the field is  $-10$  dB. The main-beam efficiency is shown in Figure 6.9 together with  $R_{MB}$ . Similar values for the main-beam efficiency are obtained when comparing the PCCAs with the LW-BT.

To define the resolution of the system, instead of looking at the focal fields of the transmitter, one should also consider the effect of the receiver. In this work, the receiver and transmitter are always identical. Due to reciprocity, the receiving antenna will have the same properties in reception as in transmission. One can then define a two-way amplitude power pattern, which is proportional to the focal field of the transmitter to the power four:  $\left| \vec{E}_{Tx}^{Sc}(\rho, \phi) \right|^4$ . The resolution is defined as the average HPBW over all  $\phi$  cuts of the two-way amplitude pattern. The relation between frequency and resolution of the different structures considered is shown in Figure 6.10. Here a comparison is done with the maximum achievable resolution of the two-way pattern, which is approximately  $\Delta_x^{ideal} / \sqrt{2}$ .

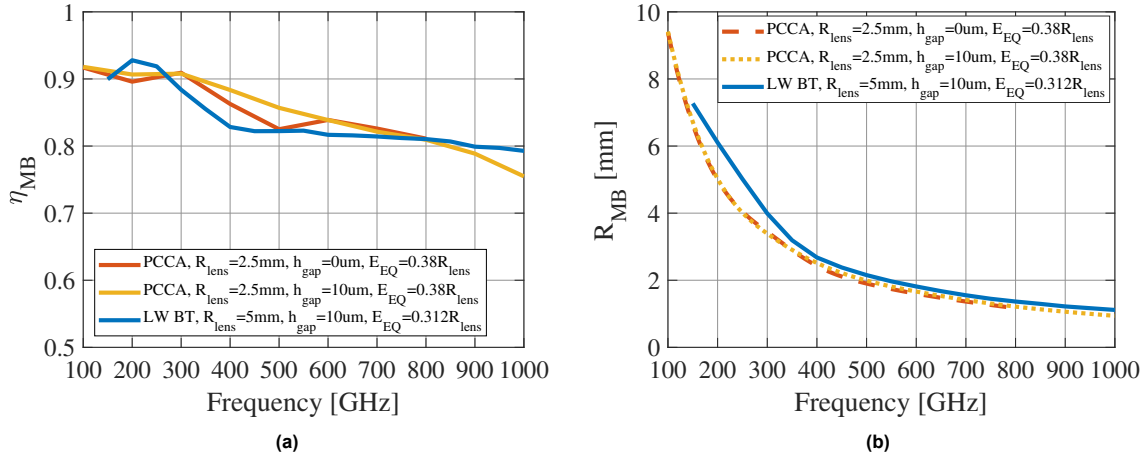


**Figure 6.9:** (a) Main beam efficiency and the (b) main-beam radius  $R_{MB}$  used of the focal fields of the imaging setup for the structures considered.

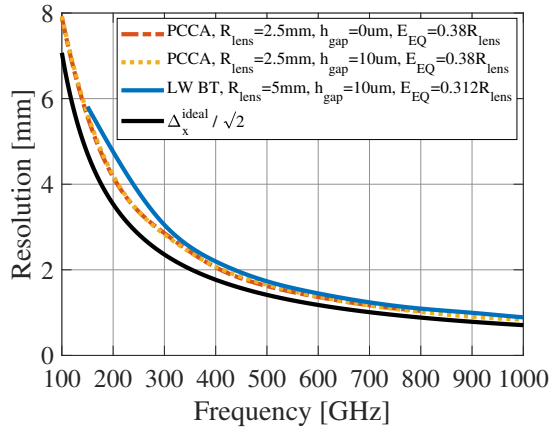


**Figure 6.10:** Resolution of the imaging setup for the different structures considered.

Note here that for the  $h_{gap} = 0 \mu\text{m}$  PCCA the quantities in Figure 6.9 and Figure 6.10 are only evaluated up until 800 GHz due to the fact that when the grating lobes are present the main beam is not in the center.

From Figure 6.10, it is evident that the highest resolution (or smallest two-way HPBW) is obtained with the PCCAs and the LW-BT has a slightly lower resolution (larger two-way HPBW). This result is also expected from the taper efficiencies evaluated in Chapter 5 (Figure 5.8). The PCCAs have a higher taper efficiency on the focusing lenses, which causes a more directive field in the focal plane, giving a slightly better resolution compared to the LW-BT.

### 6.2.1. Depth of Field

The Depth of Field (DoF) of a focusing component is defined as the length along the axis of the focusing component of the region in which the field is approximately focussed. The DoF thus determines the region in which the imaging system can be used. In this work, the focused region is defined as the region along the reflector axis in which the field stays within  $3\text{dB}$  of the maximum value.

Another effect to consider is that the field focused by a focusing component might not have its maximum intensity aligned with the geometrical focus of the focusing component. Both the DoF and shift of the focal point are related to the Fresnel number  $N$  of the focusing component, which is given by:

$$N = \frac{D_{foc}^2}{4\lambda_0 R_{image}} \quad (6.5)$$

The expressions given in [34] are used to evaluate the true focal point and DoF in case the scattered field by the lens is a perfect uniform spherical wave. The focal point and edges of the depth of field ( $\Delta_z^{min}$  and  $\Delta_z^{max}$ ) are shown in Figure 6.11.

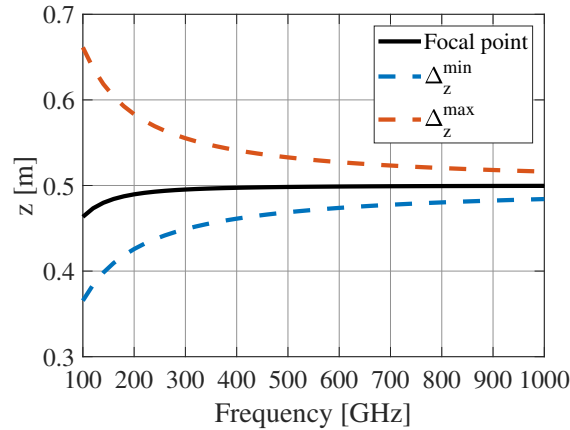


Figure 6.11: Location of the focal point and the DoF in case the scattered field by the lens is a uniform spherical wave.

From Figure 6.11 it is evident that at the geometrical focus at  $z = R_{image} = 0.5$ , the field is always considered to be in acceptable focus. Also, as the frequency increases, the focal point gets closer to the geometrical focus. Note that the DoF is roughly proportional to  $\lambda_0 (R_{image}/D_{foc})^2$  for  $N \geq 5$ . This means a tradeoff between resolution and DoF exists, where the DoF roughly scales quadratically with  $R_{image}/D_{foc}$  while the two-way HPBW scales linearly with  $R_{image}/D_{foc}$ .

## 6.3. Link benchmarking analysis

To benchmark the different PCAs with their designed imaging lens, a reference case is studied where a PCA together with a focusing lens in transmission is directly coupled to a PCA with a focusing lens in reception. The setup is shown in Figure 6.12. In this section, the link between the Tx and Rx PCAs in the setup of Figure 6.12 is studied. First, the QO path is fully quantified, and then the open circuit voltage at the receiver side is found using a field matching formalism [21]. Using the open circuit voltage at the receiver, the maximum available received power is evaluated.

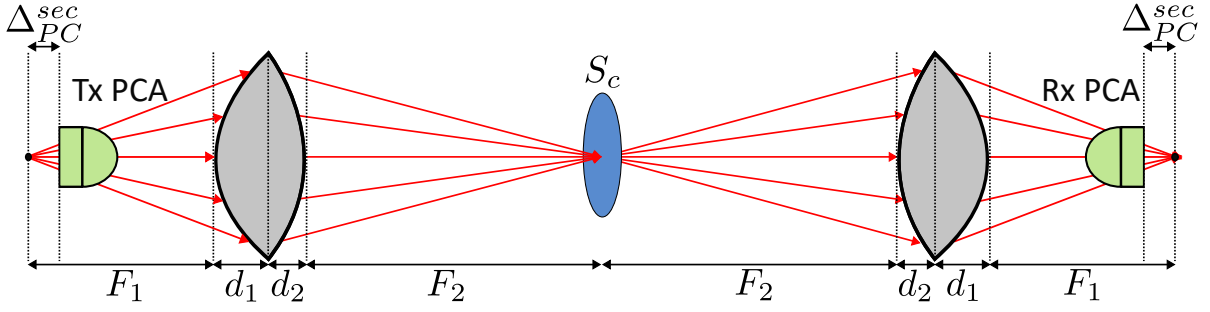


Figure 6.12: Schematic overview of the benchmarking setup used to study the coupling between two PCAs with focusing lenses.

### 6.3.1. QO losses

In Figure 5.10, the lens efficiency  $\eta_l$  is defined to quantify the losses associated with the PCAs considered for imaging. The lens efficiency quantifies the losses due to the front-to-back ratio of the feed, and spillover- and reflection losses on the PCA lens. The losses associated with the focusing lenses are dielectric losses, spillover losses, and reflection losses, where the dielectric losses are shown in Figure 6.6. The spillover and reflection are found from the focal fields evaluated by GRASP from Section 6.2. Here, in GRASP, the lenses are assumed to be free from dielectric losses. The product of the spillover and reflection efficiency of a single focusing lens is then found as:

$$\eta_{SO}^{foc}(f)\eta_{ref}^{foc}(f) = \frac{P_{Tx}^{S_c}(f)}{P_{sec}^{Tx}(f)} \quad (6.6)$$

where  $P_{sec}^{Tx}$  is the power in the secondary field of the Tx PCA. Figure 6.13 shows  $\eta_{SO}^{foc}(f)\eta_{ref}^{foc}(f)$  for the different structures.

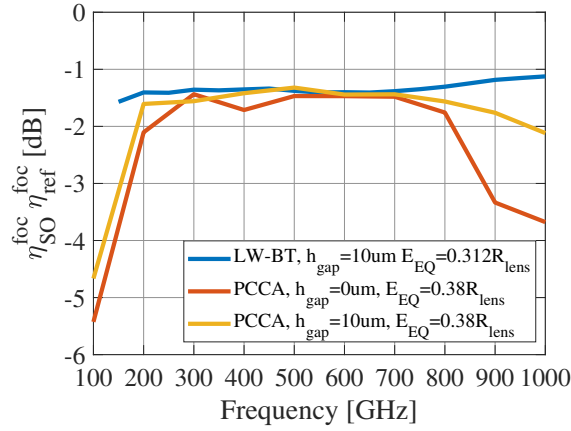


Figure 6.13: Efficiency terms  $\eta_{SO}^{foc}(f)\eta_{ref}^{foc}(f)$  quantifying the spillover and reflection losses on a single focusing lens for the different structures.

### 6.3.2. Field matching

To find the maximum available power that can be received by the receiving antenna (PCA 2), one can resort to the use of a field-matching technique [35]. More specifically, the open circuit voltage  $V_{oc}$  at the receiving antenna is evaluated by a reaction integral in the focal plane:

$$V_{oc}(f)I_{Tx}(f) = \frac{2}{\zeta_0} \iint_{S_c} \vec{E}_1^{S_c} \cdot \vec{E}_2^{S_c} dS, \quad (6.7)$$

where  $\vec{E}_1^{S_c}$  and  $\vec{E}_2^{S_c}$  are the fields on the focal plane produced by PCA 1 and PCA 2 respectively in transmission. The current  $I_{Tx}$  is the current excitation used in PCA 2 which produces the field  $\vec{E}_2^{S_c}$  on the focal plane. To study the coupling between two PCAs with focusing lenses, a case is considered

where the receiver is represented by a Thevenin circuit in reception, which is shown in Figure 6.14. The power lost due to a mismatch between the receiving antenna and its load is not taken into account here, meaning the receiver load is considered matched with the antenna ( $Z_L = Z_a^*$ ). The power in the matched load of the receiving antenna can then be expressed as:

$$P_2^{load} = \frac{|V_{oc}(f)|^2}{8R_a}, \quad (6.8)$$

where  $R_a$  is the real part of the antenna impedance. In transmission, the same antenna would radiate a power  $P_2^{rad} = \frac{1}{2}R_a|I_{Tx}|^2$  when excited by a current  $I_{Tx}$ . One can then express  $R_a$  in terms of the radiated power as:

$$R_a = \frac{2P_2^{rad}}{|I_{Tx}(f)|^2}. \quad (6.9)$$

Upon substituting Equation 6.8 into Equation 6.9, the following relation is obtained:

$$P_2^{load} = \frac{|V_{oc}(f)I_{Tx}(f)|^2}{16P_2^{rad}}, \quad (6.10)$$

To quantify the efficiency of the full setup, a link efficiency can be defined as the ratio between the power delivered to a matched receiver  $P_2^{load}$  and the power that is radiated by the feed of the transmitting PCA  $P_1^{rad}$ :

$$\eta_{link} = \frac{P_2^{load}}{P_1^{rad}} = \frac{|V_{oc}(f)I_{Tx}(f)|^2}{16P_2^{rad}P_1^{rad}}. \quad (6.11)$$

Note from Equation 6.7 that the  $|V_{oc}(f)I_{Tx}(f)|$  term will be maximal when either  $\vec{E}_1^{S_c} = (\vec{E}_2^{S_c})^*$  or when the result of the product  $\vec{E}_1^{S_c} \cdot \vec{E}_2^{S_c}$  has a uniform phase over the field matching surface. In both cases, there are no losses associated with a mismatch between the focal fields of the receiving and transmitting antenna. In general, an efficiency term can be defined which quantifies the loss of power due to the mismatch in the fields, which in this work is called the field-matching efficiency  $\eta_{FM}$ . Equation 6.7 and Equation 6.11 can be further simplified by considering that  $\vec{E}_1^{S_c} = \vec{E}_2^{S_c}$  due to the symmetry of the secondary fields. The link efficiency can then be expressed as:

$$\eta_{link} = \frac{\left| \frac{2}{\epsilon_0} \int_{S_c} \vec{E}_1^{S_c} \cdot \vec{E}_1^{S_c} dS \right|^2}{16(P_{prim}^{tot})^2} = (\eta_l \cdot \eta_{SO}^{foc} \cdot \eta_{ref}^{foc})^2 \cdot \eta_{FM}, \quad (6.12)$$

with  $P_{prim}^{tot}$  being the total power in the primary fields as earlier defined in Chapter 2. The link efficiency in Equation 6.12 is expressed in terms of several known efficiency terms, and the field matching efficiency  $\eta_{FM}$ . Note here that  $\eta_{link}$  does not include  $\eta_{loss}^{foc}$ , as the lenses are considered lossless in GRASP. Adding the dielectric losses for the two focusing lenses results in the total efficiency of the link, quantified by  $\eta_{link}^{tot} = \eta_{link}(\eta_{loss}^{foc})^2$ . The field-matching efficiency and total link efficiencies are shown in Figure 6.15 and Figure 6.16 respectively.

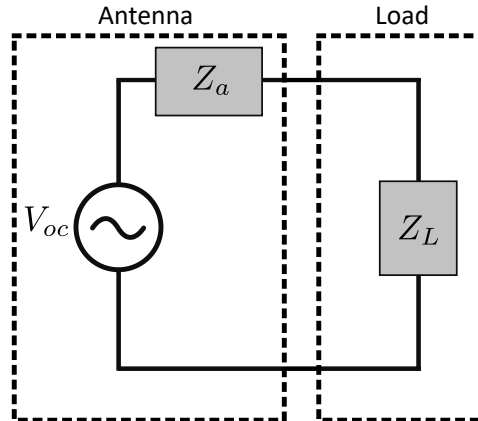
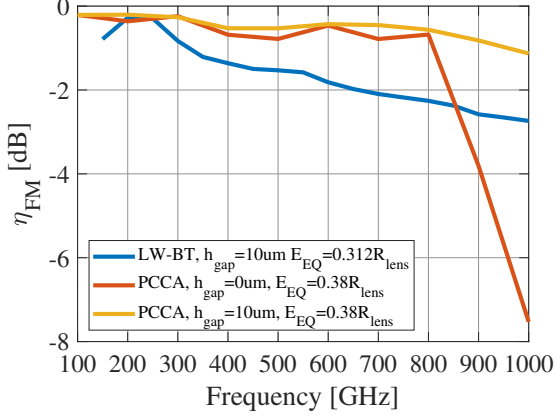
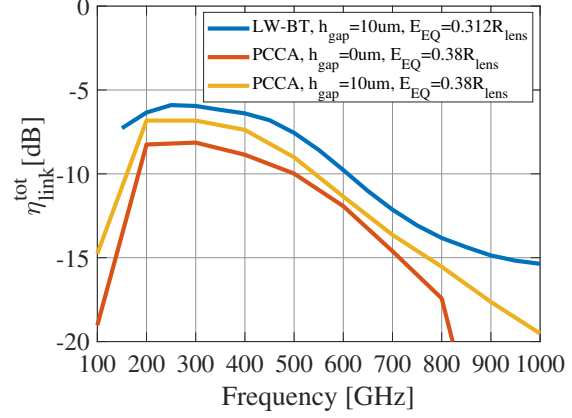


Figure 6.14: Frequency domain Thevenin equivalent circuit in reception.

Figure 6.15: Field matching efficiency  $\eta_{FM}$ .Figure 6.16: Total link efficiency  $\eta_{link}^{tot}$ .

The field matching efficiency in Figure 6.15 shows that for the PCCAs, generally a higher field-matching efficiency is obtained compared to the LW-BT. This can be attributed to the fact that the phase variation over the focal spot patterns is generally larger for the LW-BT compared to the PCCAs. This is in turn mainly related to more significant phase variations of the secondary field for the LW-BT compared to the PCCAs, which causes the field on the focus to have a more significant phase variation. The higher phase variation of the LW-BT on the focal plane translates to a loss in field-matching efficiency.

The frequency dependence of the field matching efficiency for the LW-BT due to the phase variation can be understood by considering the phase center of the LW-BT PCA. While the calculated phase center of the secondary field  $\Delta_{PC}^{sec}$  is aligned with the first focus of the focusing lens, the "best" point to choose for the phase center shifts with frequency. The frequency dependence of the phase center will result in a frequency-dependent shift of the second focus of the focusing lenses. Because the field does not exactly focalize on the field-matching surface, a phase variation is present on the field-matching surface which causes a drop in the field-matching efficiency. For the PCCAs, this effect is not as significant as for the LW-BT, resulting in a generally higher field-matching efficiency. To back up this claim, the PEL on the equivalent aperture of a parabolic reflector with the same size as the focusing lenses is shown in Appendix H, where a similar frequency dependence is observed as in the field-matching efficiency. Furthermore, the effect of the grating lobes is clearly visible as a drop in the field matching efficiency above 800 GHz for the PCCA with  $h_{gap} = 0 \mu\text{m}$ . The field matching efficiency drops significantly in the presence of grating lobes or significant sidelobes in the secondary field as they are usually out of phase with the main beam.

For the total link efficiencies shown in Figure 6.16, the LW-BT has the highest total link efficiency, which is mainly due to the higher lens efficiency  $\eta_l$  (Figure 5.10) and higher dielectric loss efficiency  $\eta_{loss}^{foc}$  (Figure 6.6) compared to the PCCAs.

### 6.3.3. Receiver energy spectra and power

Using the obtained link efficiency, one can find the energy spectral density of the received power at an ideal receiver,  $E_{s,Rx}^{ideal}$ , by multiplying the spectral density of the transmitting PCA  $E_{s,Tx}$  by the total link efficiency:

$$E_{s,Rx}^{ideal}(f) = E_{s,Tx}(f) \cdot \eta_{link}^{tot}(f) \quad (6.13)$$

Note that part of the signature of the receiving PCA is ignored in this case, as the antenna is assumed to be matched to the load. To fully take into account the receiving PCA, one would have to evaluate the time-domain Norton circuit in reception using the open-circuit voltage as found from the field-matching procedure. This is however not yet considered in this work and is regarded as future work.

The energy spectra considering ideal receivers are evaluated for the considered PCA structures, where for the laser power and bias voltage the maximum possible values are taken. The constant parameters used to evaluate the Norton circuit can be found in Table 2.3. The remaining parameters together with the power generated in the transmitter  $P_1^{rad}$  and the maximum power received at the receiver  $P_2^{load}$  as calculated from the spectra are given in Table 6.2. The corresponding transmitter and receiver energy

spectra are shown in Figure 6.17. Note here that for the LW-BT, the maximum possible values for the bias voltage and laser power, as increasing either the bias voltage or laser power would cause dielectric breakdown[9].

**Table 6.2:** Parameters used for the evaluation of the spectra in Figure 6.17, and the associated radiated powers in transmission and reception.

Structure	$\tilde{P}_L$ [mW]	$\eta_{SO,Laser}^{ML}$	$\eta_{SO,Laser}^{Gap}$	$\tilde{P}_{gap}$ [mW]	$V_b$ [V]	Radiated power ( $P_1^{rad}$ ) [mW]	Received power ( $P_2^{load}$ ) [mW]
PCCA, $h_{gap} = 0 \mu\text{m}$	178	0.58	0.537	2.22	80	1.23	0.128
PCCA, $h_{gap} = 10 \mu\text{m}$	178	0.58	0.537	2.22	80	1.65	0.177
LW-BT	100	~	0.38	38	30	0.176	0.034

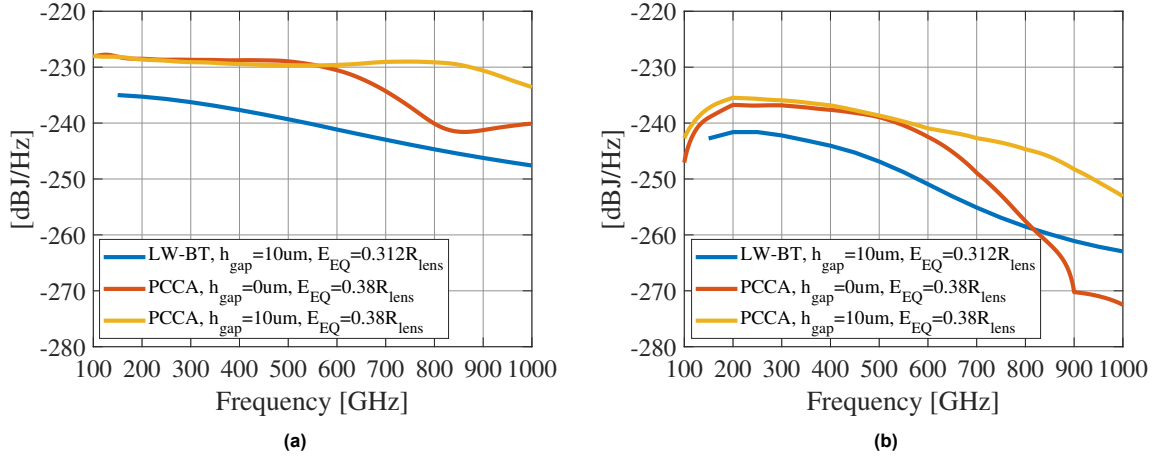


**Figure 6.17:** Energy spectrum of the transmitted spectrum (a) and the energy spectrum received by an ideal receiver with matched load (b) for the PCA geometries considered.

Note here that for the LW-BT, the radiated power  $P_1^{rad}$  and the received power at the load  $P_2^{load}$  are calculated in a frequency band from 150 GHz – 1000 GHz, while for the PCCAs a frequency band from 100 GHz – 1000 GHz is considered. The LW-PCCA performs best when considering the power at a matched receiver, followed by the PCCA with  $h_{gap} = 0 \mu\text{m}$  and the LW-BT. Even though the LW-BT has a higher total link efficiency, it radiates the least power due to the lower laser power and bias voltage that can be applied before dielectric breakdown occurs.

Comparing the PCCAs, the LW-PCCA radiates the most power and has a higher energy spectral density at the receiver over the considered frequency band, which can be attributed to the higher total link efficiency compared to the PCCA with  $h_{gap} = 0 \mu\text{m}$ .

## 6.4. Conclusions

The goal of this chapter was to design an imaging setup to benchmark the PCA geometries considered in Table 5.2 of Chapter 5. Focusing lenses are designed to focalize the field at a distance of  $R_{image} = 0.5 \text{ m}$ . With a diameter of  $D_{foc} = 0.15 \text{ cm}$ , the dielectric losses are in the order within 1 dB – 1.5 dB at the central frequency. To benchmark the different PCAs with their newly designed focusing lenses, the coupling between PCAs is studied via a field-matching formalism. The power at an ideal receiver is found, and the total link efficiency is found quantifying the fraction of the power that is received at the receiver. The total link efficiency is higher over the considered frequency band for the LW-BT, mainly due to its higher lens efficiency and lower dielectric focusing lens losses compared to the PCCAs.

# Conclusions and future work

## 7.1. Summary and conclusions

This work consists of two parts, where the first part is about the characterization of PCCA antennas, and the second part is about the design of an imaging setup.

First, the concept of the LW-PCCA is introduced in Chapter 2 and compared with the PCCA design developed by Garufo et al., [15]. The PCCA without a leaky wave cavity suffers from grating lobes and destructive mutual coupling effects due to the period of the array. Adding a leaky wave cavity to the PCCA enhances the bandwidth of such structures, as it effectively suppresses the grating lobes and destructive mutual coupling effects. A PCCA with an air cavity of  $h_{gap} = 10 \mu\text{m}$  is found to result in the largest bandwidth.

In Chapter 3, a Physical Optics method is discussed to find the fields radiated by the silicon lenses of the PCCAs. Instead of using the primary fields of the array, a PO method based on the use of the Embedded Element Patterns is introduced. The PO method based on EEPs provides a convenient way to get the secondary fields in case the lens is not in the far field of the array. The secondary fields of the fabricated PCCA structures are evaluated using the introduced PO method based on EEPs. Using the evaluated secondary fields, the effect of the dielectric lens on the spectrum of the radiated field and the effect on the corresponding radiated power is quantified for the fabricated PCA geometries.

Subsequently in Chapter 4, first a power-measurement experiment is considered. The QO path of the measurement setup is modeled, and the power received by a PM5 is predicted and compared to measurements. From the measurement results, it is evident that the model does not predict several saturation effects occurring for increasing laser power and bias voltage. The saturation effects for increasing laser power are likely not predicted accurately due to the assumptions made on the array impedance. An analytical description of the array impedance is needed to accurately predict the radiated spectrum by the PCCAs, and possibly an equivalent of the single-element Norton time-domain model for the full array. Furthermore, measurements of the spectrum confirmed the positive effect of the added leaky wave cavity on the bandwidth of a PCCA.

Then in Chapter 5, the PCCA lenses are redesigned in order to couple well to a QO focusing component. The aperture efficiency on a canonical parabolic reflector geometry is considered, where an optimization is done for the extension length of the extended hemispherical lenses and the focal distance. The elliptical extension length provides the highest aperture efficiencies. To reduce the focal distance, the radius of the PCCA lenses is set to  $R_{lens} = 2.5 \text{ mm}$

Lastly, in Chapter 6 an imaging setup using dielectric focusing lenses is designed to benchmark the different PCA structures considered. Using the focusing lenses of  $D_{foc} = 0.15 \text{ cm}$ , the system achieves a lateral resolution of approximately 2 mm at the central frequency of 500 GHz with losses of about 1 dB – 1.5 dB per lens. The performance of the PCAs is studied via a field matching formalism, where the spectrum of the received energy is found in the case a matched load at the receiver is assumed. The total link efficiency is the highest for the LW-BT, which is mainly due to its better lens efficiency compared to the PCCAs.

## 7.2. Future work

In this chapter, several possibilities and recommendations for future work are given:

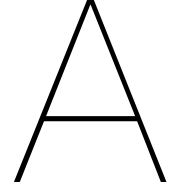
- Currently, the period of the connected arrays is determined by the microlens array which has the smallest period that was commercially available at the time of fabrication. At this time microlenses with smaller periods are commercially available[36], which allows the fabrication of PCCAs with a smaller array period. Moving to a smaller array period while keeping the same array size would be beneficial, as it would push both the grating lobes and destructive mutual coupling to higher frequencies. One can then also do a study on the optimal PC gap size for the laser power that is incident on each gap.
- Currently, the approximations on the impedance of the array lead to inaccuracies in the modeling. An analytical description of the array impedance should be developed to get a more accurate idea of the array impedance, possibly leading to more accurate modeling of the radiated spectra of PCCA structures.
- A better matching layer can be designed for the PCCA lenses in order to obtain higher lens efficiencies. This could be done using multiple dielectric layers as is done in [17]. Another way this can be realized is by making a matching layer based on imprinted sub-wavelength structures on a high-dielectric material as done in [37].
- In Section 6.3, currently the receiver is assumed to have a load matched to the antenna. However, the signature of the receiving PCA is neglected when assuming a matched load at the receiver. To truly get an idea of what is received by the receiver, one should use the Norton PCA circuit in reception for the receiver. Using the received power, one can make an estimate of the SNR that can be expected, and thus the integration time needed for a certain FoV.
- Using TICRA GRASP and a field-matching formalism, one can simulate a true imaging scenario where a picture is made of an object. A simulation together with measurements can truly show the potential of these systems.

# References

- [1] Masayoshi Tonouchi. "Cutting-edge terahertz technology". In: *Nature Photonics* 1.2 (Feb. 2007), pp. 97–105. ISSN: 1749-4885. DOI: 10.1038/nphoton.2007.3.
- [2] Leili Afsah-Hejri et al. "A Comprehensive Review on Food Applications of Terahertz Spectroscopy and Imaging". In: *Comprehensive Reviews in Food Science and Food Safety* 18.5 (Sept. 2019), pp. 1563–1621. ISSN: 1541-4337. DOI: 10.1111/1541-4337.12490.
- [3] Liu Yu et al. "The medical application of terahertz technology in non-invasive detection of cells and tissues: opportunities and challenges". In: *RSC Advances* 9.17 (2019), pp. 9354–9363. ISSN: 2046-2069. DOI: 10.1039/C8RA10605C.
- [4] Philip F. Taday. "Applications of terahertz spectroscopy to pharmaceutical sciences". In: *Philosophical Transactions of the Royal Society of London. Series A: Mathematical, Physical and Engineering Sciences* 362.1815 (Feb. 2004), pp. 351–364. ISSN: 1364-503X. DOI: 10.1098/rsta.2003.1321.
- [5] Ken B. Cooper et al. "THz imaging radar for standoff personnel screening". In: *IEEE Transactions on Terahertz Science and Technology* 1.1 (Sept. 2011), pp. 169–182. ISSN: 2156342X. DOI: 10.1109/TTHZ.2011.2159556.
- [6] D. H. Auston, K. P. Cheung, and P. R. Smith. "Picosecond photoconducting Hertzian dipoles". In: *Applied Physics Letters* 45.3 (Aug. 1984), pp. 284–286. ISSN: 0003-6951. DOI: 10.1063/1.95174.
- [7] Peter Uhd Jepsen, David G. Cooke, and Martin Koch. "Terahertz spectroscopy and imaging - Modern techniques and applications". In: *Laser & Photonics Reviews* 5.1 (Jan. 2011), pp. 124–166. ISSN: 18638880. DOI: 10.1002/lpor.201000011.
- [8] Nathan M. Burford and Magda O. El-Shenawee. "Review of terahertz photoconductive antenna technology". In: *Optical Engineering* 56.1 (Jan. 2017), p. 010901. ISSN: 0091-3286. DOI: 10.1117/1.OE.56.1.010901.
- [9] Arturo Fiorellini Bernardis. "On the Modelling and Characterisation of Photoconducting Antennas". PhD thesis. DOI: 10.4233/uuid:469e35d4-7aa8-4301-94a0-17baceb3af1c.
- [10] Nuria Llobart and Andrea Neto. "THz time-domain sensing: The antenna dispersion problem and a possible solution". In: *IEEE Transactions on Terahertz Science and Technology* 2.4 (2012), pp. 416–423. ISSN: 2156342X. DOI: 10.1109/TTHZ.2012.2197949.
- [11] Paolo Maria Sberna et al. "Leaky Lens Photo-Conductive Antennas on LT GaAs membranes". In: *2021 46th International Conference on Infrared, Millimeter and Terahertz Waves (IRMMW-THz)*. IEEE, Aug. 2021, pp. 1–1. ISBN: 978-1-7281-9424-0. DOI: 10.1109/IRMMW-THz50926.2021.9566890.
- [12] Alessandro Garufo et al. "A Connected array of coherent photoconductive pulsed sources to generate mw average power in the submillimeter wavelength band". In: *IEEE Transactions on Terahertz Science and Technology* 9.3 (2019), pp. 221–236. ISSN: 2156342X. DOI: 10.1109/TTHZ.2019.2896791.
- [13] Andrea Neto and J. J. Lee. "Ultrawide-Band Properties of Long Slot Arrays". In: *IEEE Transactions on Antennas and Propagation* 54.2 (2006), pp. 534–543. ISSN: 15582221. DOI: 10.1109/TAP.2005.863140.
- [14] Daniele Cavallo. "Connected array antennas : analysis and design". PhD thesis. Technische Universiteit Eindhoven, 2011. DOI: 10.6100/IR719461. URL: <https://doi.org/10.6100/IR719461>.
- [15] Alessandro Garufo. "Towards the Engineering of Pulsed Photoconductive Antennas". PhD thesis. 2017, p. 289. ISBN: 978-94-028-0657-1.

- [16] Arturo Fiorellini Bernardis et al. *Signal to Noise Ratio Budget of a Pico-Seconds Pulsed Radar System for Stand-Off Imaging*. Tech. rep. 2019.
- [17] Andrea Neto. “UWB, non dispersive radiation from the planarly fed leaky lens antenna part 1: Theory and design”. In: *IEEE Transactions on Antennas and Propagation* 58.7 (July 2010), pp. 2238–2247. ISSN: 0018926X. DOI: 10.1109/TAP.2010.2048879.
- [18] Nuria Llombart et al. “Impact of mutual coupling in leaky wave enhanced imaging arrays”. In: *IEEE Transactions on Antennas and Propagation* 56.4 (Apr. 2008), pp. 1201–1206. ISSN: 0018926X. DOI: 10.1109/TAP.2008.919223.
- [19] Dassault Systèmes. *CST Microwave Studio*. 2018. URL: <https://www.3ds.com/>.
- [20] Daniele Cavallo, Andrea Neto, and Giampiero Gerini. “Analytical description and design of printed dipole arrays for wideband wide-scan applications”. In: *IEEE Transactions on Antennas and Propagation* 60.12 (2012), pp. 6027–6031. ISSN: 0018926X. DOI: 10.1109/TAP.2012.2209856.
- [21] Huasheng Zhang, Andrea Neto, and Nuria Llombart. “On the Modelling of the Quasi-Optical Coupling between Two Photoconductive Antennas under Pulsed Laser Illumination”. In: *International Conference on Infrared, Millimeter, and Terahertz Waves, IRMMW-THz*. Vol. 2021-August. IEEE Computer Society, 2021. ISBN: 9781728194240. DOI: 10.1109/IRMMW-THz50926.2021.9567003.
- [22] Huasheng Zhang. “A GO/FO Tool for Analyzing Quasi-optical Systems in Reception”. PhD thesis. 2018.
- [23] Ozan Yurduseven, Daniele Cavallo, and Andrea Neto. “Wideband dielectric lens antenna with stable radiation patterns fed by coherent array of connected leaky slots”. In: *IEEE Transactions on Antennas and Propagation* 62.4 (2014), pp. 1895–1902. ISSN: 0018926X. DOI: 10.1109/TAP.2014.2298875.
- [24] TICRA. *GRASP*. 2019. URL: <https://www.ticra.com/>.
- [25] John M. Khosroffian and Bruce A. Garetz. “Measurement of a Gaussian laser beam diameter through the direct inversion of knife-edge data”. In: *Applied Optics* 22.21 (Nov. 1983), p. 3406.
- [26] Juan Bueno et al. “A Leaky Enhanced Photo-Conductive Connected Array for Efficient Generation of THz Power”. In: *EuCAP*. 2022.
- [27] Daniel F. Filipovic, Steven S. Gearhart, and Gabriel M. Rebeiz. “Double-Slot Antennas on Extended Hemispherical and Elliptical Silicon Dielectric Lenses”. In: *IEEE Transactions on Microwave Theory and Techniques* 41.10 (1993), pp. 1738–1749. ISSN: 15579670. DOI: 10.1109/22.247919.
- [28] Daniel F. Filipovic, George V. Eleftheriades, and Gabriel M. Rebeiz. *Off-Axis Imaging Properties of Substrate Lens Antennas*. Tech. rep.
- [29] Carlos A. Fernandes, Eduardo B. Lima, and Jorge R. Costa. “Dielectric Lens Antennas”. In: *Handbook of Antenna Technologies*. Singapore: Springer Singapore, 2016, pp. 1001–1064. DOI: 10.1007/978-981-4560-44-3.
- [30] Warren Stutzman and Gary Thiele. *Antenna Theory and Design*. 3rd ed. Wiley, 2012.
- [31] Andrea Neto, Nuria Llombart, and Daniele Cavallo. *Lecture notes for Quasi Optical Systems*. Tech. rep. Delft University of Technology.
- [32] Erio Gandini et al. “Wide Field of View Inversely Magnified Dual-Lens for Near-Field Submillimeter Wavelength Imagers”. In: *IEEE Transactions on Antennas and Propagation* 66.2 (Feb. 2018), pp. 541–549. ISSN: 0018926X. DOI: 10.1109/TAP.2017.2778016.
- [33] Joseph W. Goodman and Mary E. Cox. *Introduction to Fourier Optics*. 3rd ed. 2005. ISBN: 0974707724.
- [34] Yajun Li and Emil Wolf. “Focal shifts in diffracted converging spherical waves”. In: *Optics Communications* 39.4 (Oct. 1981), pp. 211–215. ISSN: 00304018. DOI: 10.1016/0030-4018(81)90108-5.
- [35] Marta Arias Campo et al. “On the Use of Fly’s Eye Lenses with Leaky-Wave Feeds for Wideband Communications”. In: *IEEE Transactions on Antennas and Propagation* 68.4 (Apr. 2020), pp. 2480–2493. ISSN: 0018-926X. DOI: 10.1109/TAP.2019.2952474.

- 
- [36] *MicroLens Arrays*. URL: <https://holographix.com/microlens-arrays/>.
- [37] Juan Bueno et al. "Lossless Matching Layer for Silicon Lens Arrays At 500 GHz Using Laser Ablated Structures". In: *IEEE Transactions on Terahertz Science and Technology* (2022), pp. 1–7. ISSN: 2156-342X. DOI: 10.1109/TTHZ.2022.3202031.



## Time-domain Norton circuit

Using the result from [9], the impressed current  $i_{impr}(t)$  and the generator current  $i_g(t)$  are given in Equation A.1 and Equation A.2 respectively. Due to the many parameters involved, not all of them are explained in the text. The full list of parameters and definitions can be found in Table 2.4 and Table 2.3.

$$i_{impr}(t) = \frac{q_e^2}{m_e} \frac{W_y W_z}{W_x} A \int_{-t_{min}}^t e^{-4 \ln 2 \frac{t''^2}{\tau_p^2}} \int_{t''}^t e^{-\frac{t-t'}{\tau_s}} V_b dt' e^{-\frac{t-t''}{\tau_c}} dt'' \quad (\text{A.1})$$

$$i_{gen}(t) = \frac{q_e^2}{m_e} \frac{W_y W_z}{W_x} A \int_{-t_{min}}^t e^{-4 \ln 2 \frac{t''^2}{\tau_p^2}} \int_{t''}^t e^{-\frac{t-t'}{\tau_s}} (v_{rad}(t')) dt' e^{-\frac{t-t''}{\tau_c}} dt'' \quad (\text{A.2})$$

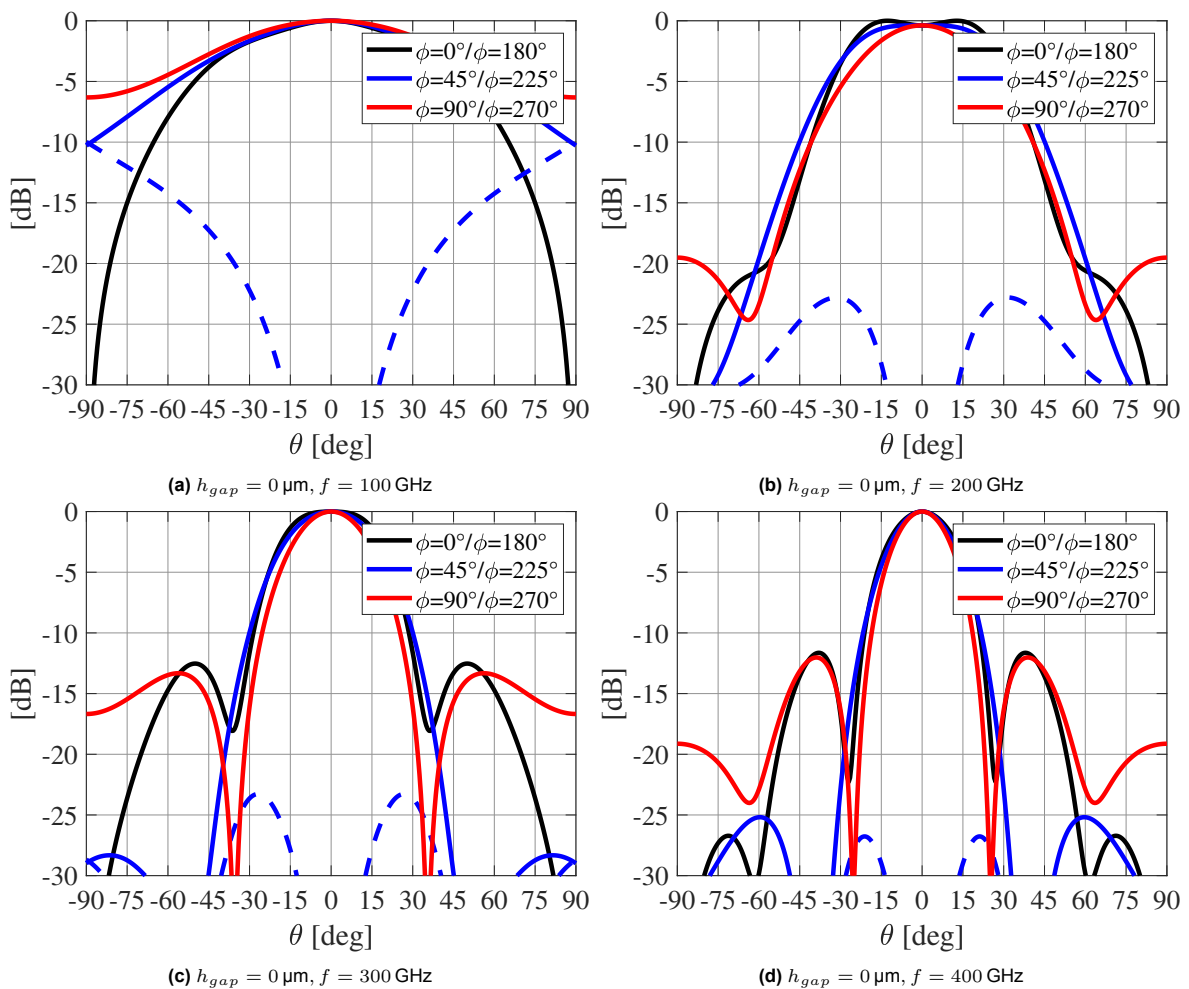
$$i_{rad}(t) = i_{impr}(t) - i_{gen}(t) \quad (\text{A.3})$$

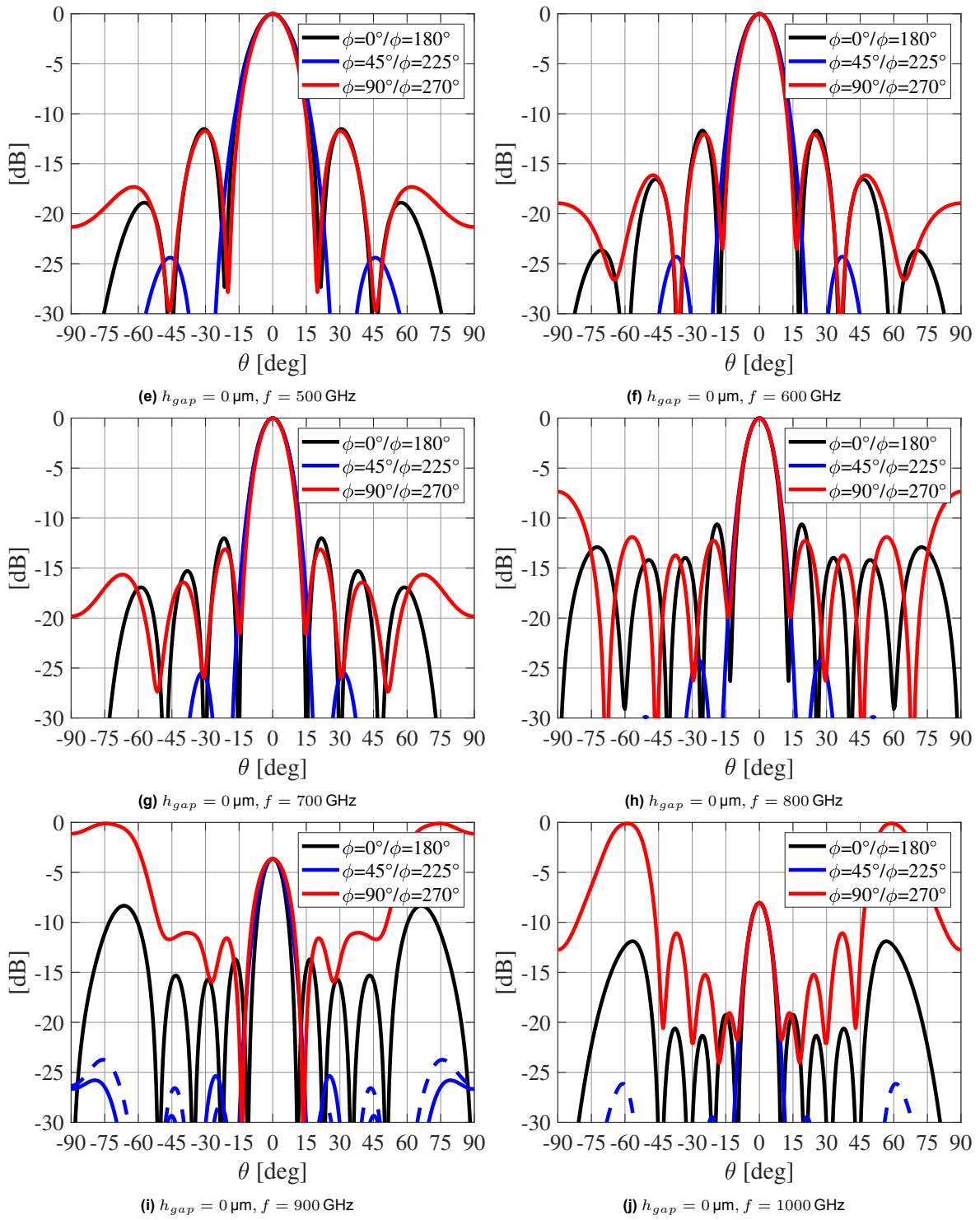
# B

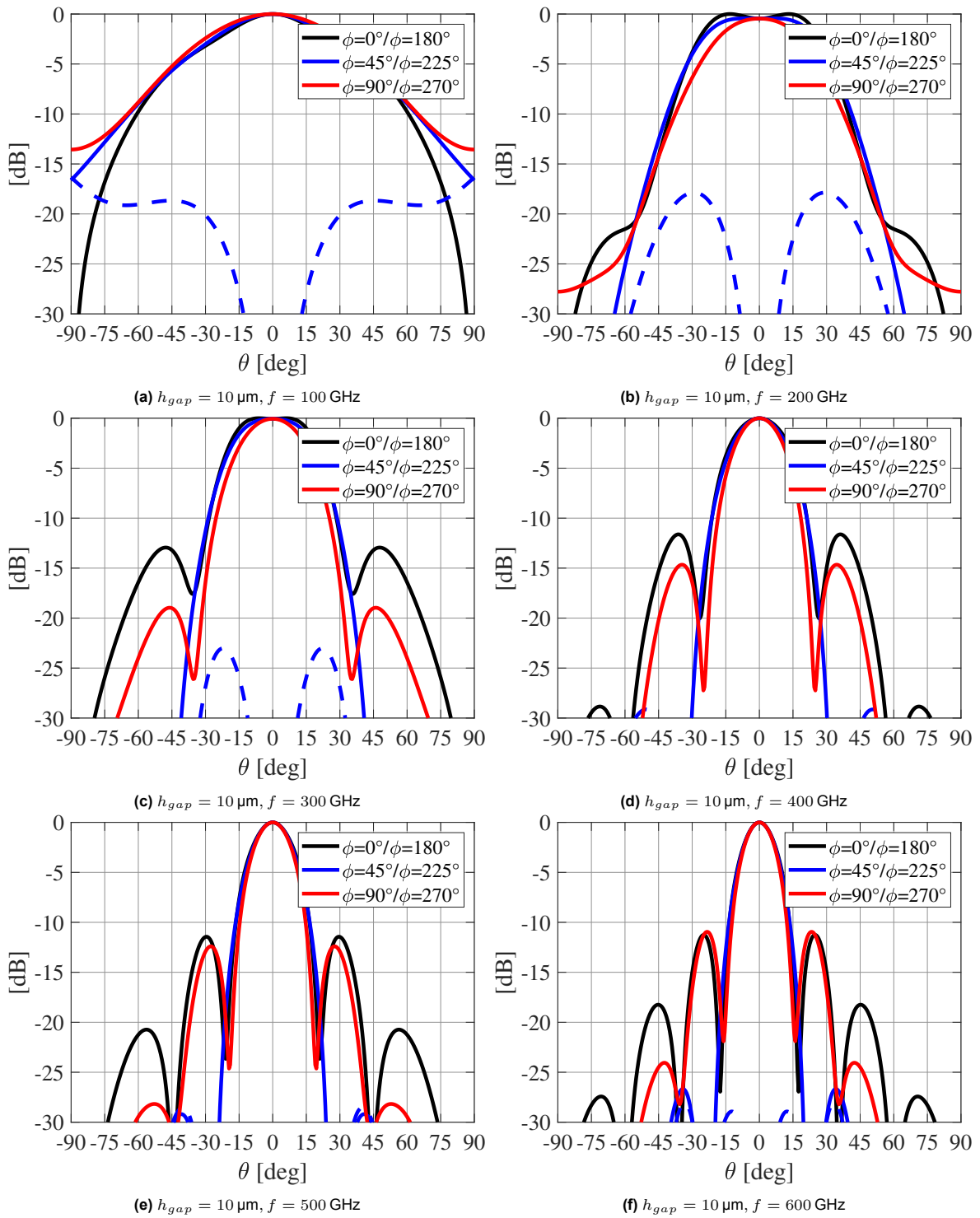
## Primary far-fields of the array inside silicon.

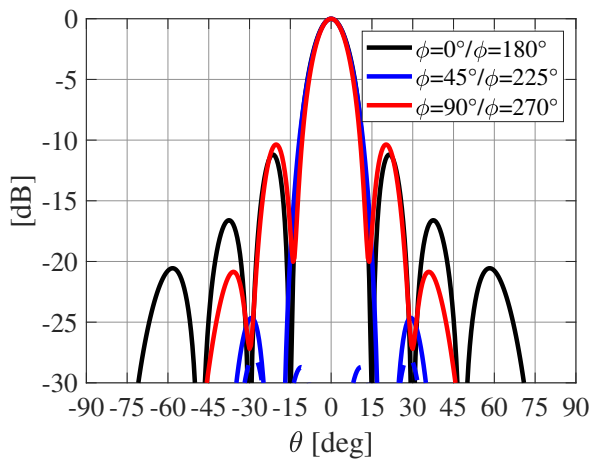
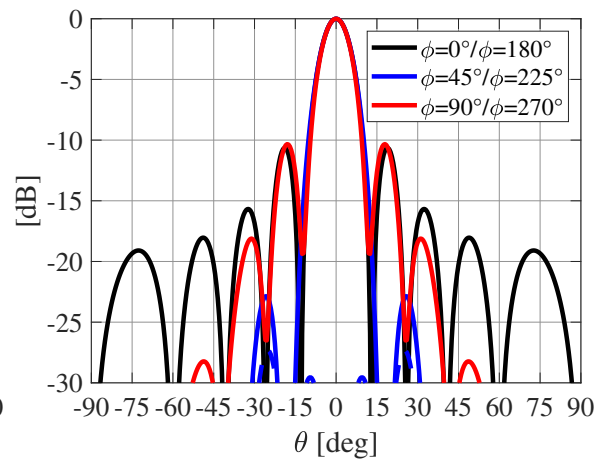
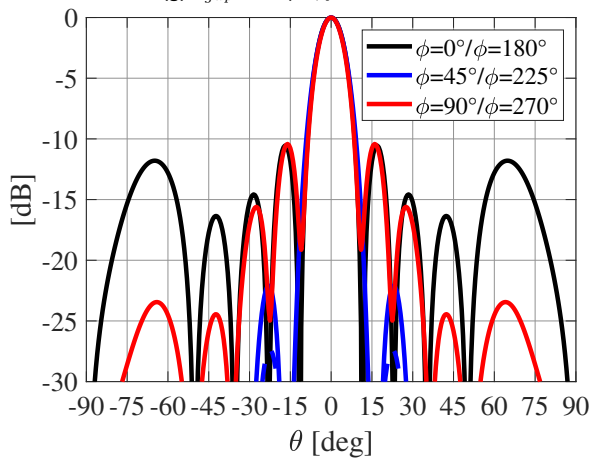
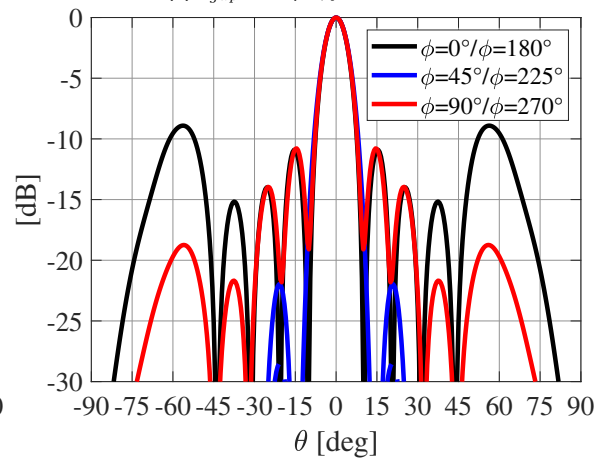
### B.1. Primary far-field patterns

#### B.1.1. Amplitude patterns $h_{gap} = 0 \mu m$

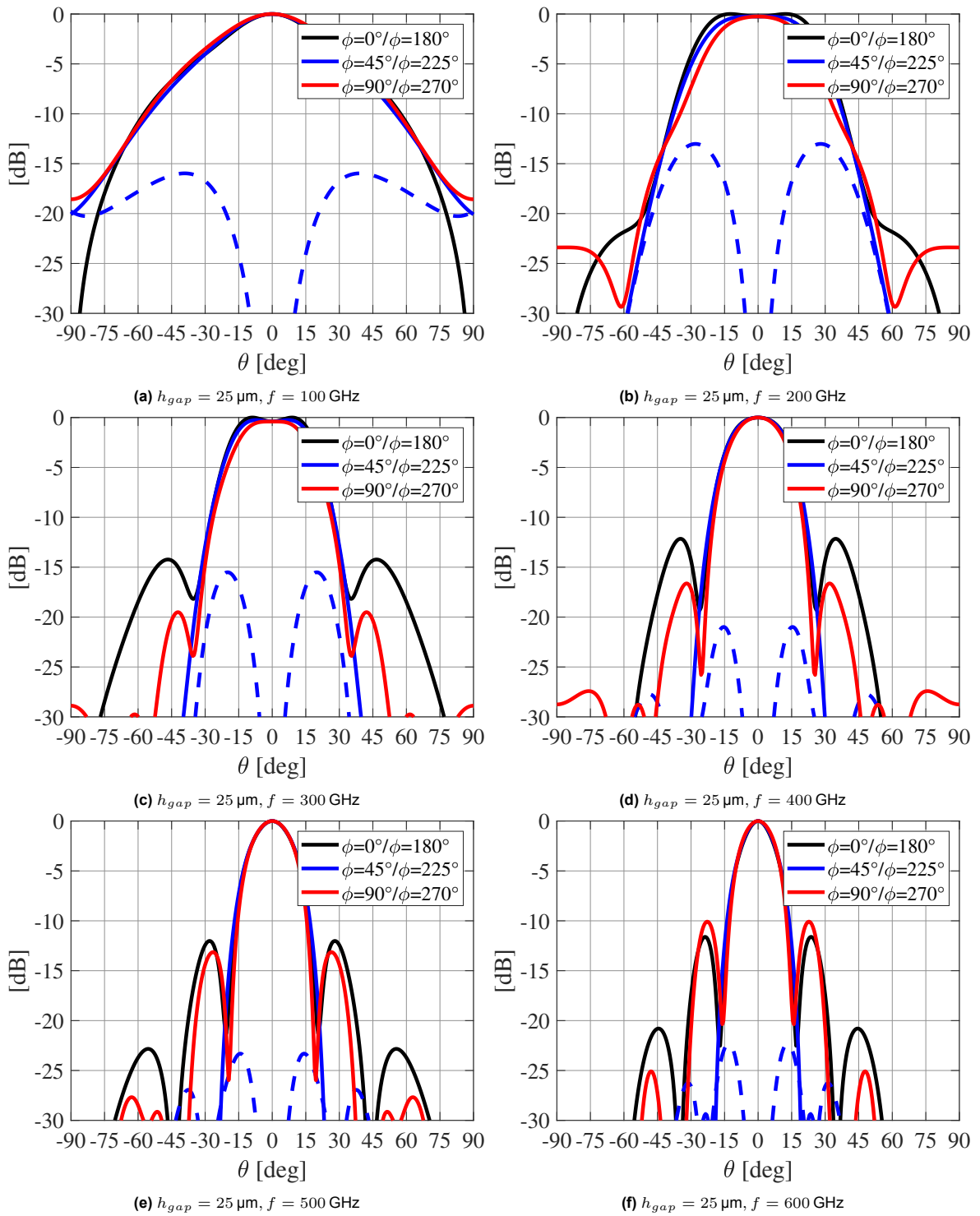


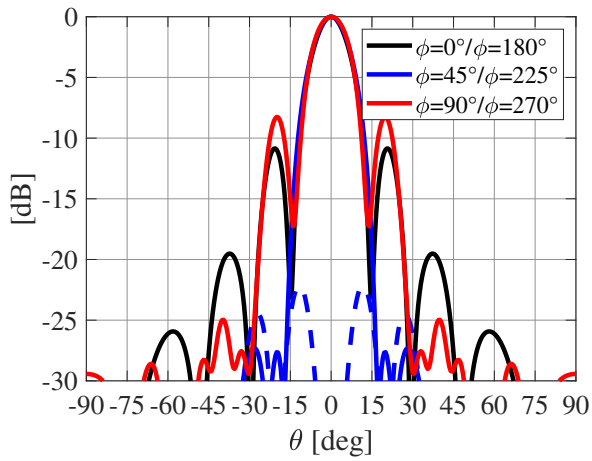
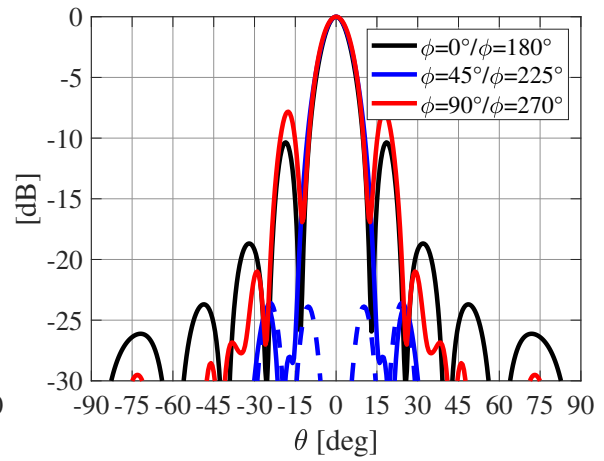
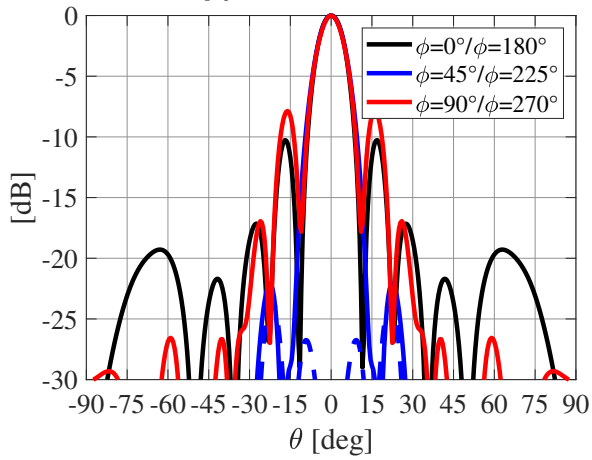
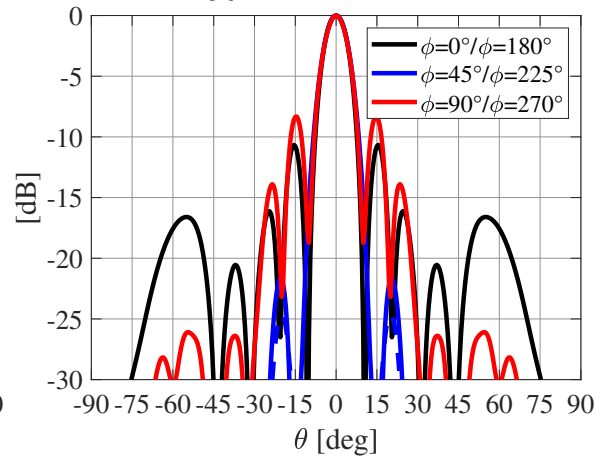


B.1.2. Amplitude patterns  $h_{gap} = 10\mu m$ 

(g)  $h_{gap} = 10 \mu\text{m}$ ,  $f = 700 \text{ GHz}$ (h)  $h_{gap} = 10 \mu\text{m}$ ,  $f = 800 \text{ GHz}$ (i)  $h_{gap} = 10 \mu\text{m}$ ,  $f = 900 \text{ GHz}$ (j)  $h_{gap} = 10 \mu\text{m}$ ,  $f = 1000 \text{ GHz}$

**B.1.3. Amplitude patterns  $h_{gap} = 25\mu m$**



(g)  $h_{gap} = 25 \mu\text{m}$ ,  $f = 700 \text{ GHz}$ (h)  $h_{gap} = 25 \mu\text{m}$ ,  $f = 800 \text{ GHz}$ (i)  $h_{gap} = 25 \mu\text{m}$ ,  $f = 900 \text{ GHz}$ (j)  $h_{gap} = 25 \mu\text{m}$ ,  $f = 1000 \text{ GHz}$

## B.2. Phase error losses

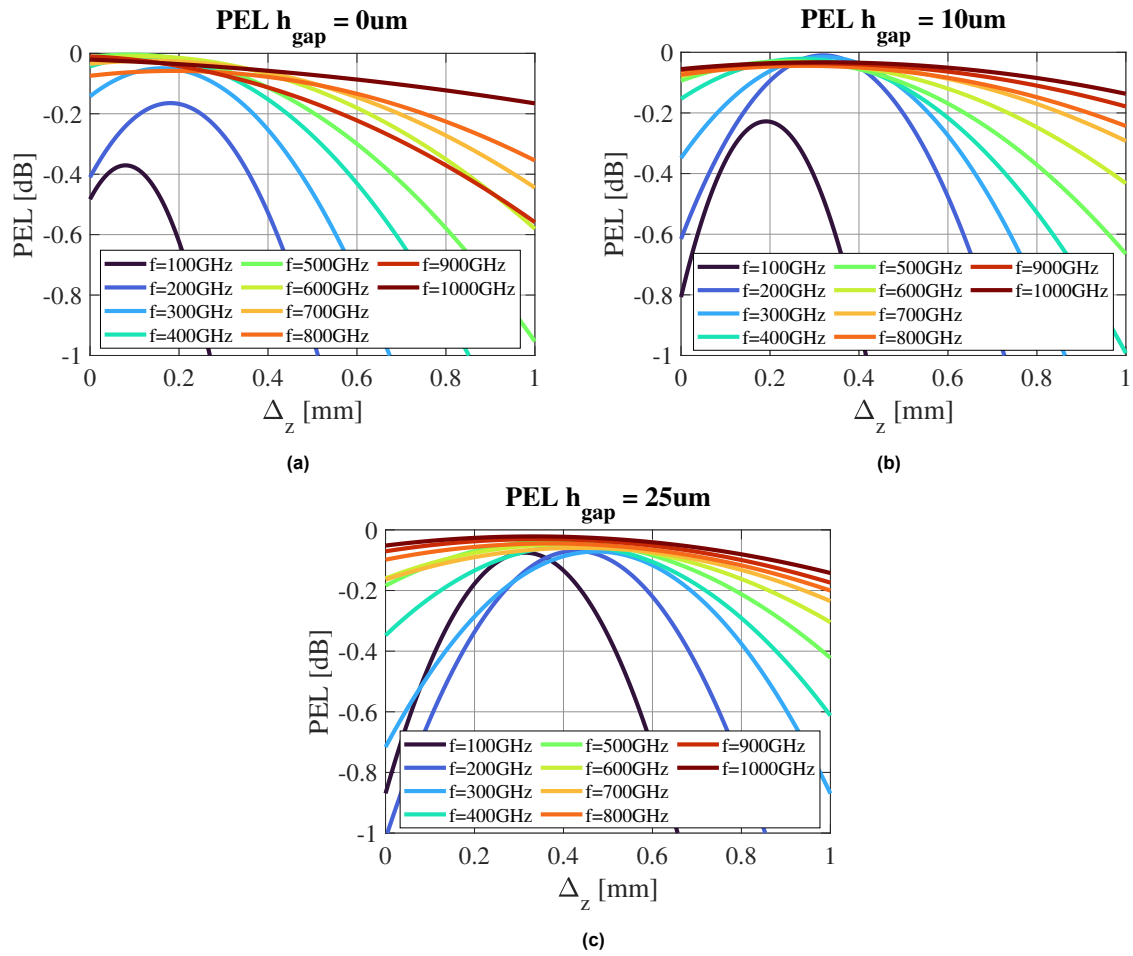
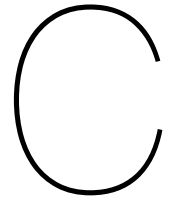


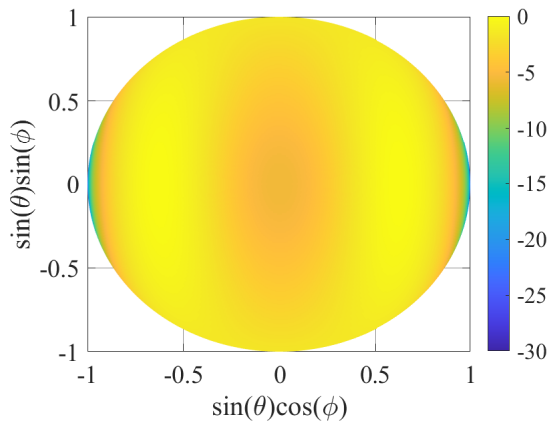
**Figure B.4:** PEL evaluated for different  $\Delta_z$  of the far-fields inside silicon, for (a)  $h_{gap} = 0\text{ um}$ , (b)  $h_{gap} = 10\text{ um}$ , (c)  $h_{gap} = 25\text{ um}$ .



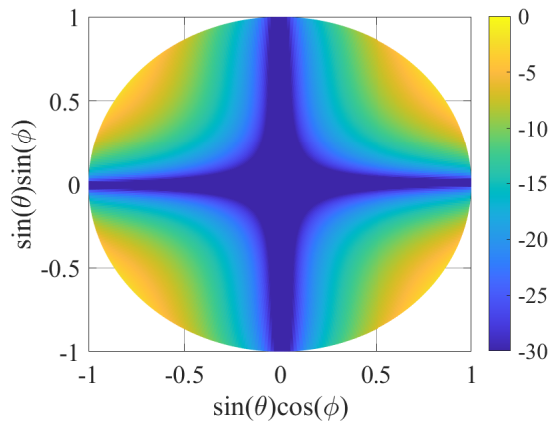
# Center Embedded Element Pattern

## C.1. Far-field embedded pattern of the center element

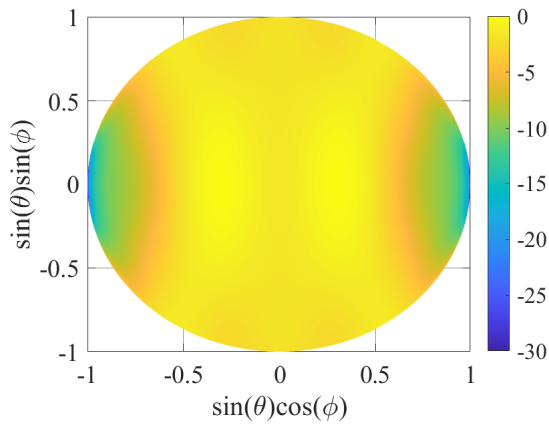
### C.1.1. $h_{gap} = 0\mu m$



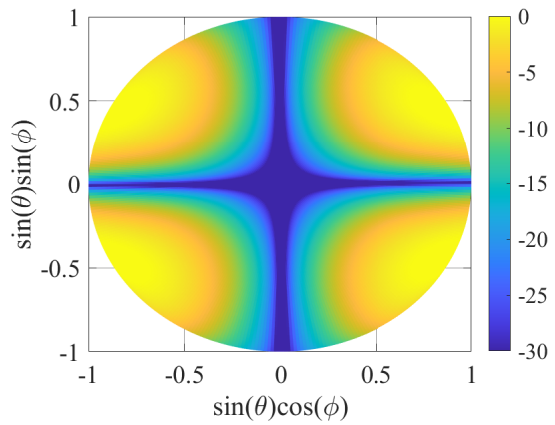
(a) co-polar component, 100 GHz



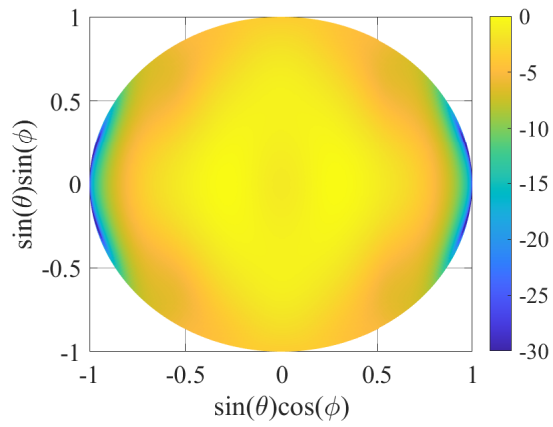
(b) cross-polar component, 100 GHz



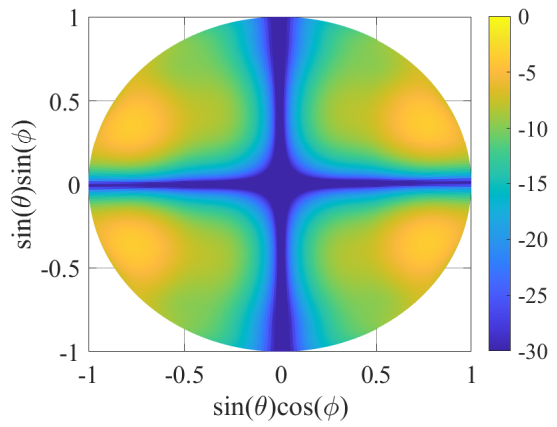
(c) co-polar component, 200 GHz



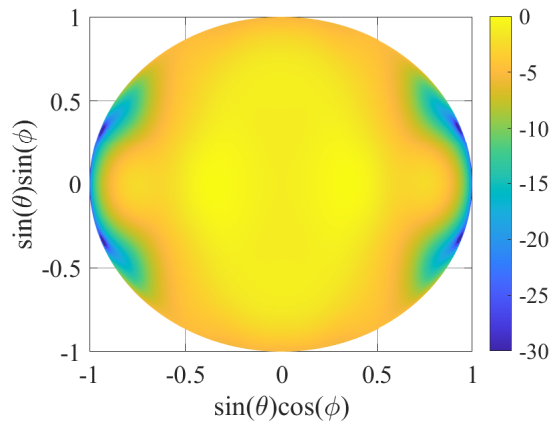
(d) cross-polar component, 200 GHz



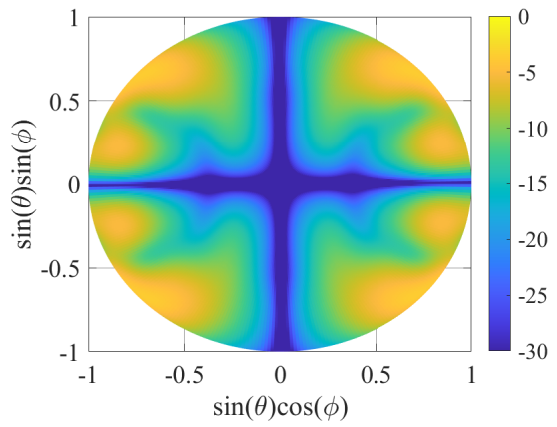
(e) co-polar component, 300 GHz



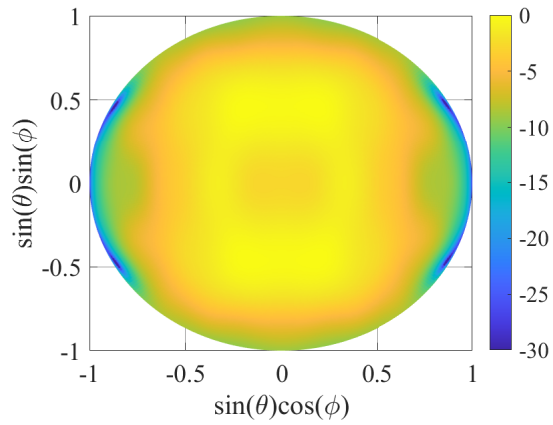
(f) cross-polar component, 300 GHz



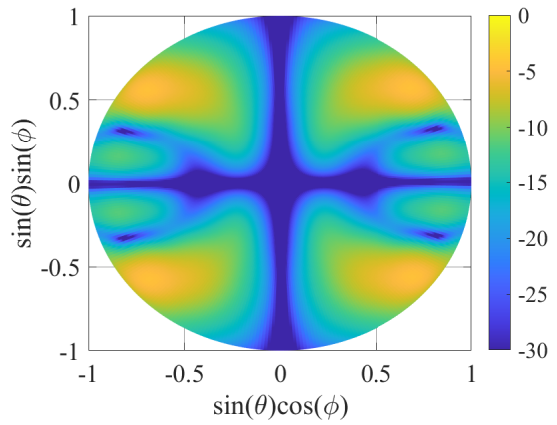
(g) co-polar component, 400 GHz



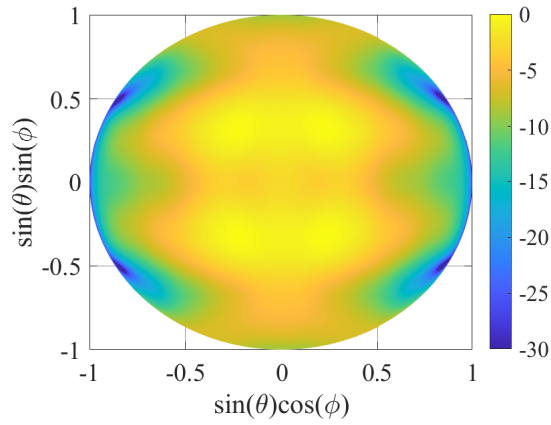
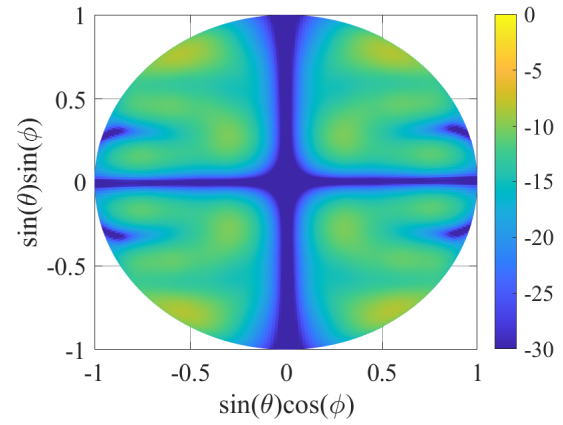
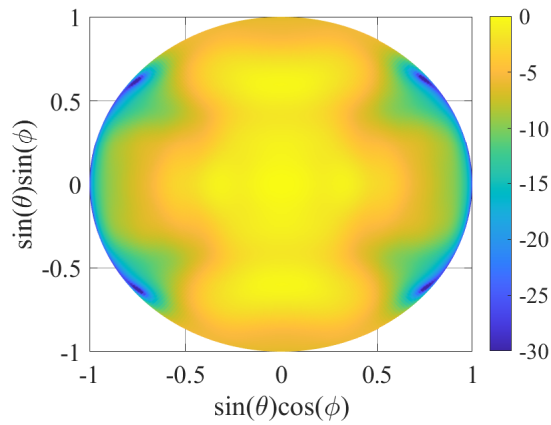
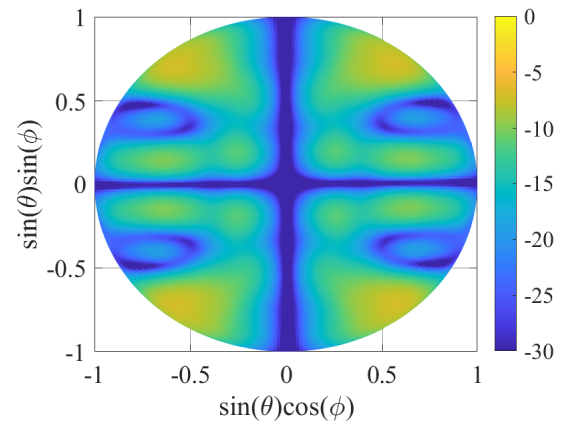
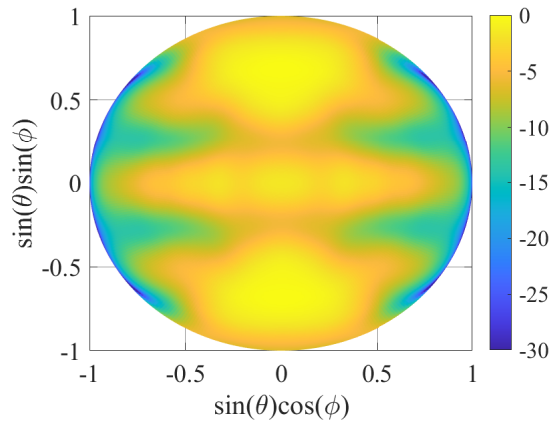
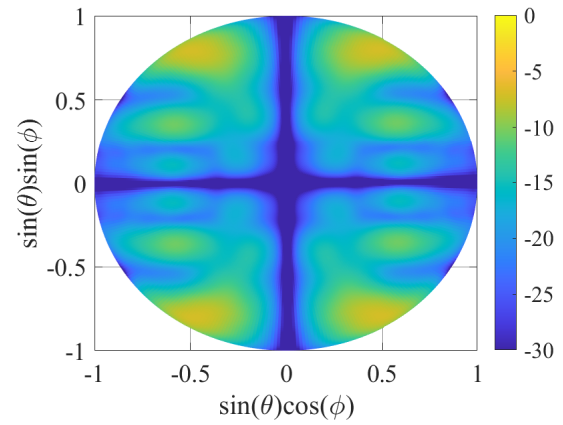
(h) cross-polar component, 400 GHz

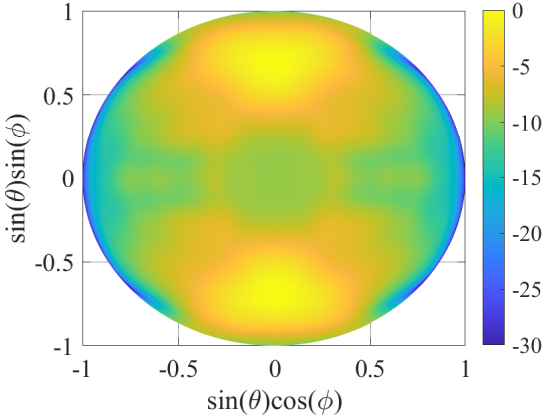


(i) co-polar component, 500 GHz

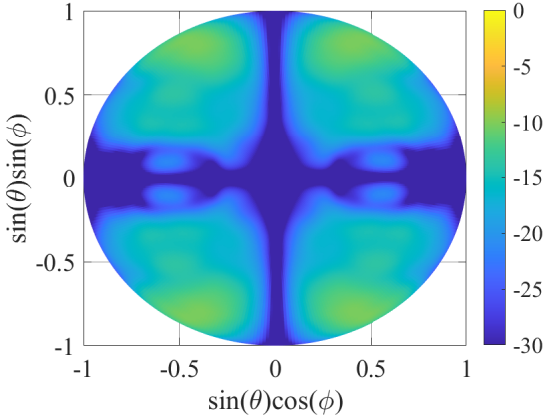


(j) cross-polar component, 500 GHz

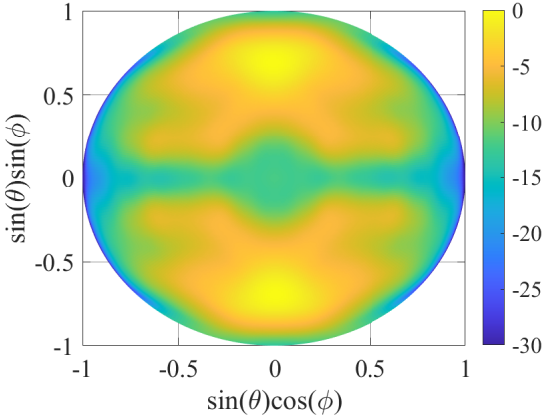
**(k)** co-polar component, 600 GHz**(l)** cross-polar component, 600 GHz**(m)** co-polar component, 700 GHz**(n)** cross-polar component, 700 GHz**(o)** co-polar component, 800 GHz**(p)** cross-polar component, 800 GHz



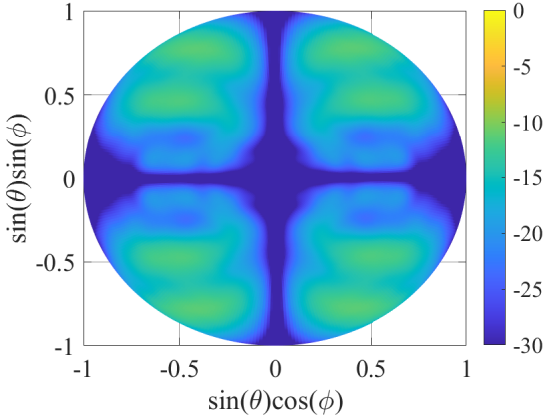
(q) co-polar component, 900 GHz



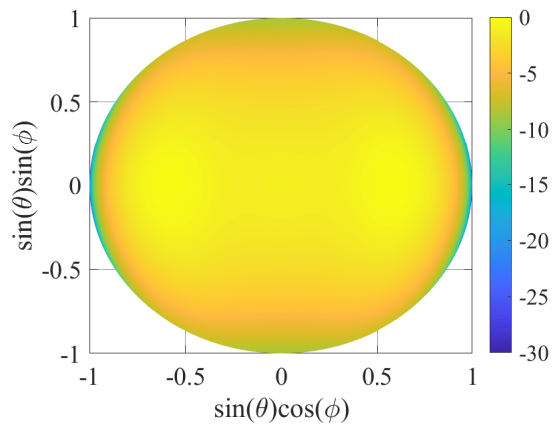
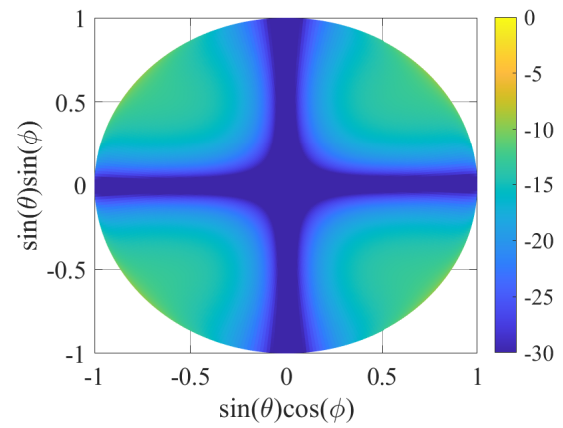
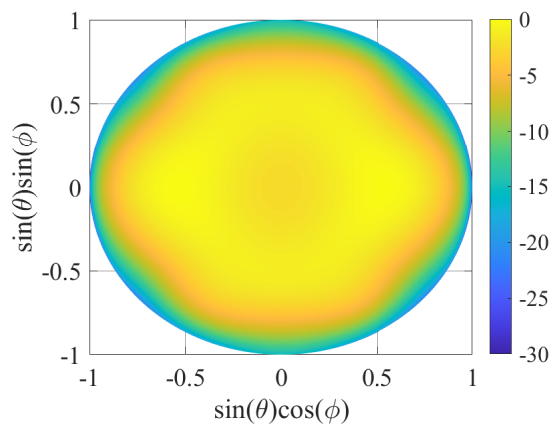
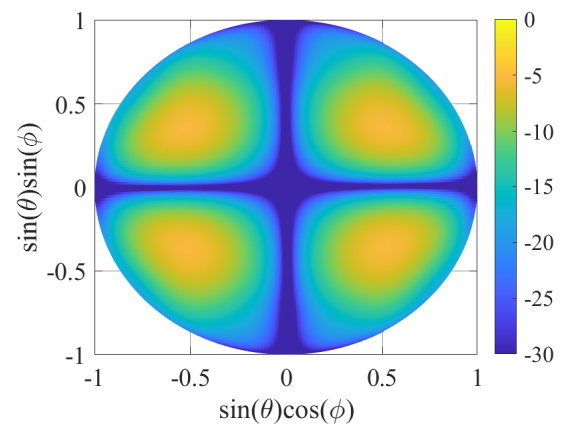
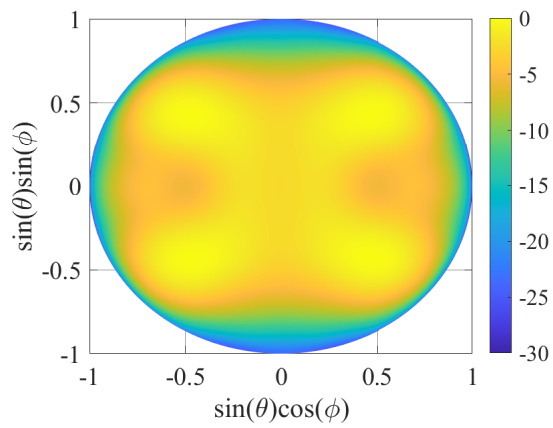
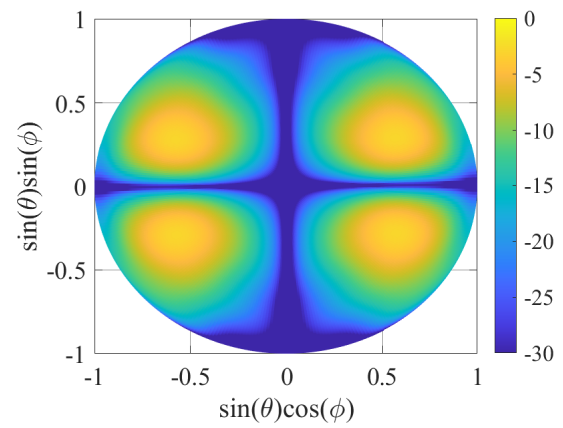
(r) cross-polar component, 900 GHz

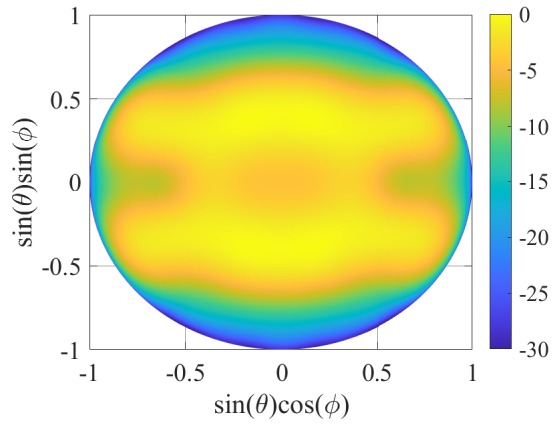
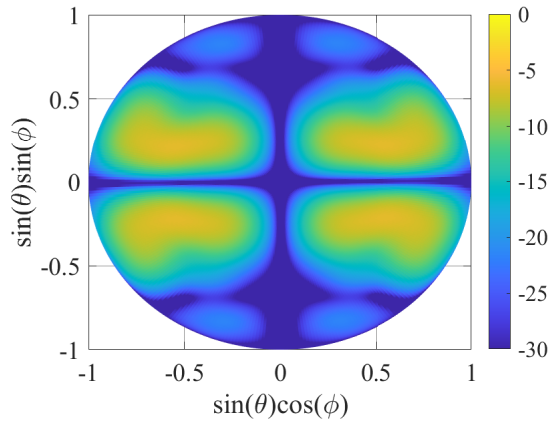
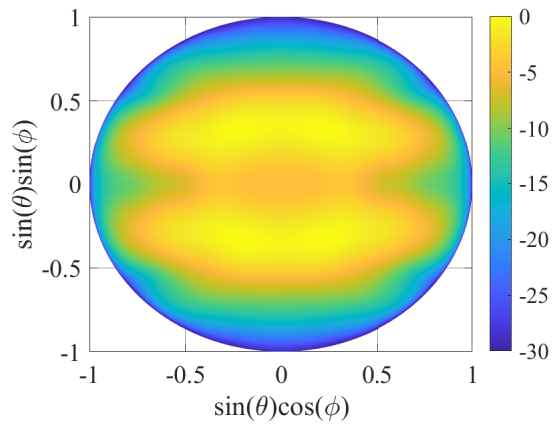
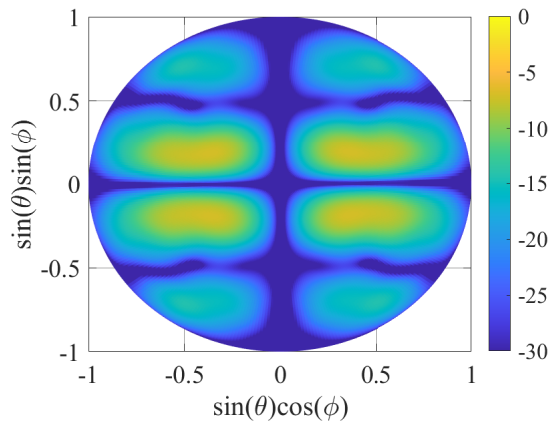
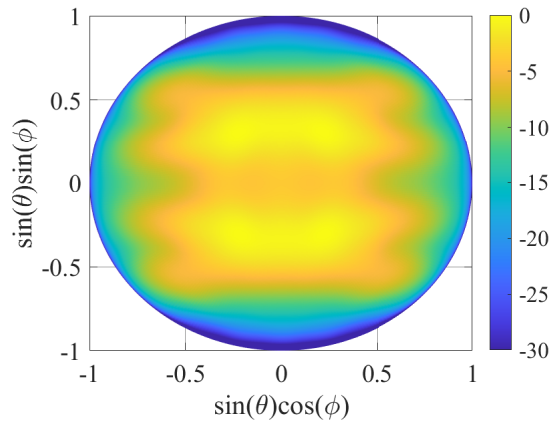
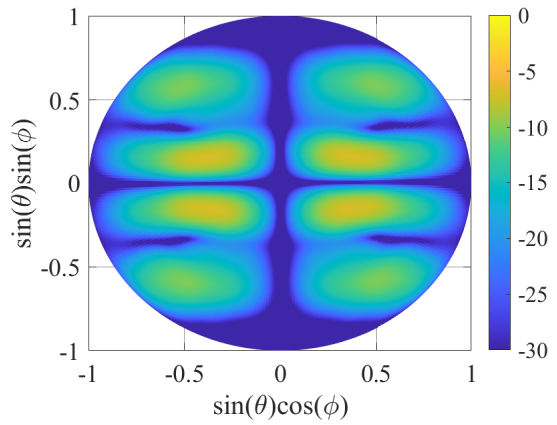


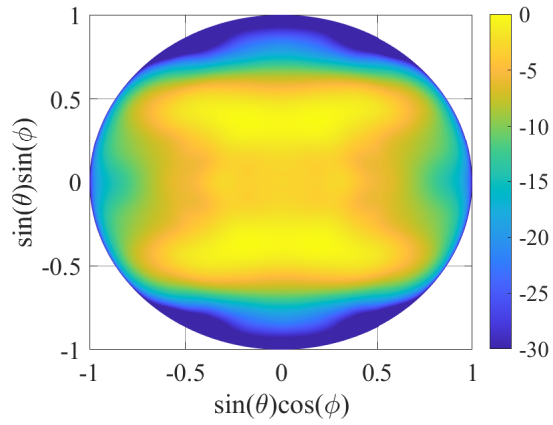
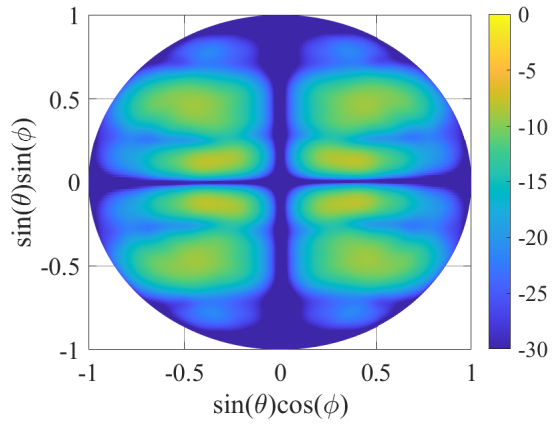
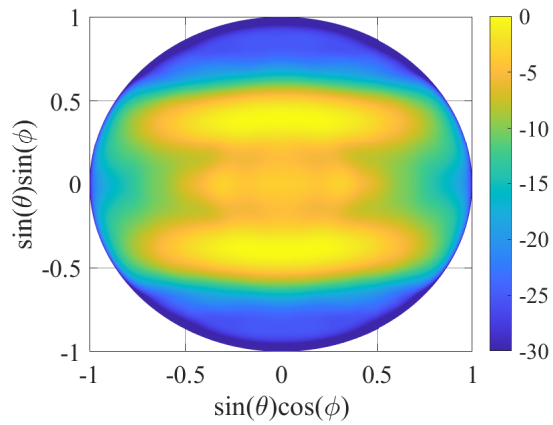
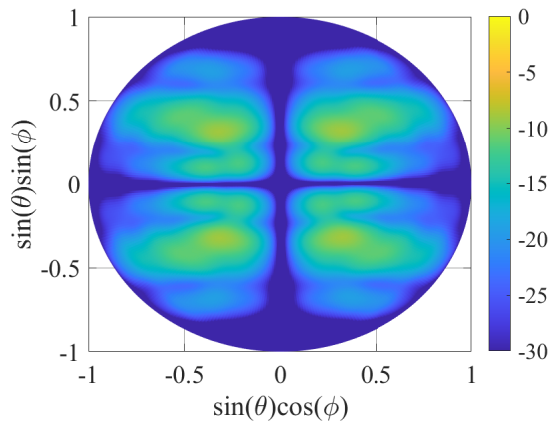
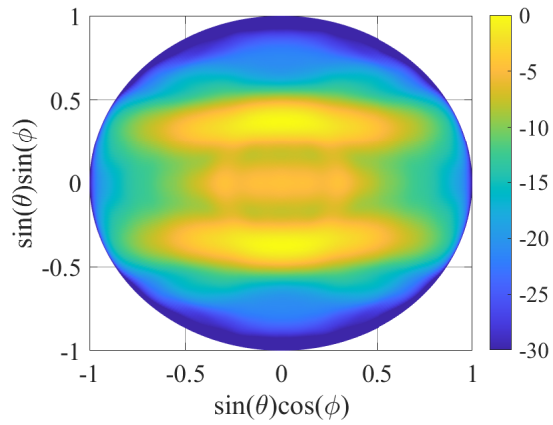
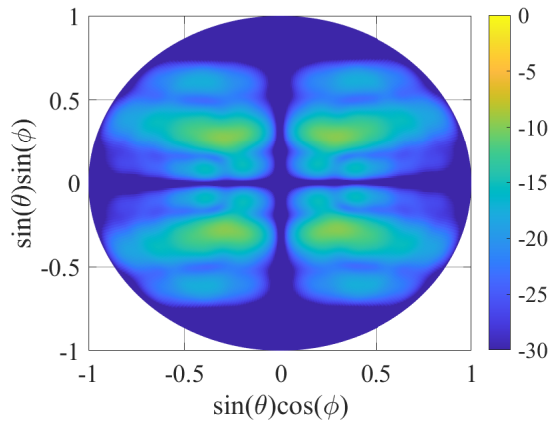
(s) co-polar component, 1000 GHz

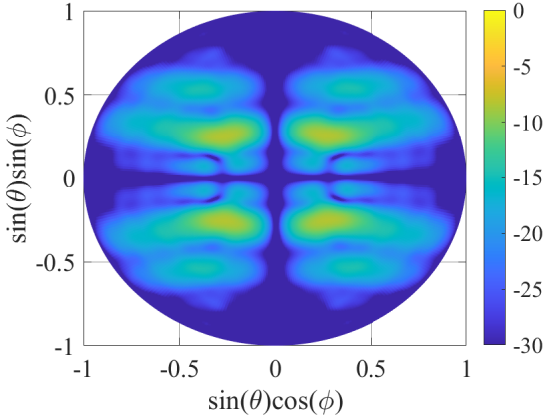
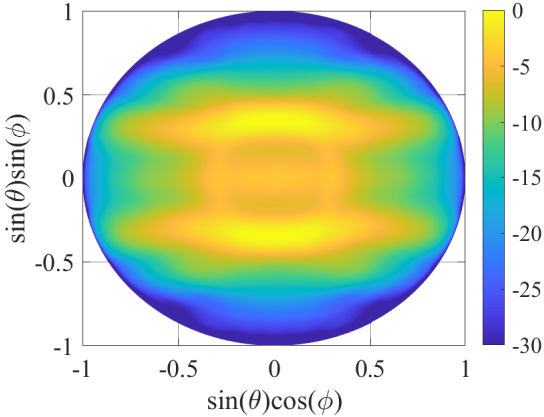


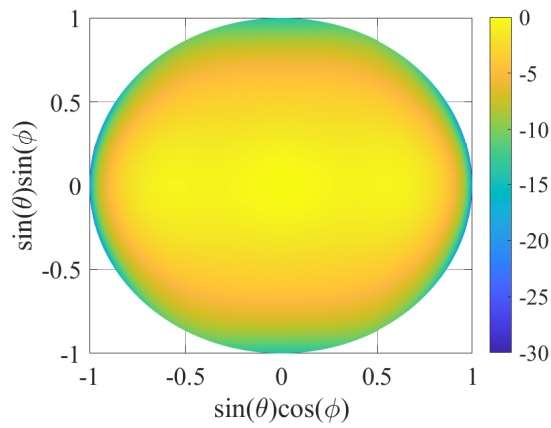
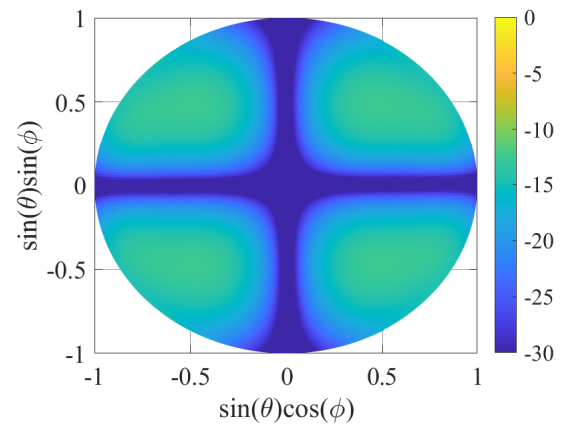
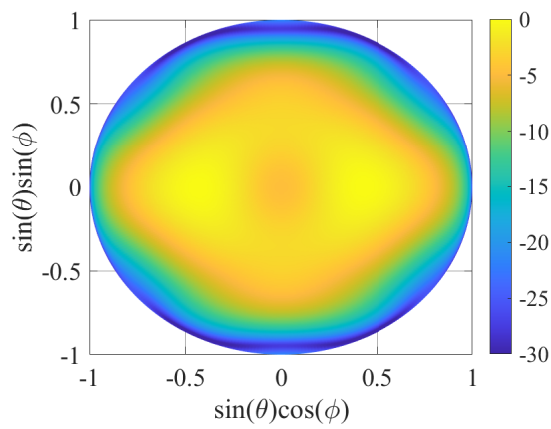
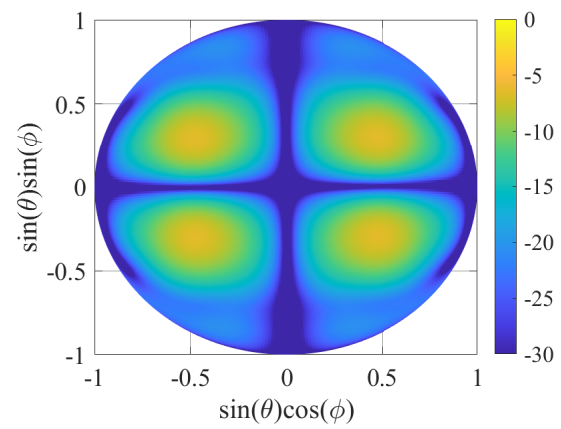
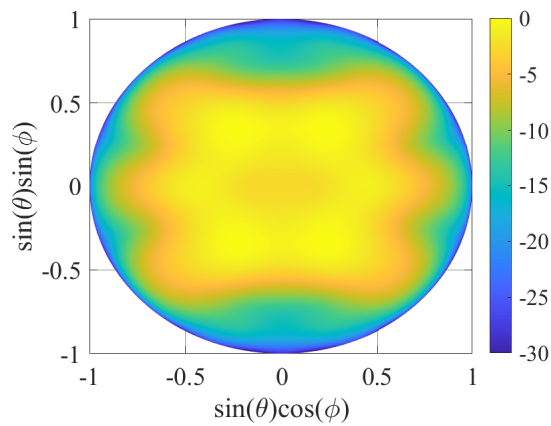
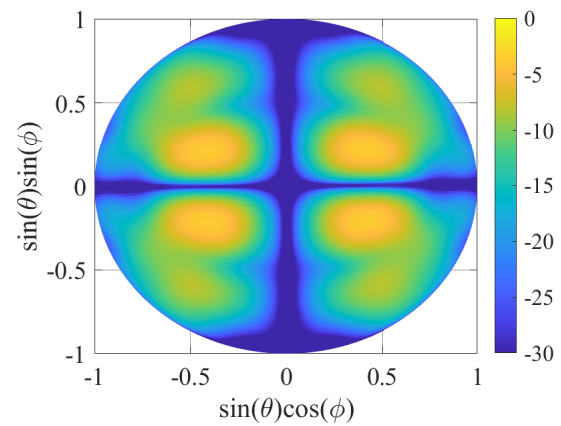
(t) cross-polar component, 1000 GHz

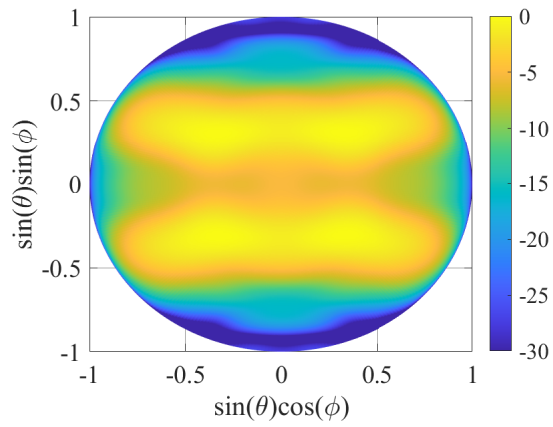
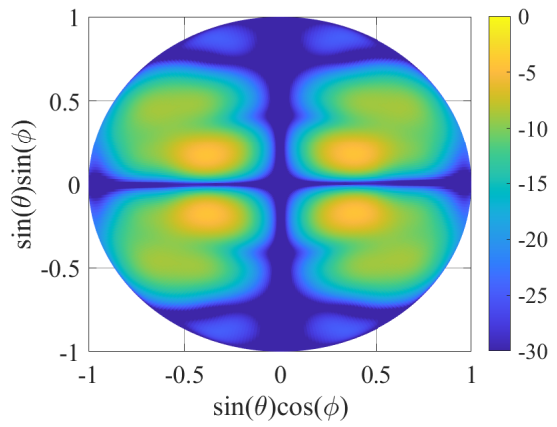
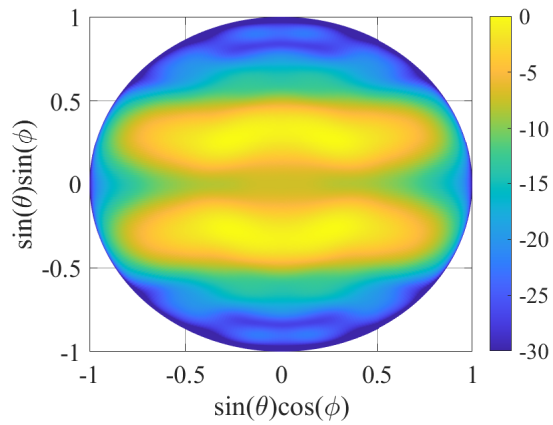
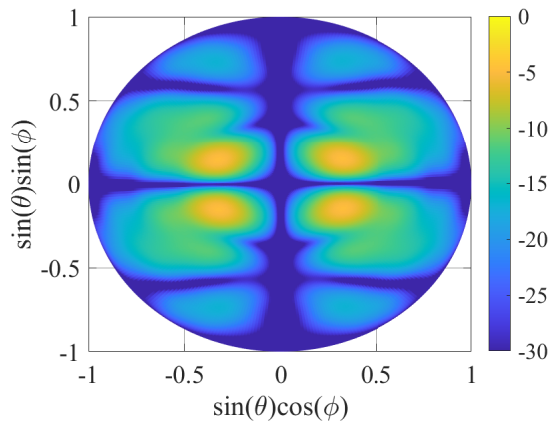
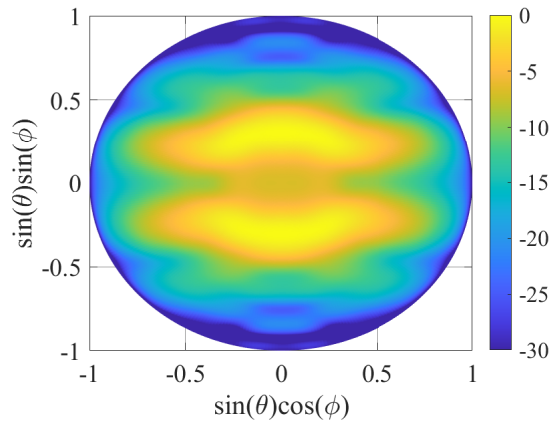
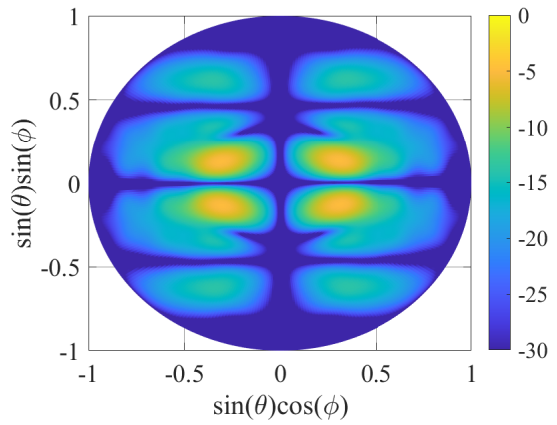
**C.1.2.**  $h_{gap} = 10\mu m$ **(a)** co-polar component, 100 GHz**(b)** cross-polar component, 100 GHz**(c)** co-polar component, 200 GHz**(d)** cross-polar component, 200 GHz**(e)** co-polar component, 300 GHz**(f)** cross-polar component, 300 GHz

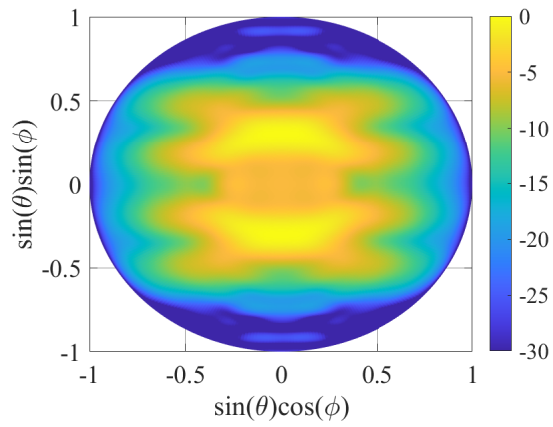
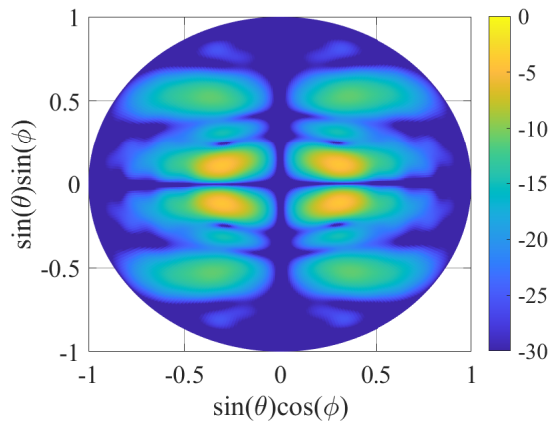
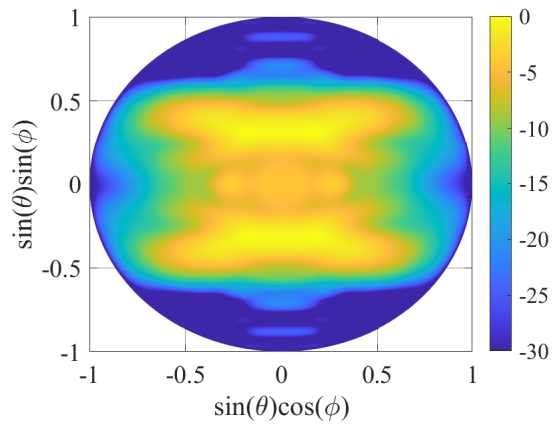
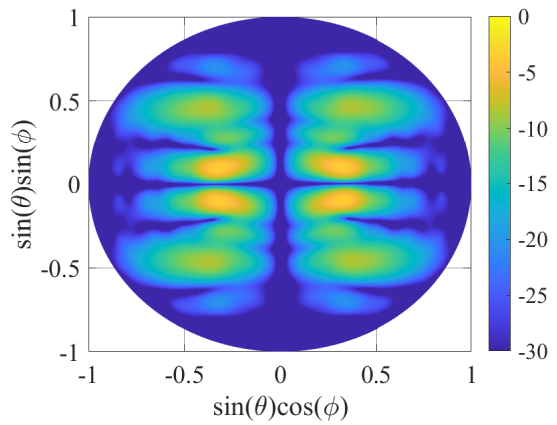
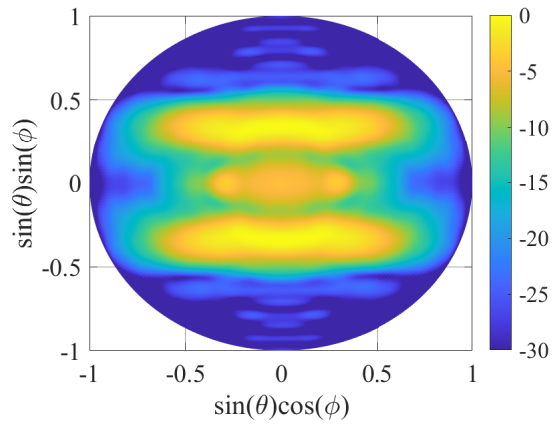
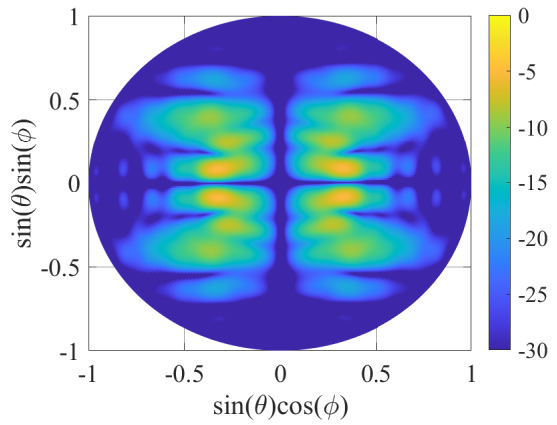
**(g)** co-polar component, 400 GHz**(h)** cross-polar component, 400 GHz**(i)** co-polar component, 500 GHz**(j)** cross-polar component, 500 GHz**(k)** co-polar component, 600 GHz**(l)** cross-polar component, 600 GHz

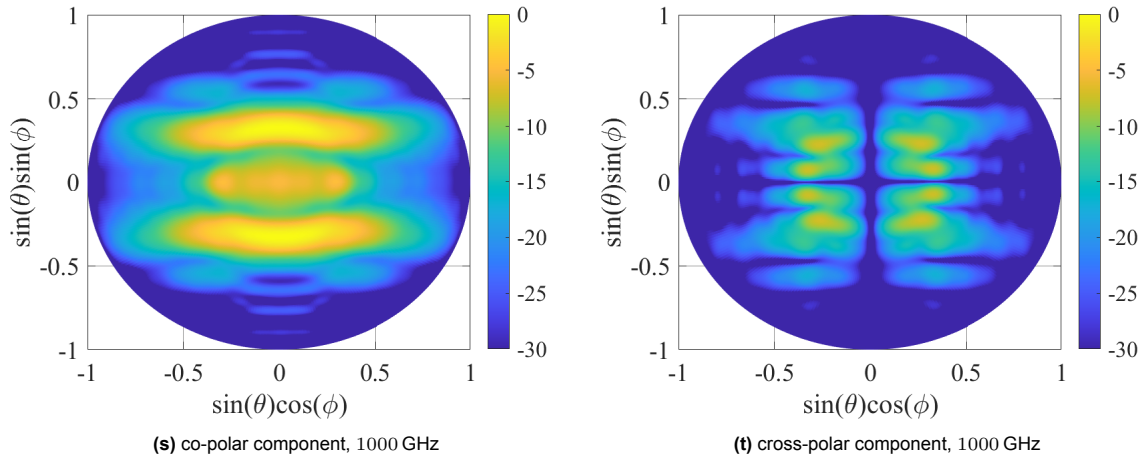
**(m)** co-polar component, 700 GHz**(n)** cross-polar component, 700 GHz**(o)** co-polar component, 800 GHz**(p)** cross-polar component, 800 GHz**(q)** co-polar component, 900 GHz**(r)** cross-polar component, 900 GHz



**C.1.3.**  $h_{gap} = 25\mu m$ **(a)** co-polar component, 100 GHz**(b)** cross-polar component, 100 GHz**(c)** co-polar component, 200 GHz**(d)** cross-polar component, 200 GHz**(e)** co-polar component, 300 GHz**(f)** cross-polar component, 300 GHz

**(g)** co-polar component, 400 GHz**(h)** cross-polar component, 400 GHz**(i)** co-polar component, 500 GHz**(j)** cross-polar component, 500 GHz**(k)** co-polar component, 600 GHz**(l)** cross-polar component, 600 GHz

**(m)** co-polar component, 700 GHz**(n)** cross-polar component, 700 GHz**(o)** co-polar component, 800 GHz**(p)** cross-polar component, 800 GHz**(q)** co-polar component, 900 GHz**(r)** cross-polar component, 900 GHz



### C.2. Phase error losses

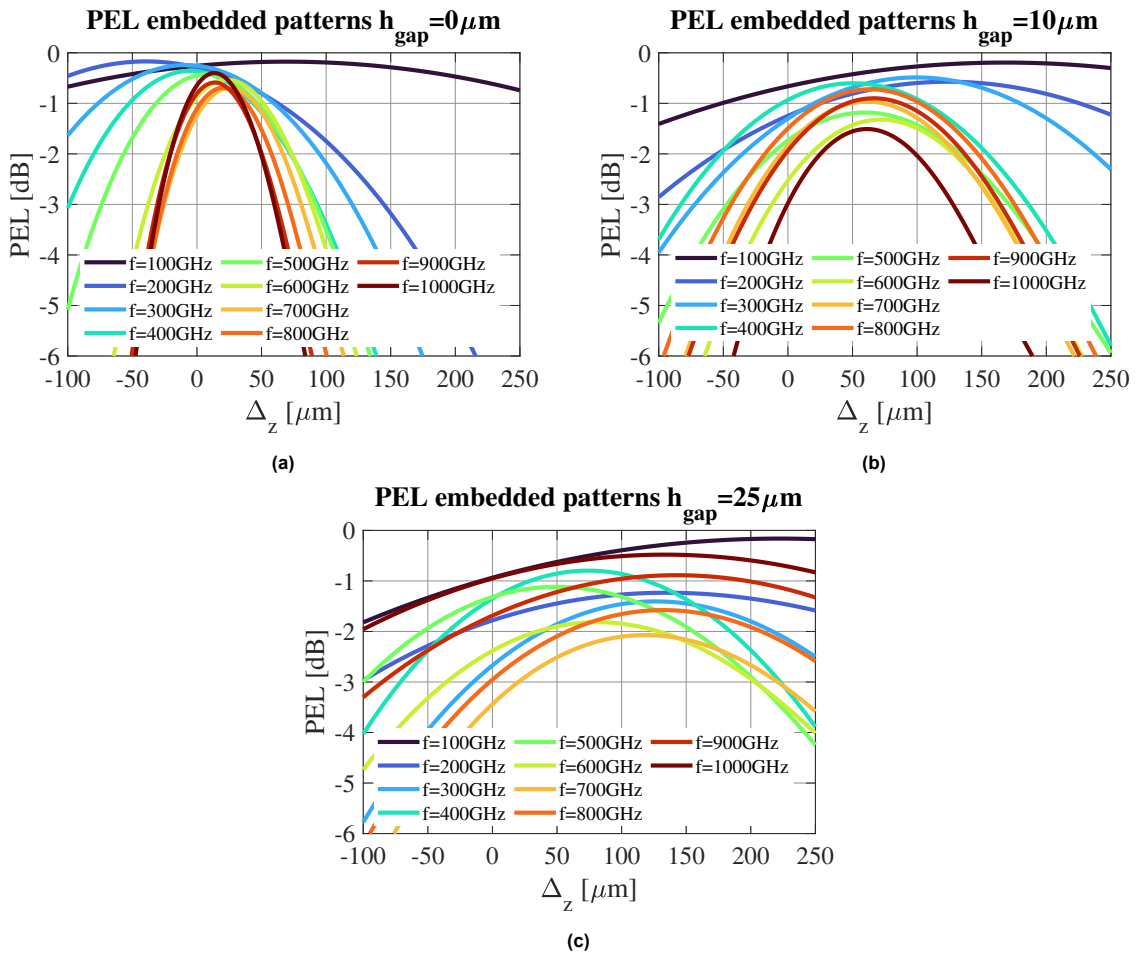
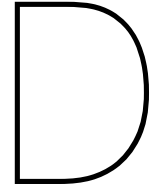


**Figure C.4:** PEL evaluated for different  $\Delta_z$  of the embedded center element patterns silicon, for (a)  $h_{gap} = 0 \mu\text{m}$ , (b)  $h_{gap} = 10 \mu\text{m}$ , (c)  $h_{gap} = 25 \mu\text{m}$ .

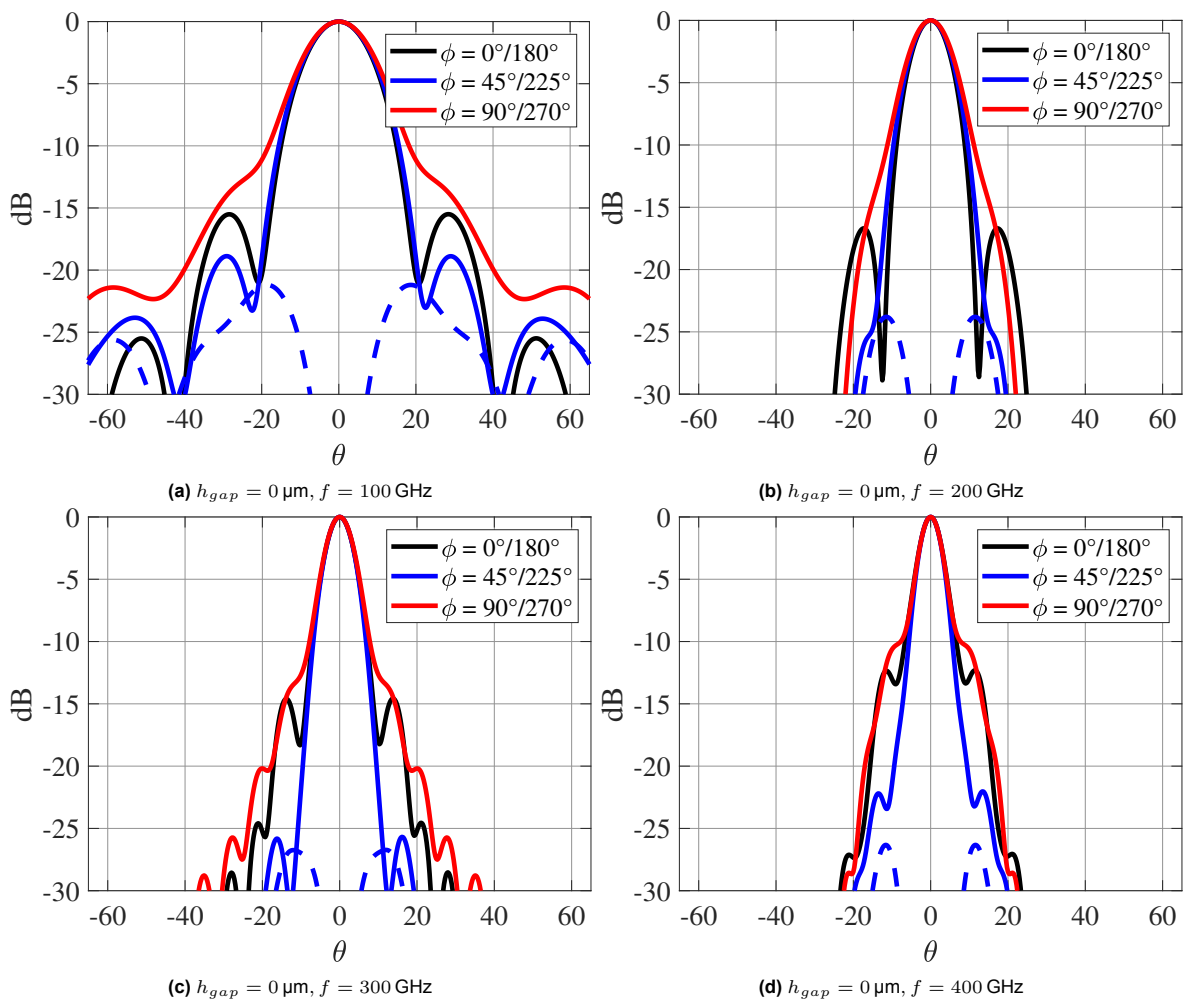


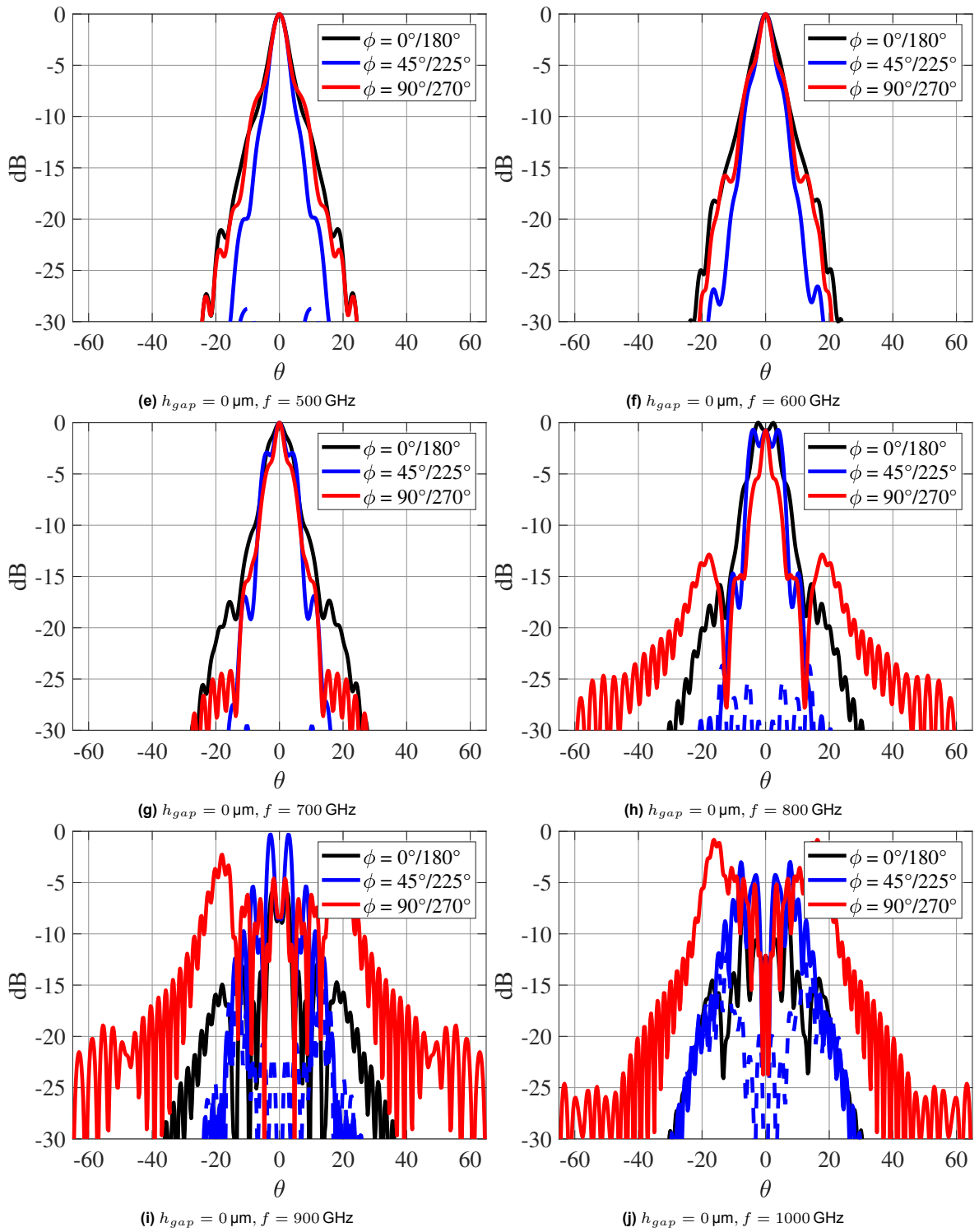
# Secondary fields fabricated PCCAs

## D.1. Secondary far-field patterns

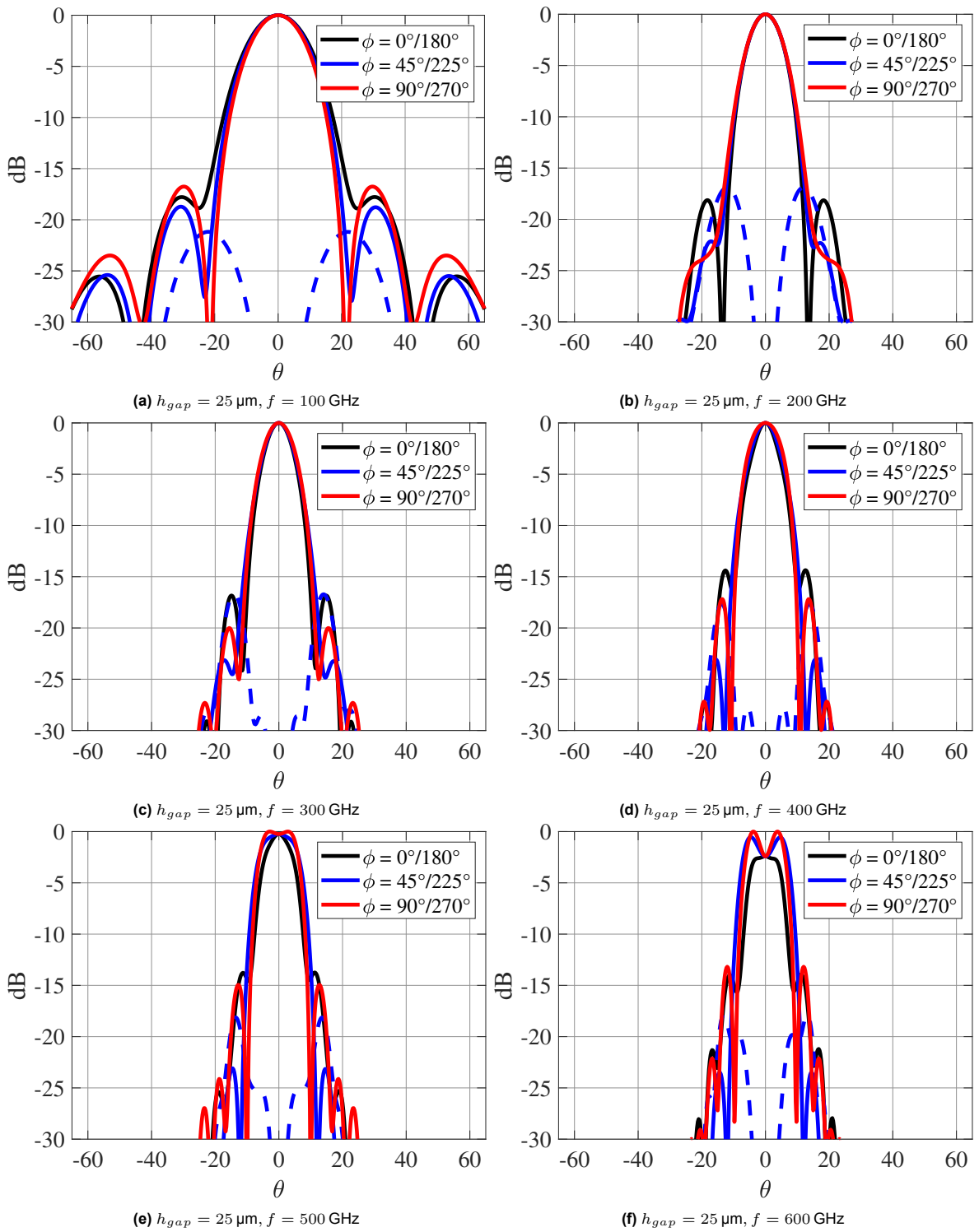
In this section, the amplitude of the secondary fields radiated by the fabricated PCCA's is shown.

### D.1.1. Amplitude patterns $h_{gap} = 0 \mu m$





**Figure D.1:** Normalized secondary far-field amplitude patterns of the fabricated PCCA geometry with  $h_{gap} = 0 \mu\text{m}$ . Note that the co-polarized components are indicated with solid lines, and the cross-polarized components are indicated with dashed lines.

D.1.2. Amplitude patterns  $h_{gap} = 25\mu m$ 

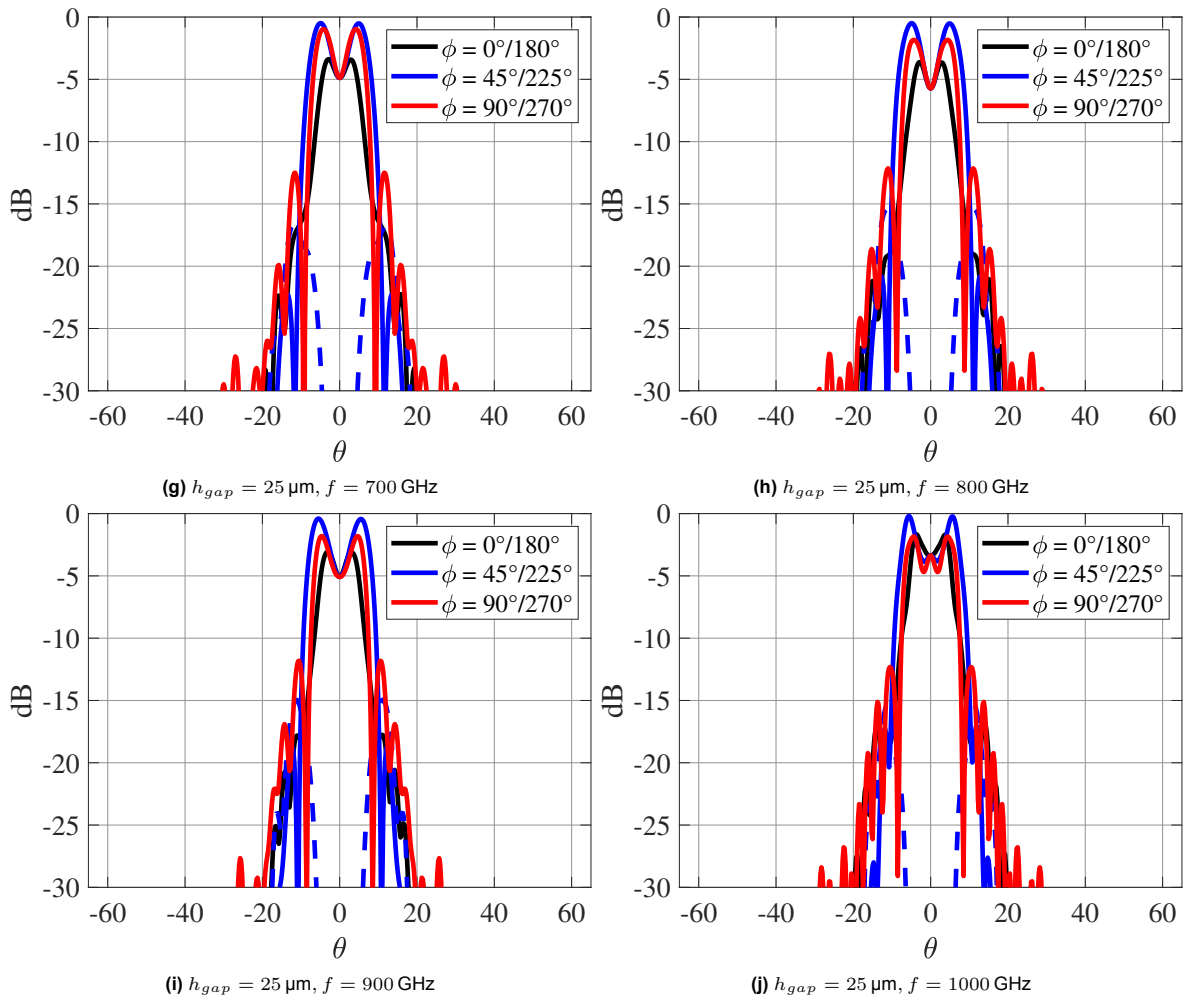


**Figure D.2:** Normalized secondary far-field amplitude patterns of the fabricated PCCA geometry with  $h_{gap} = 25 \mu\text{m}$ . Note that the co-polarized components are indicated with solid lines, and the cross-polarized components are indicated with dashed lines.

## D.2. Phase error losses

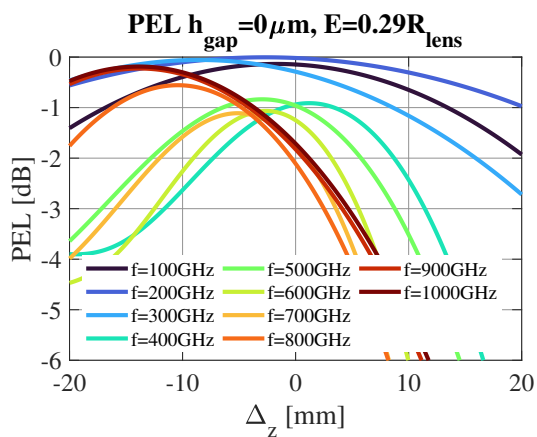


**Figure D.3:** PEL evaluated for different  $\Delta_z$  of the secondary fields, for  $h_{gap} = 0 \mu\text{m}$ .

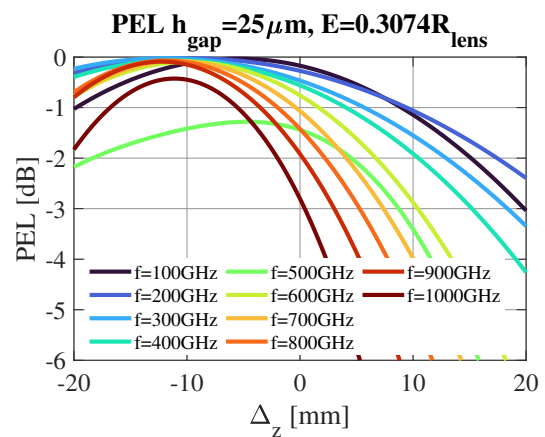
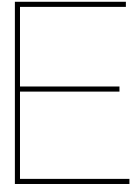


**Figure D.4:** PEL evaluated for different  $\Delta_z$  of the secondary fields, for  $h_{gap} = 25 \mu\text{m}$ .

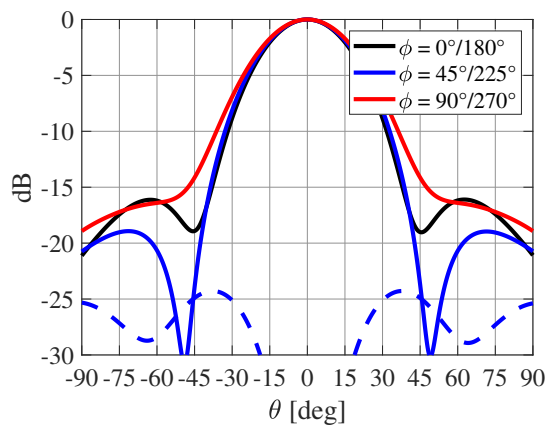


# Secondary fields redesigned PCCAs

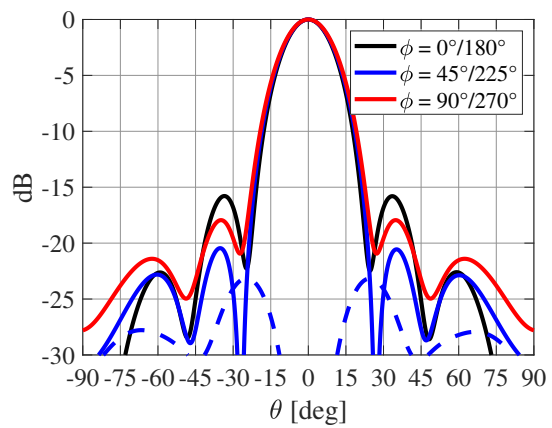
## E.1. Secondary far-field patterns

In this section, the amplitude of the secondary fields radiated by the redesigned PCCAs is shown.

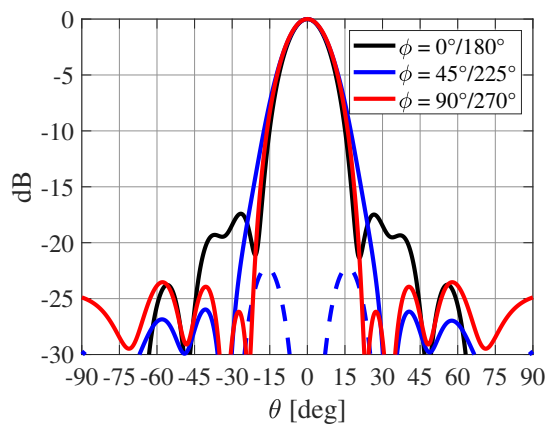
### E.1.1. Amplitude patterns $h_{gap} = 0 \mu m$



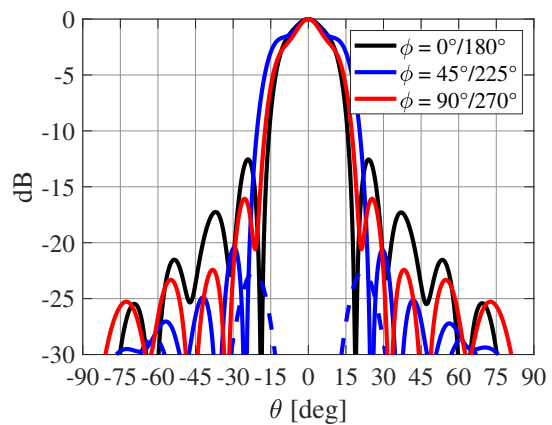
(a)  $h_{gap} = 0 \mu m, f = 100 \text{ GHz}$



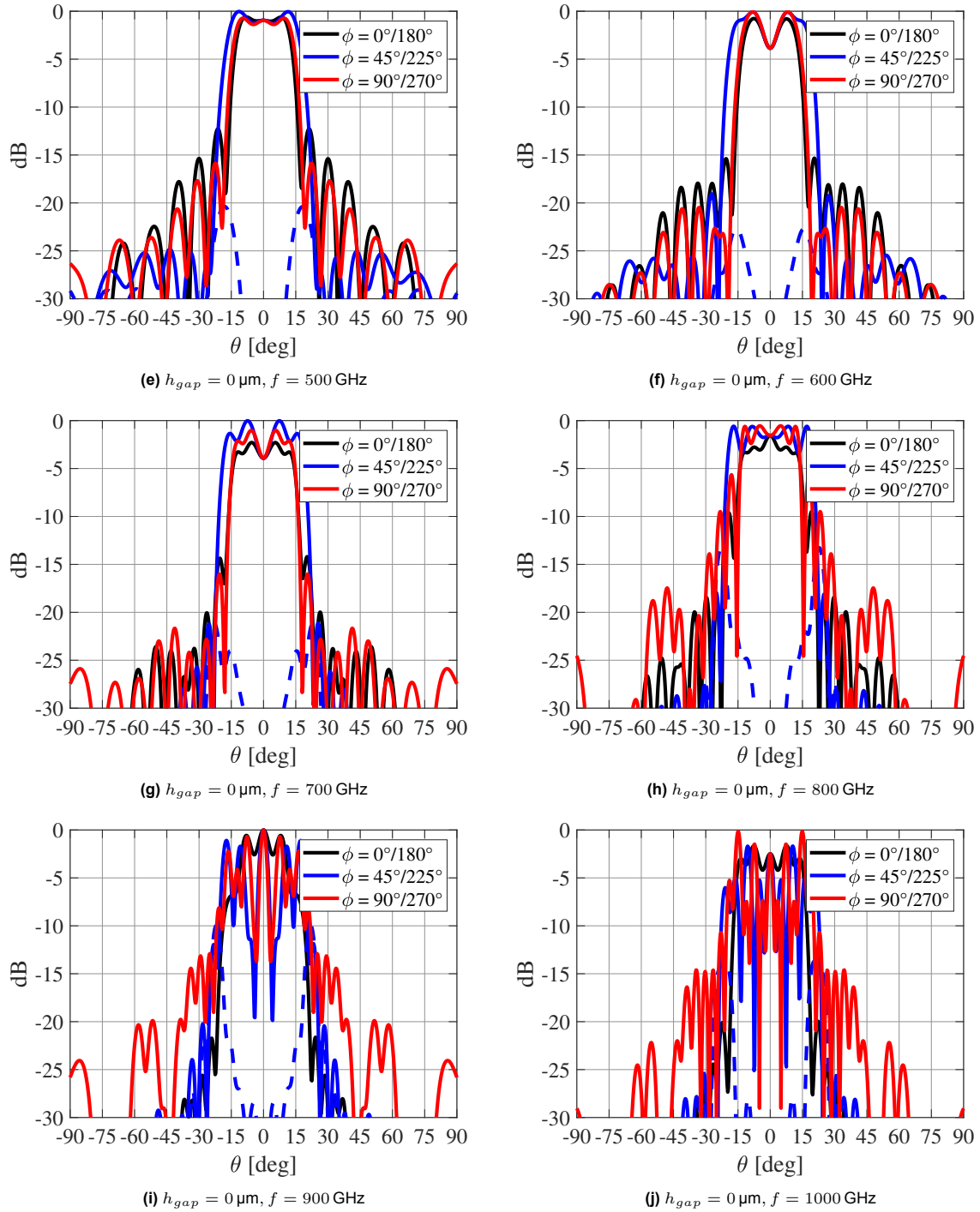
(b)  $h_{gap} = 0 \mu m, f = 200 \text{ GHz}$



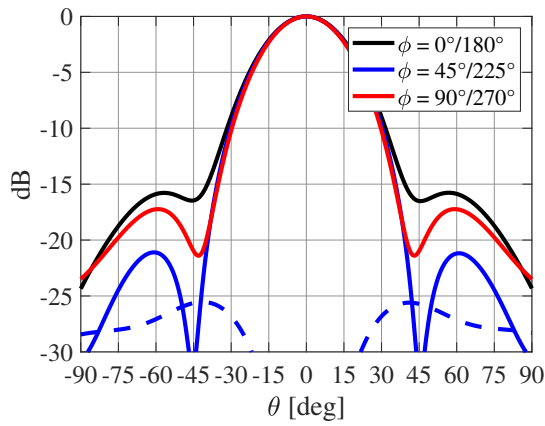
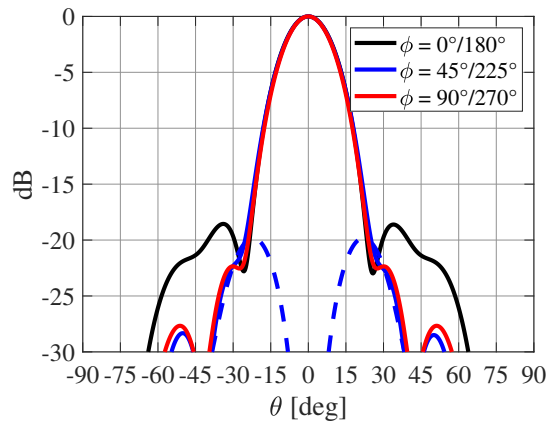
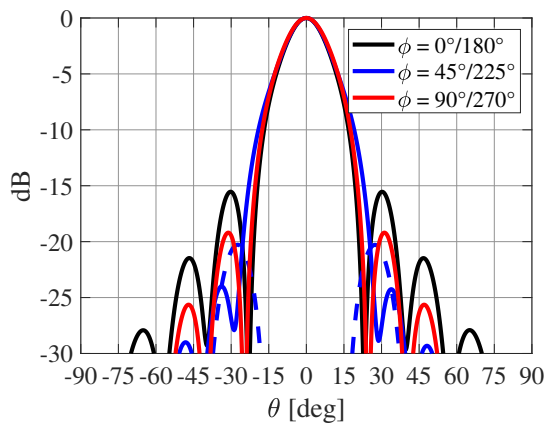
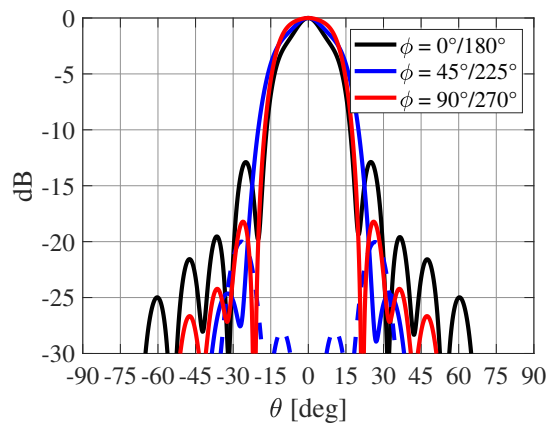
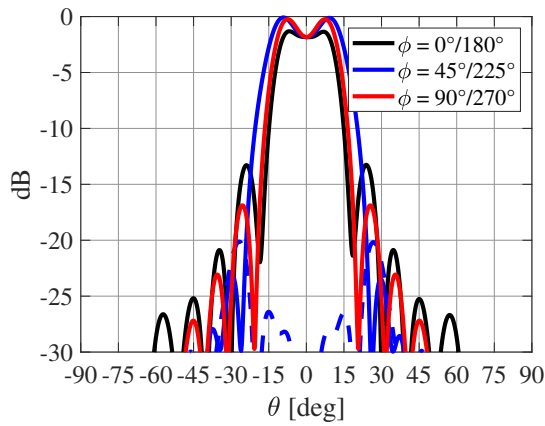
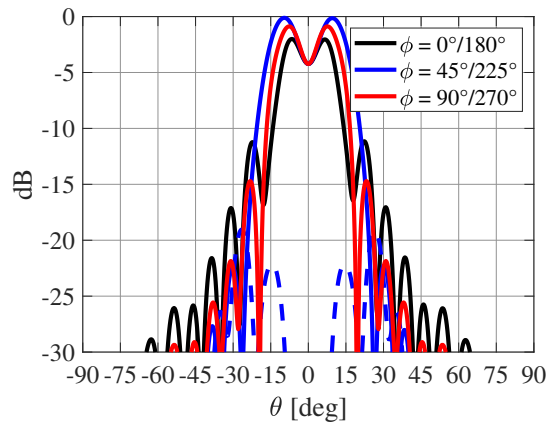
(c)  $h_{gap} = 0 \mu m, f = 300 \text{ GHz}$



(d)  $h_{gap} = 0 \mu m, f = 400 \text{ GHz}$



**Figure E.1:** Normalized secondary far-field amplitude patterns of the redesigned PCCA geometry with  $h_{gap} = 0 \mu\text{m}$  and  $E_{EQ} = 0.38R_{lens}$ . Note that the co-polarized components are indicated with solid lines, and the cross-polarized components are indicated with dashed lines.

E.1.2. Amplitude patterns  $h_{gap} = 10\mu m$ (a)  $h_{gap} = 10\ \mu m, f = 100\ \text{GHz}$ (b)  $h_{gap} = 10\ \mu m, f = 200\ \text{GHz}$ (c)  $h_{gap} = 10\ \mu m, f = 300\ \text{GHz}$ (d)  $h_{gap} = 10\ \mu m, f = 400\ \text{GHz}$ (e)  $h_{gap} = 10\ \mu m, f = 500\ \text{GHz}$ (f)  $h_{gap} = 10\ \mu m, f = 600\ \text{GHz}$

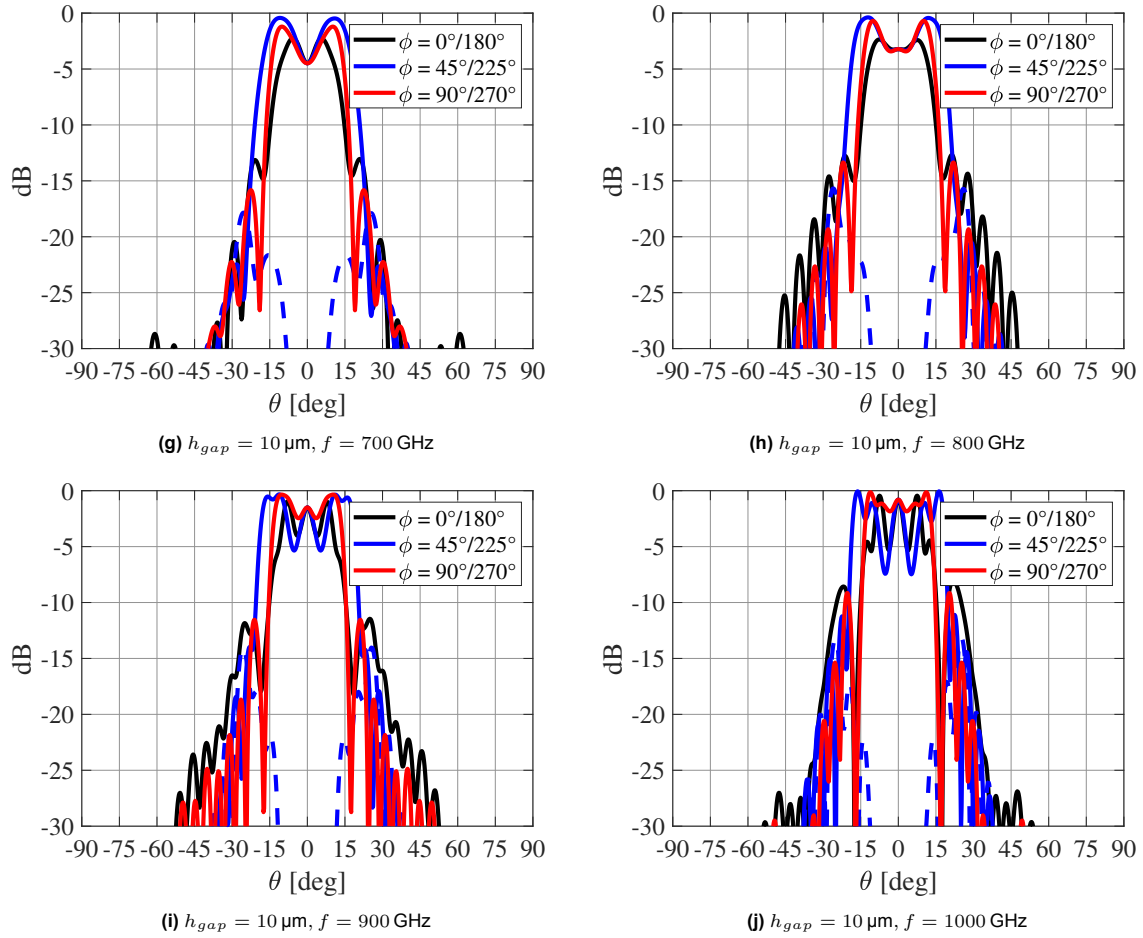


**Figure E.2:** Normalized secondary far-field amplitude patterns of the redesigned PCCA geometry with  $h_{gap} = 10 \mu\text{m}$ ,  $E_{EQ} = 0.38R_{lens}$  and  $R_{lens} = 2.5 \text{ mm}$ . Note that the co-polarized components are indicated with solid lines, and the cross-polarized components are indicated with dashed lines.

## E.2. Phase error losses

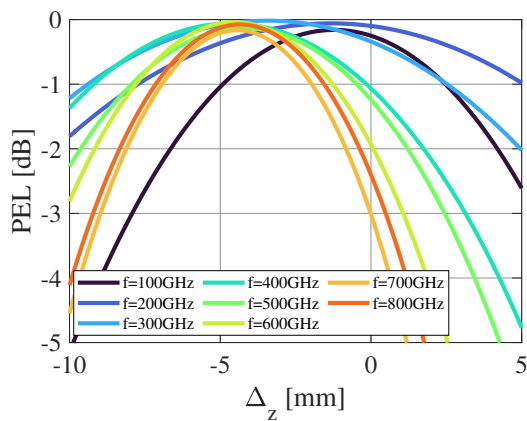


**Figure E.3:** PEL evaluated for different  $\Delta_z$  of the secondary fields of the redesigned PCCA with  $h_{gap} = 0 \mu\text{m}$ ,  $E_{EQ} = 0.38R_{lens}$  and  $R_{lens} = 2.5 \text{ mm}$ .

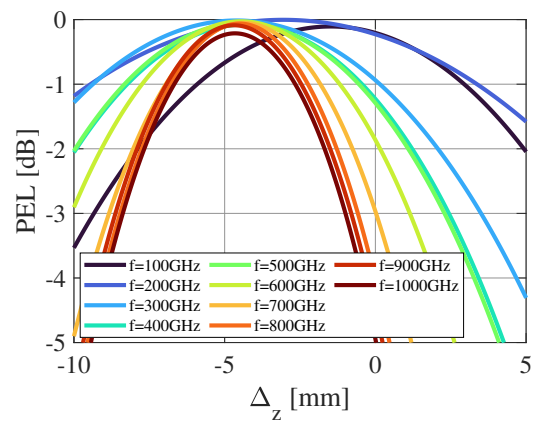
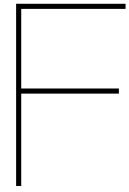


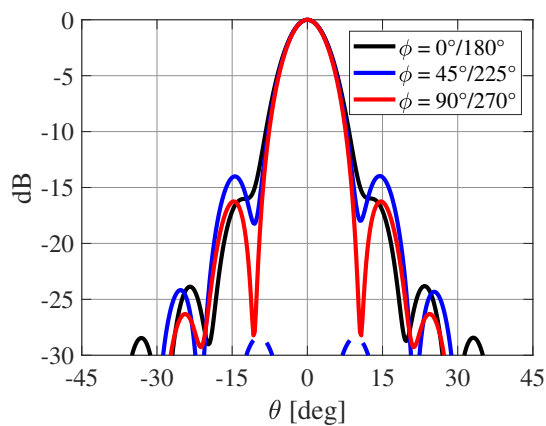
**Figure E.4:** PEL evaluated for different  $\Delta_z$  of the secondary fields of the redesigned PCCA with  $h_{gap} = 10 \mu\text{m}$ ,  $E_{EQ} = 0.38R_{lens}$  and  $R_{lens} = 2.5 \text{ mm}$ .



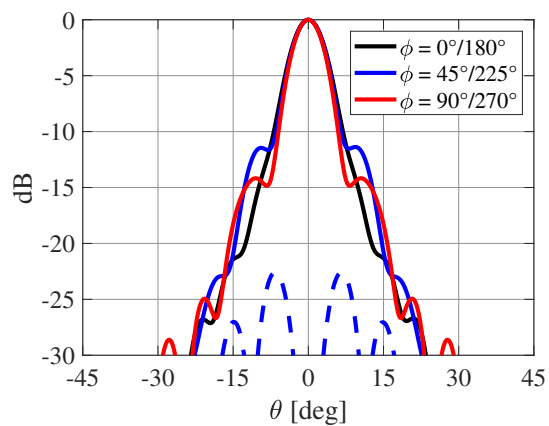
# Secondary fields leaky wave bow-tie PCA

## F.1. Secondary far-field patterns

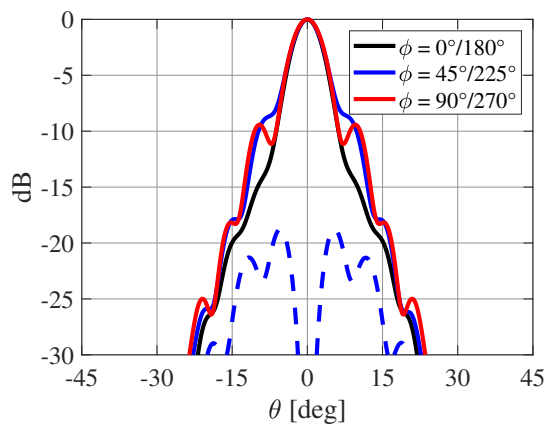
In this section, the amplitude of the secondary fields radiated by a leaky-wave bow-tie antenna with  $R_{lens} = 5$  mm and  $h_{gap} = 10$   $\mu$ m.



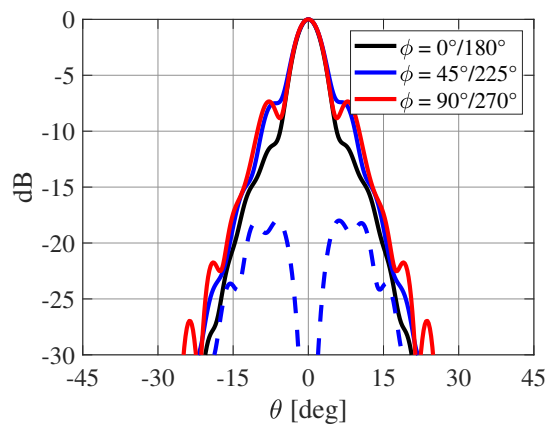
(a)  $f = 200$  GHz



(b)  $f = 300$  GHz



(c)  $f = 400$  GHz



(d)  $f = 500$  GHz

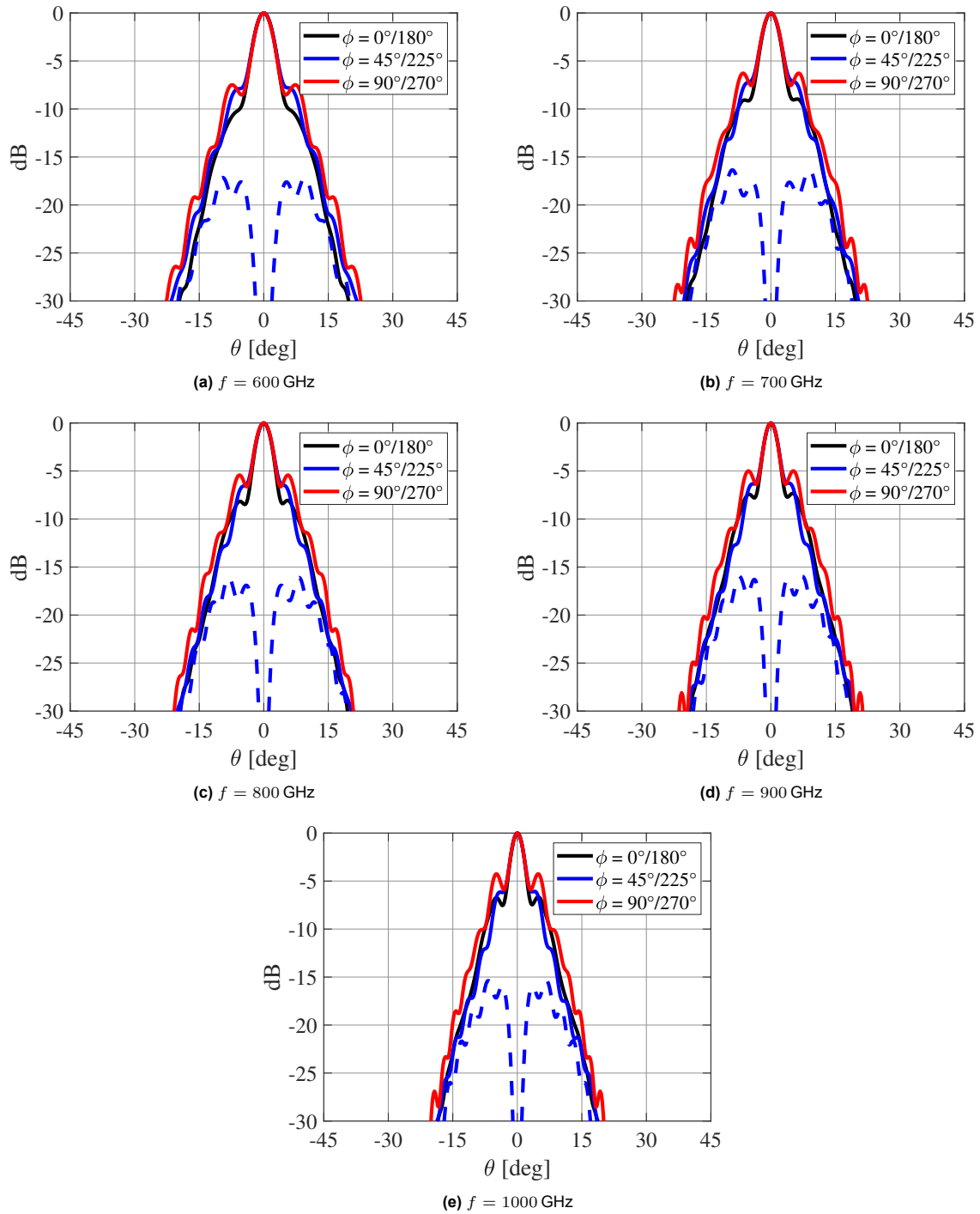


**Figure F.2:** Secondary field amplitude patterns of the leaky wave bow-tie PCA. Note that the co-polar component is represented by the solid lines, and the cross-polar component is represented by the dashed line.

### F.2. Phase error losses

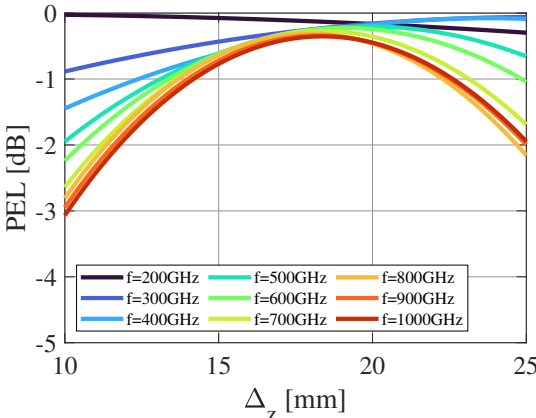


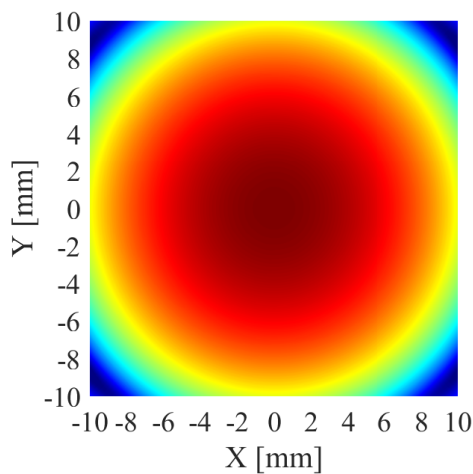
Figure F.3: PEL of the secondary fields of the LW-BT evaluated for different  $\Delta_z$ .



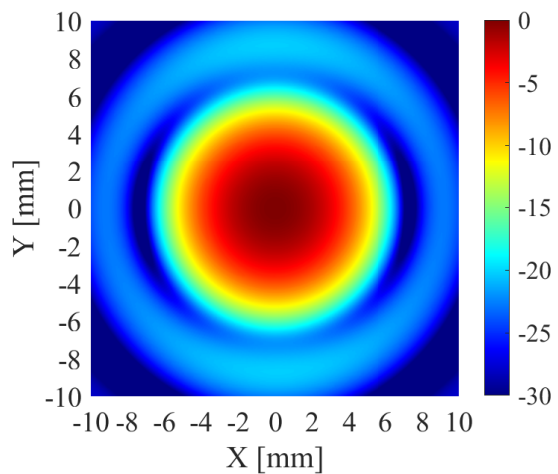
# Focal field amplitude patterns

In this chapter, the amplitude of the focal fields in the imaging setup designed for the different considered antenna structures, discussed in Chapter 6.

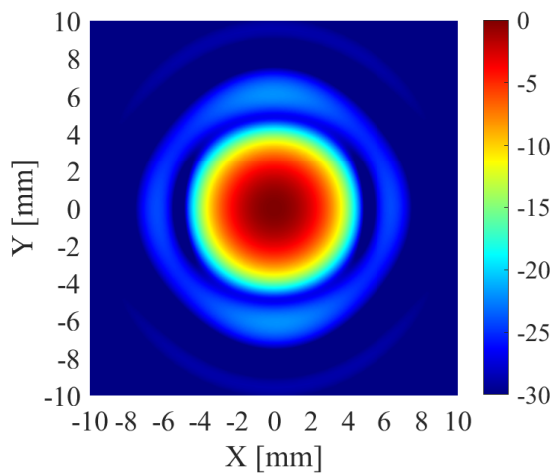
## G.1. PCCA $h_{gap} = 0 \mu m$



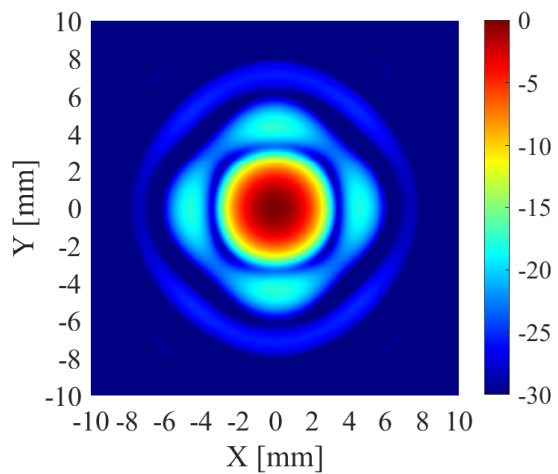
(a)  $f = 100$  GHz



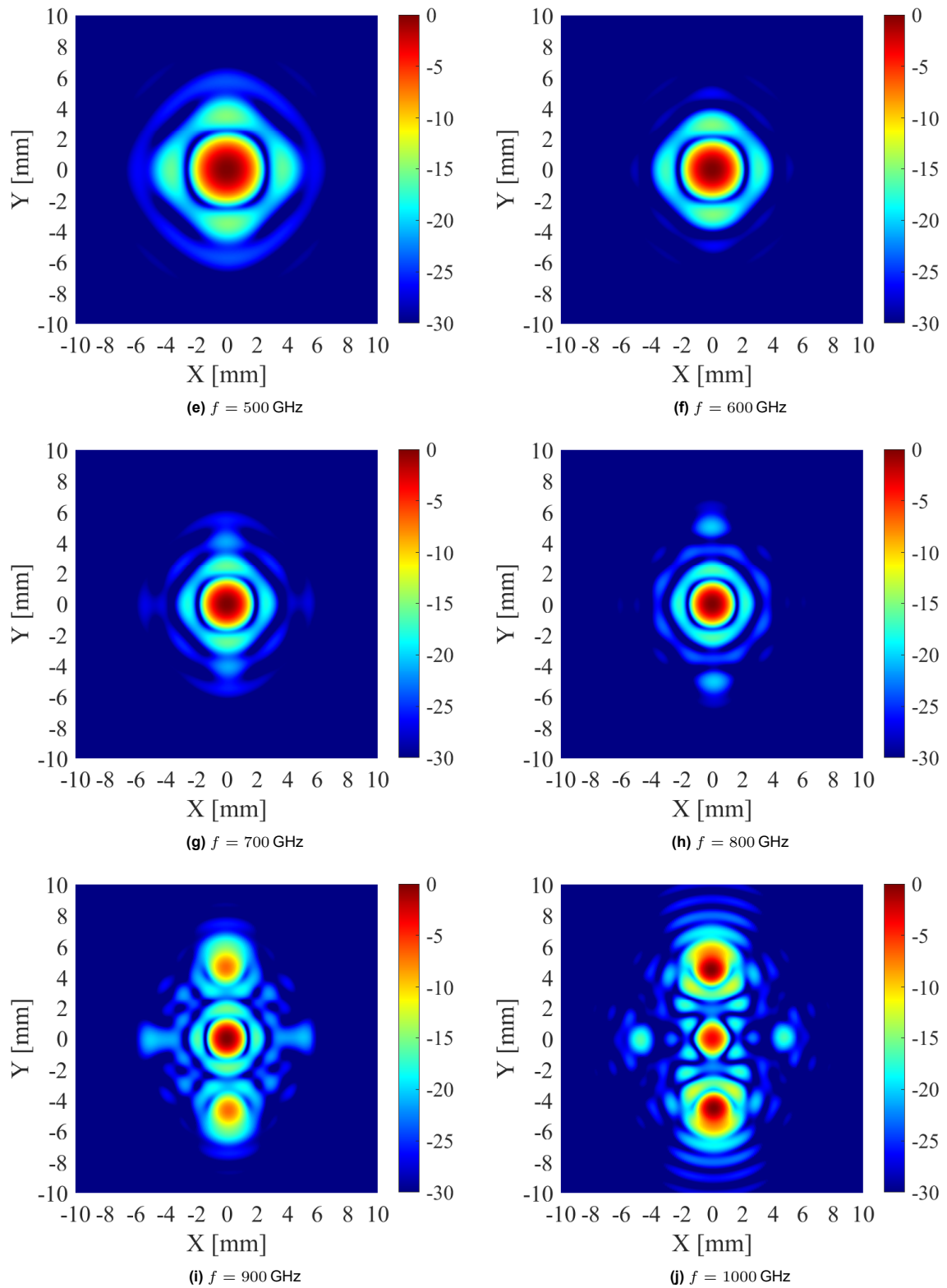
(b)  $f = 200$  GHz



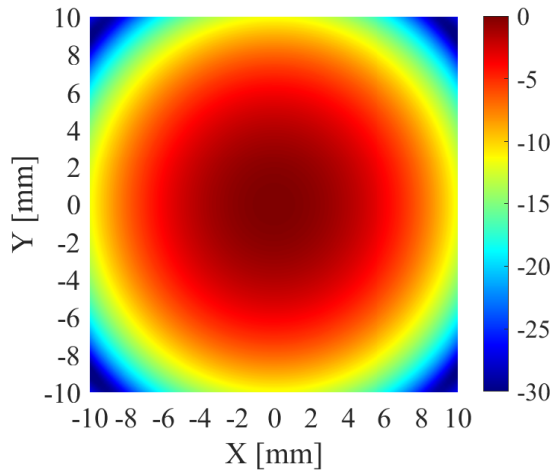
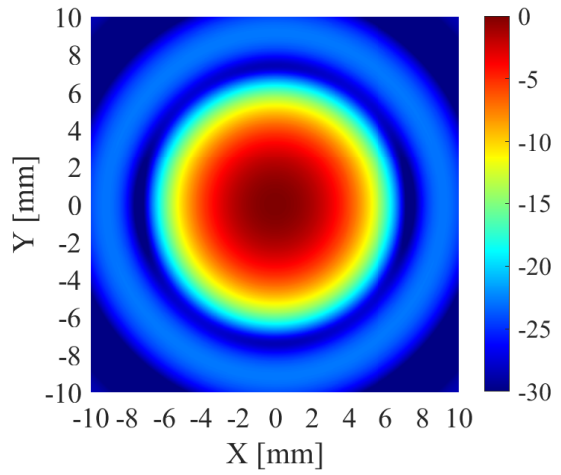
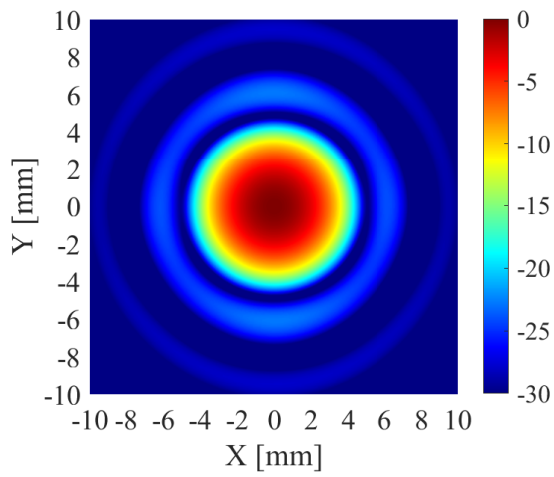
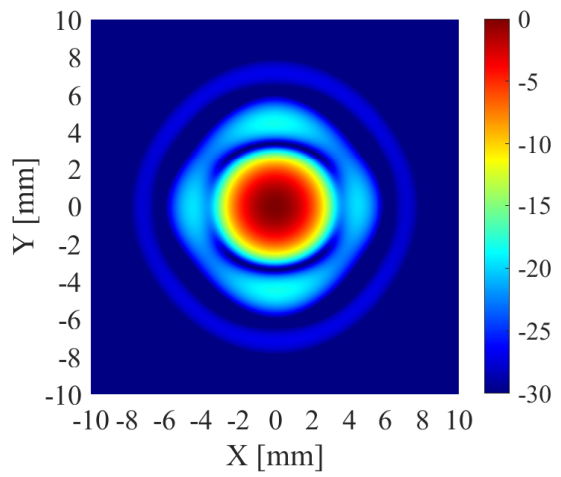
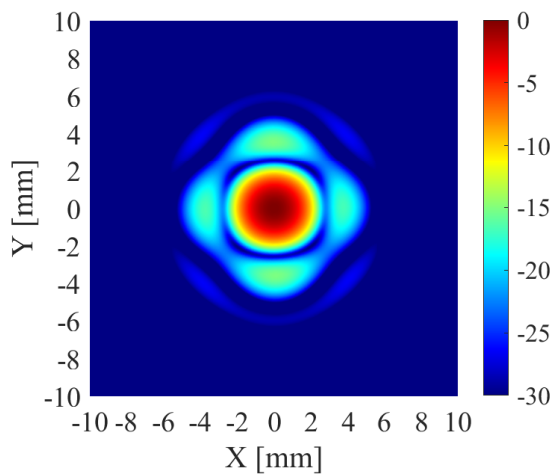
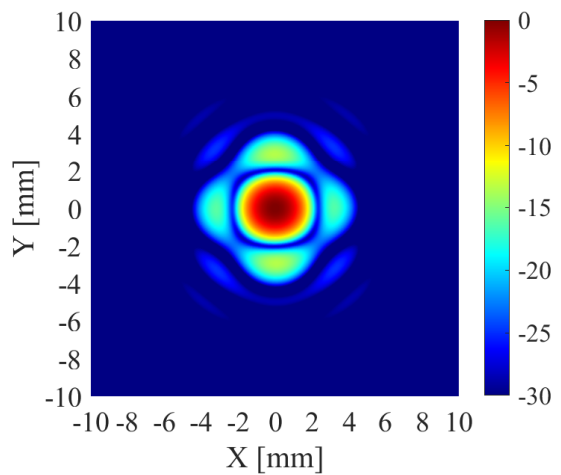
(c)  $f = 300$  GHz



(d)  $f = 400$  GHz



**Figure G.1:** Focal fields of the PCCA with  $h_{gap} = 0\mu m$  in the imaging setup defined in Chapter 6.

**G.2. PCCA  $h_{gap} = 10\mu m$** (a)  $f = 100$  GHz(b)  $f = 200$  GHz(c)  $f = 300$  GHz(d)  $f = 400$  GHz(e)  $f = 500$  GHz(f)  $f = 600$  GHz

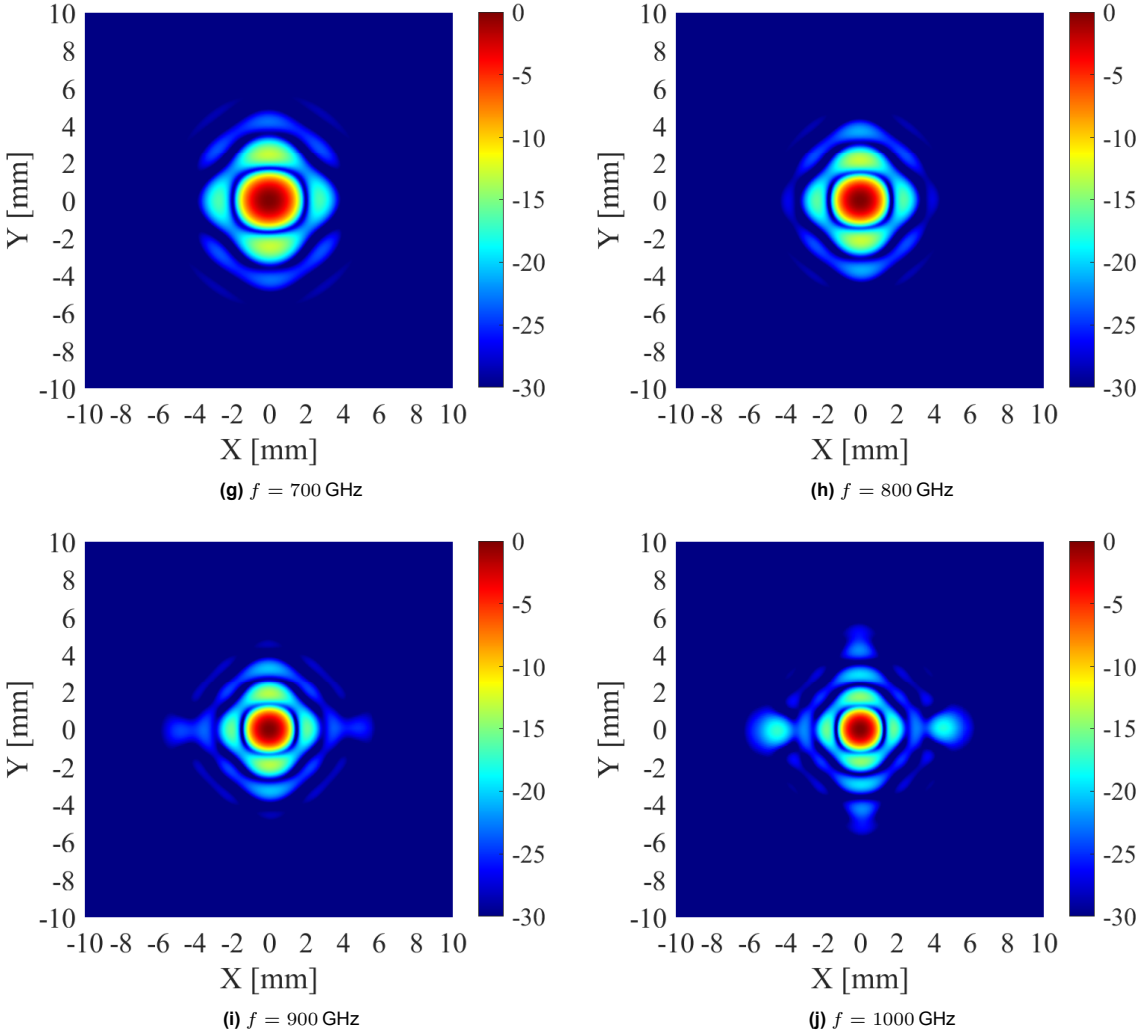
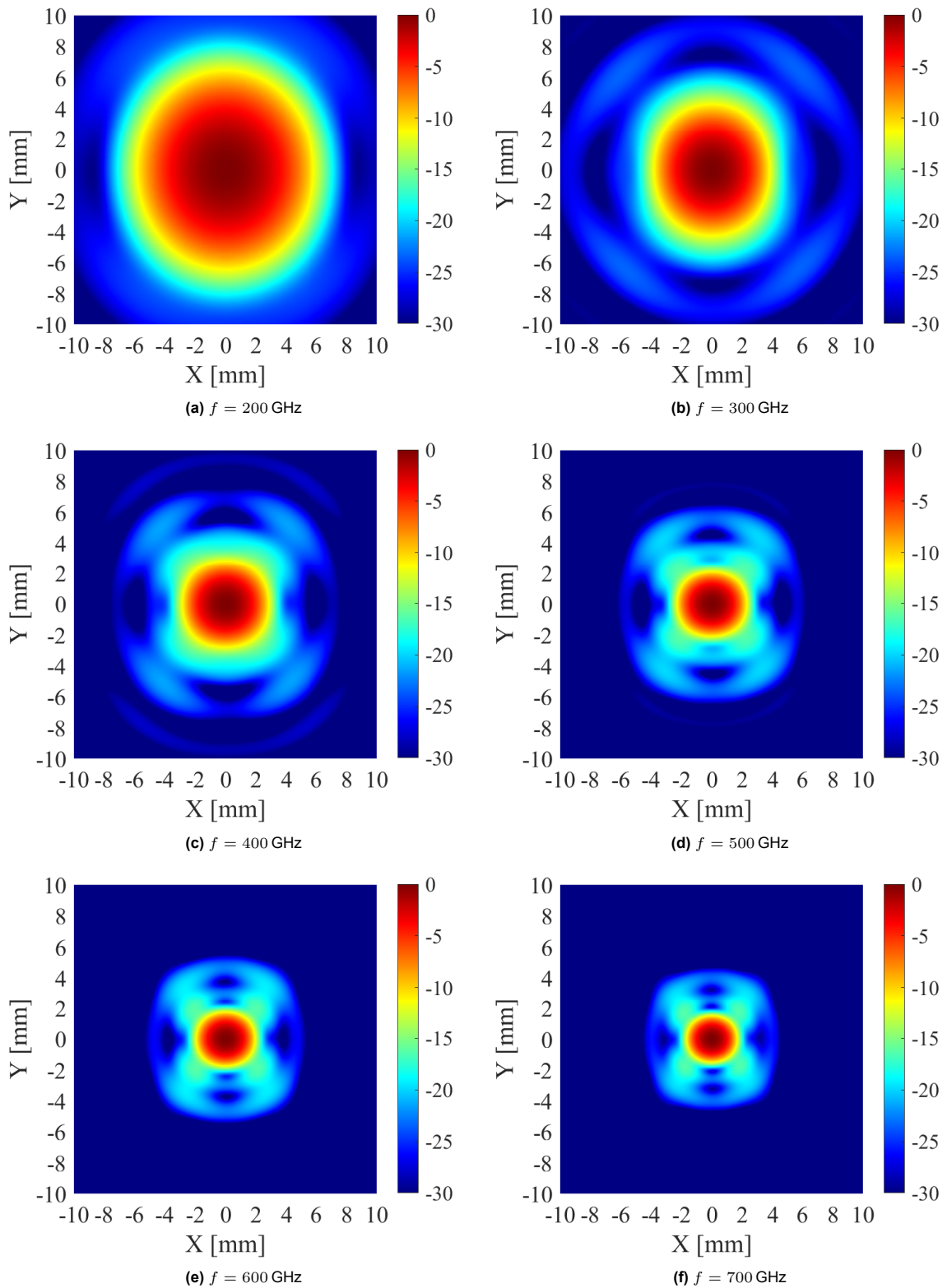
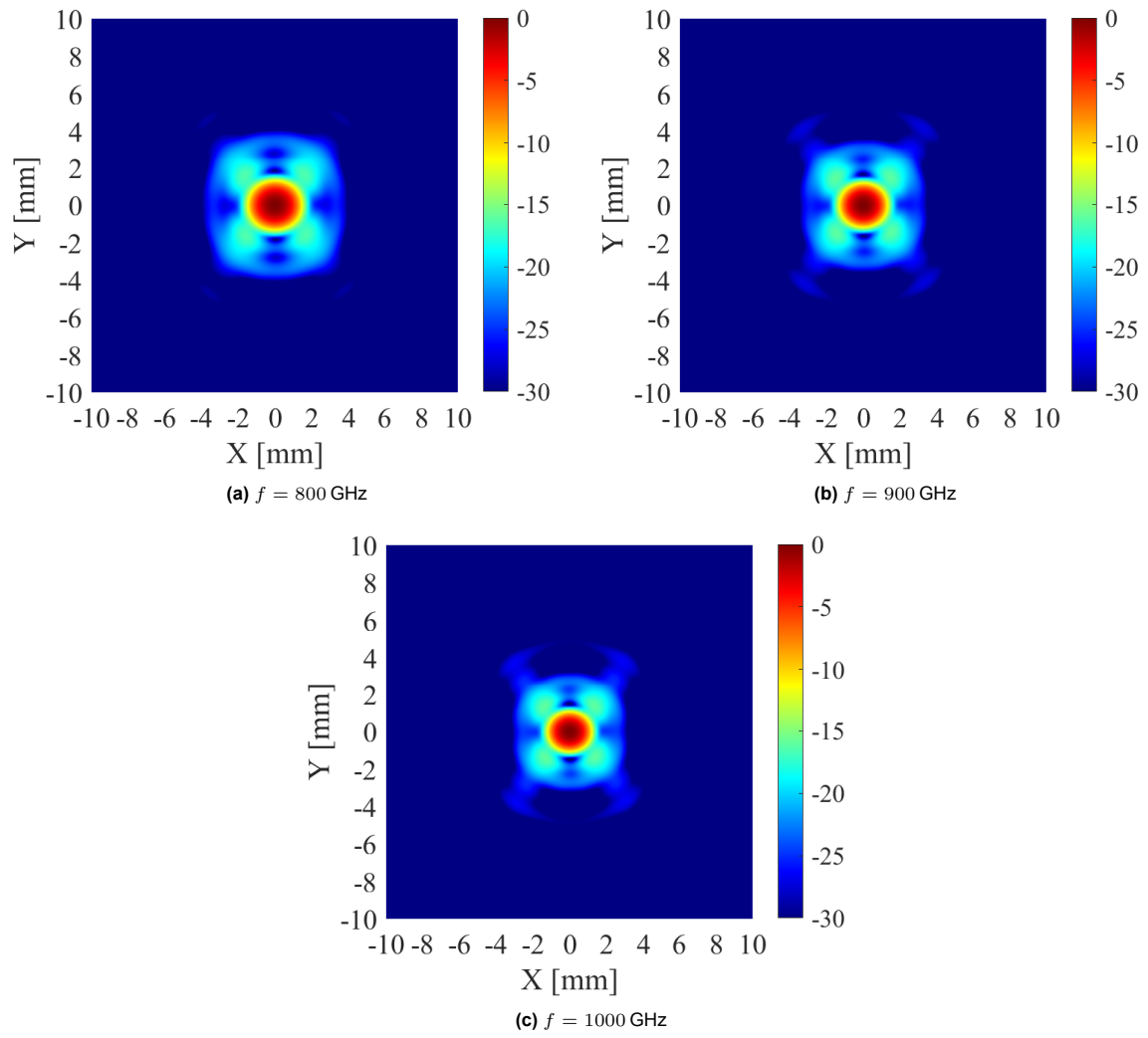
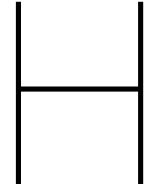


Figure G.2: Focal fields of the PCCA with  $h_{gap} = 10\mu m$  in the imaging setup defined in Chapter 6.

**G.3. Leaky wave bow-tie PCA  $h_{gap} = 10\mu m$** 



**Figure G.4:** Focal fields of the leaky wave bow tie PCA with  $h_{gap} = 10\mu m$  in the imaging setup defined in Chapter 6.



## PEL parabolic reflector fields

In this chapter, the PEL of the equivalent aperture fields of a parabolic reflector evaluated using Equation 5.1 for the geometries considered in Table 5.2. Note that the shape of the calculated PEL is similar to that of the field-matching efficiency given in Figure H.1.

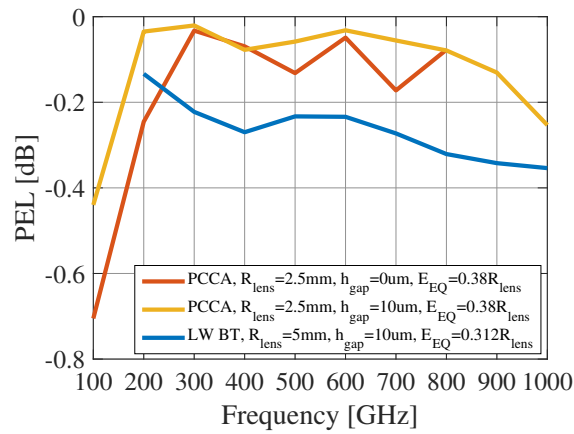


**Figure H.1:** Phase error loss of the equivalent aperture fields of a parabolic reflector for the geometries considered in Table 5.2.